4-23-2012 12:00 AM

Haptics-Enabled Teleoperation for Robotics-Assisted Minimally Invasive Surgery

Ali Talasaz
The University of Western Ontario

Supervisor
Dr. Rajni Patel
The University of Western Ontario

Graduate Program in Electrical and Computer Engineering
A thesis submitted in partial fulfillment of the requirements for the degree in Doctor of Philosophy

Haptics-Enabled Teleoperation for Robotics-Assisted Minimally Invasive Surgery

(Thesis Format: Monograph)

by

Ali Talasaz

Graduate Program in Engineering Science
Department of Electrical and Computer Engineering

A thesis submitted in partial fulfillment
of the requirements for the degree of
Doctor of philosophy

The School of Graduate and Postdoctoral Studies
The University of Western Ontario
London, Ontario, Canada

THE UNIVERSITY OF WESTERN ONTARIO
School of Graduate and Postdoctoral Studies

CERTIFICATE OF EXAMINATION

Advisor	Examining Board
Dr. Rajni V. Patel	Dr. Peter Liu
	Dr. Ilia Polushin
	Dr. Mehrdad Kermani
	Dr. Shaun Salisbury

The thesis by
Ali Talasaz

entitled
Haptics-Enabled Teleoperation for Robotics-Assisted Minimally Invasive Surgery

is accepted in partial fulfillment of the
requirements for the degree of
Doctor of Philosophy

Date: March 12, 2012

Chairman of Examining Board
Dr.

Abstract

The lack of force feedback (haptics) in robotic surgery can be considered to be a safety risk leading to accidental tissue damage and puncturing of blood vessels due to excessive forces being applied to tissue and vessels or causing inefficient control over the instruments because of insufficient applied force. This project focuses on providing a satisfactory solution for introducing haptic feedback in robotics-assisted minimally invasive surgical (RAMIS) systems. The research addresses several key issues associated with the incorporation of haptics in a master-slave (teleoperated) robotic environment for minimally invasive surgery (MIS). In this project, we designed a haptics-enabled dual-arm (two masters - two slaves) robotic MIS testbed to investigate and validate various single-arm as well as dual-arm teleoperation scenarios. The most important feature of this setup is the capability of providing haptic feedback in all 7 degrees of freedom (DOF) required for RAMIS (3 translations, 3 rotations and pinch motion of the laparoscopic tool). The setup also enables the evaluation of the effect of replacing haptic feedback by other sensory cues such as visual representation of haptic information (sensory substitution) and the hypothesis that surgical outcomes may be improved by substituting or augmenting haptic feedback by such sensory cues. To provide realistic haptic feedback, it is necessary to measure forces acting at the tip of the laparoscopic instruments in all appropriate directions, as well as when gripping, cutting or palpating tissue. In order to achieve this, we have incorporated two types of laparoscopic instruments in the testbed: A sensorized da Vinci tool, with the capability of measuring grasping forces provided by several strain gauges embedded in the tool shaft, and a customized instrument, the Tactile Sensing Instrument (TSI), which has been developed in our laboratory for soft-tissue palpation in RAMIS.

Two surgical scenarios are considered in this project: Tumor localization in soft-tissue palpation, and endoscopic suturing. The first application is to localize tumors embedded in liver and lung tissue through the single-arm master-slave teleoperation system. Since the stiffness of a tumor is higher than that of healthy tissue, it can be distinguished as a hard nodule during remote palpation. Tactile sensing is a method that can be used in RAMIS to localize cancerous tumors prior to performing ablative therapies. However, its performance is highly dependent on the consistency of the exploration force. Using the customized tactile sensing instrument, the pressure distribution over the tissue is captured and provided as a color contour map on a screen. In order to apply the exploration force consistently over the tissue, different force feedback modalities are incorporated with tactile sensing feedback: Direct reflection of force feedback, visual presentation of interaction forces, and a fusion method utilizing an autonomous force control for the exploration force in the palpation direction and direct reflection of the force measured at the location of the tumor to the operator's fingers through the grasper mechanism of the haptic interface. The problem of incorporating haptic feedback in robot-assisted endoscopic suturing is explored as the next telesurgery scenario. The dual-arm teleoperation setup is used for this application. In order to assess the quality of suturing, we divide the suturing task into two phases: stitching and knot tying. Each phase consists of several well-specified sub-tasks. The experiments are performed in three modes: without force feedback, with visual force feedback and with direct force reflection to the user. Three levels are considered for the visual feedback presented to the user. The main objective of showing force in different levels is to assure the user that the force being applied on the suture is sufficient to end up with a secure knot. The main focus on this work is to explore which way of presenting force feedback can be more effectively used, and how each modality can help the user to increase the performance.

KEYWORDS: Robot-Assisted Minimally Invasive Surgery, Telesurgery, Teleoperation, Force Feedback, Tactile Feedback, Soft-Tissue Palpation, Endoscopic Suturing.

Statement of Collaboration

The work presented in this thesis involved collaboration with Harman Bassan who performed mechanical design of the grasping mechanism of the 7-DOF Haptic Wand and Simon Perreault who helped with development of kinematics modeling of the 7-DOF Haptic Wand and the da Vinci needle driver instrument. The Tactile Sensing Instrument used for soft-tissue palpation was designed at CSTAR in a project on palpation for minimally invasive surgery involving Melissa Perri, Greig McCreery, Ana Luisa Trejos, Michael Naish, Rajni Patel and Richard Malthaner. I would also like to acknowledge the contribution of Ana Luisa Trejos to sensorize the da Vinci needle drivers used in the experimental work for suturing application.

Acknowledgement

First and foremost, I wish to express my sincere gratitude and appreciation to my supervisor, Dr. Rajni Patel for giving me the opportunity to do this project at CSTAR. I would like to thank him for his support, encouragement, great advices, and constructive criticisms during the past years. I would also like to thank the members of the examining committee, Dr. Peter Liu, Dr. Ilia Polushin, Dr. Mehrdad Kermani, and Dr. Shaun Salisbury.

Special thanks to my dear friend Dr. Mahdi Azizian for his help and insightful discussions during my work at CSTAR. My gratitude goes to all the past and present members of CSTAR, especially Simon Perreault, Chris Ward, Dr. Harman Bassan, and Ana Luisa Trejos for their help in this project. Sincere thanks also go to my dear friends at CSTAR, Iman Khalaji, Mahta Khoshnam, and Ali Asadian and my close friend in London, Dr. Mehdi Delrobaei for providing me with a home away from home.

I would like to thank my very special friend, Ali Neissi who is like a brother to me. I am always proud to have such a wonderful friend for a very long time. It is always great to have a very close friend who believes in you, supports you, and encourages you all the time.

Last but by no means least, I would like to thank my lovely mom who means a world to me. She scarified her life for me and provided me unconditional love and care. Mom, I am deeply indebted to you and love you from the bottom of my heart. I am thankful beyond words to all my kind relatives in Iran who have always supported my mom and made it possible for me to focus on my work here in Canada. Without their help, I would not be able to continue my Ph.D. study.

Table of Contents

List of Tables

List of Figures

Nomenclature

MIS	Minimally Invasive Surgery
RAMIS	Robot-Assisted Minimally Invasive Surgery
MIST	Minimally Invasive Surgery and Therapy
3D	3 Dimensional
2D	2 Dimensional
DOFs	Degrees of Freedom
MRI	Magnetic Resonance Imaging
CT	Computed Tomography
LED	Light Emitting Diode
CSTAR	Canadian Surgical Technologies and Advanced Robotics
UDP	User Datagram Protocol
QuaRC	Quanser Real-Time Control
MATLAB	MATrix LABoratory
ARCNET	Attached Resource Computer NETwork
AC	Alternating Current
PID	Proportional-Integral-Derivative
PI	Proportional and Integral
PD	Proportional and Derivative
TSI	Tactile Sensing Instrument
PPS	Pressure Profile Systems
HIL	Hardware-In-Loop
API	Application Programming Interface
RMSE	Root Mean Square Error
FKP	Forward Kinematics Problem
IKP	Inverse Kinematics Problem
FK	Forward Kinematics
IK	Inverse Kinematics

RCM	Remote Center of Motion
PFPF	Position-Forward/Position-Feedback
PFFF	Position-Forward/Force-Feedback
JTHIC	Jacobian Transpose Hybrid Impedance Control
JIHIC	Jacobian Inverse Hybrid Impedance Control
JTIC	Jacobian Transpose Impedance Control
VPTF	Visual Presentation of Tactile Feedback
DRFF	Direct Reflection of Force Feedback
VPFF	Visual Presentation of Force Feedback
VFF	Visual Force Feedback
NFF	No Force Feedback
DFF	Direct Force Feddback
PPV	Positive Predictive Value
NPV	Negative Predictive Value
ANOVA	ANalysis Of VAriance
CABG	Coronary Artery Bypass Graft
IROS	Intelligent Robots and Systems
BIOROB	Biomedical Robotics and Biomechatronics
ICRA	International Conference on Robotics and Automation
$\{\psi_1,\psi_2,\phi\}$	End effector position of da Vinci needle driver
$\{\Theta_1,\Theta_2,\Theta_\phi\}$	Motor joint angles for da Vinci needle driver
$\{x,y,z,\phi,\theta,\psi_l,\psi_u\}$	Cartesian position of the haptic wand end effector
$\{\theta_1,\ldots,\theta_8\}$	Haptic Wand joint angles
$\left[\dot{x},\dot{y},\dot{z},\dot{\phi},\dot{\theta},\dot{\psi}_l,\dot{\psi}_u\right]$	Cartesian velocity of the Haptic Wand
$\left[\dot{\theta}_1,\ldots,\dot{\theta}_8\right]$	Angular velocity of the Haptic Wand
$[t_{\theta_1},\ldots,t_{\theta_8}]$	Motor torques of the Haptic Wand
$[f_x,f_y,f_z,t_\phi,t_\theta,t_{\psi_l},t_{\psi_u}]$	Cartesian force/torque of the Haptic Wand
$[\varepsilon_0,\varepsilon_1,\varepsilon_2,\varepsilon_3]$	Quaternion components
$\boldsymbol{K}$, $\boldsymbol{I}$	Velocity constraint matrices
$\boldsymbol{R}_x(\theta)$, $\boldsymbol{R}_x(\theta)$	Rotation matrices in x and y direction
$\boldsymbol{D}$, $\boldsymbol{C}$, $\boldsymbol{G}$	Inertia, coriolis and gravity matrices for the 7-DOF Haptic Wand
$\boldsymbol{K}_p$, $\boldsymbol{K}_v$	Proportional and derivative matrix gains
$\boldsymbol{W}_x$, $\boldsymbol{W}_\theta$	Weighting matrices
α_1, α_2	Poles of high-gain velocity observer

$\boldsymbol{f}_{tip},\ \boldsymbol{\tau}_{tip}$	Force and torque measurement at the tip of instrument
$\boldsymbol{f}_{mes},\ \boldsymbol{\tau}_{mes}$	Total force and torque measured by ATI force sensor
$\boldsymbol{f}_{friction},\ \boldsymbol{\tau}_{friction}$	Friction force and torque measured between trocar and instrument
$\boldsymbol{f}_{nc},\ \boldsymbol{\tau}_{nc}$	Non-contact force and torque for instrument
$\boldsymbol{f}_{off},\ \boldsymbol{\tau}_{off}$	Offset force and torque
$\boldsymbol{f}_{free},\ \boldsymbol{\tau}_{free}$	Force and torque measured by ATI force sensor when moving in free space
$\boldsymbol{f}_{wrist},\ \boldsymbol{\tau}_{wrist}$	Force and torque measured at the wrist of the Mintsubishi PA10 robot
$\boldsymbol{r}^{l}_{cmi}, \boldsymbol{r}^{w}_{cmi}$	Location of the center of mass for segment $\{i\}$ in the local frame and world coordinate
$\boldsymbol{i},\ \boldsymbol{j}, \boldsymbol{k}$	Unit vectors
$\boldsymbol{g}$	Gravity vector
$\boldsymbol{G}$	Gravity term
$\boldsymbol{l}_{cm}$	Location of the center of mass for instrument
${}^{o}_{s}\boldsymbol{R}$	Rotation matrix from the robot base to the sensor frame
$\boldsymbol{P}_i$	Distal part i for da Vinci needle driver
r_{Θ_i}	Radius of the pulley associated with Θ_i
r_{ψ_i}	Radius of the pulley associated with ψ_i
r_{ip}	Radius of the intermediate pulley mounted on the axis ϕ of the Haptic Wand gripper
r_{Θ_ϕ}	Radius of the pulley associated with Θ_ϕ
r_ϕ	Radius of the pulley associated with ϕ
l, u	Lower and upper part of the Haptic Wand
$\mathcal{A}$	World frame of the Haptic Wand
O	Origin of the world frame of the Haptic Wand
$\mathcal{B}$	Moving frame attached to the handle of the Haptic Wand gripper
P	Origin of the moving frame
$\mathbf{Q_l}$	Rotation matrix corresponding to the transformation $\mathcal{A} \rightarrow \mathcal{B}_l$
$\boldsymbol{P}$	Projection matrix
$\boldsymbol{U}^I$	Moore-Penrose pseudo inverse of the matrix $\boldsymbol{U}$
$\boldsymbol{\theta}$	The vector of joint angles of the Haptic Wand
$\dot{\boldsymbol{\theta}}$	The vector of angular velocities of the Haptic Wand
$\ddot{\boldsymbol{\theta}}$	The vector of angular accelerations of the Haptic Wand
$\boldsymbol{\tau}$	The vector of actuator torques for the 7-DOF Haptic Wand

$\boldsymbol{F}_{\text{ext}}$	External force applied to the Haptic Wand.
$\boldsymbol{r}_{oi}^{w}$	Position of the origin of the local frame
Ω_i	Rotational velocity in local frame
$\boldsymbol{v}_{cmi}$	Translational velocity for the center of mass vector
K_i	Kinetic energy
$\boldsymbol{M}_i$	Translational inertia matrix
$\boldsymbol{I}_i$	Rotational inertia matrix
V_i	Potential energy
L	Lagrangian function
$\boldsymbol{\mathcal{D}}(\boldsymbol{\theta})$	Mass matrix of the Haptic Wand for the first 6 joint angles
V	Total potential energy
$\tau_{m,i}$	Torque computed from mathematical model
K_m	Motor torque constant
R_m	Motor armature resistance
J_{eq}	Total inertia of load and motor rotor
$\boldsymbol{\tau}_c$	Torque control command
$\boldsymbol{\tau}_f$	Friction torque
$\boldsymbol{\tau}_{ff}$	Feed-forward control torque
$\boldsymbol{\tau}_{fb}$	Feedback control signal
m	Master manipulator
s	Slave manipulator
d	Desired value
r	Reference value
u	Upper part
l	Lower part
e	Error
$\boldsymbol{X}$	Position vector of manipulator
$\dot{\boldsymbol{X}}$	Velocity vector of manipulator
$\ddot{\boldsymbol{X}}$	Acceleration vector of manipulator
C_1	Position scaling factor
C_2	Force scaling factor
F_e	Environment force
$\boldsymbol{M}$	Cartesian inertia matrix
$\boldsymbol{B}$	Cartesian damping matrix
$\boldsymbol{K}$	Cartesian stiffness matrix

$\boldsymbol{J}$	Jacobian matrix
$\boldsymbol{J}_{aug}$	Augmented Jacobian matrix
$\boldsymbol{q}$	Joint angle of manipulator
$\dot{\boldsymbol{q}}$	Angular velocity
$\ddot{\boldsymbol{q}}$	Angular acceleration
$\boldsymbol{u}$	Control input of manipulator in Cartesian space
$\boldsymbol{\rho}$	Auxiliary variable defined for high gain force observer
γ	Observer gain
$\hat{\dot{\boldsymbol{q}}}$	Angular velocity estimation
$\boldsymbol{p}_t$	Position of the tip of palpation tool
$\boldsymbol{p}_{rcm}$	RCM point
e_x	RCM error in x-direction
e_y	RCM error in y-direction
e_p	Position error
e_o	Orientation error
$\boldsymbol{S}$	Selection matrix
$\boldsymbol{\mathcal{F}}_{rcm}$	RCM kinematic function
$\boldsymbol{R}$	Rotation matrix
$\boldsymbol{k}_e$	Orientation error axis vector
$f_{lx}^t,\ f_{ly}^t$	Lateral forces in $x, y-$ direction in tissue plane
$f_{lx}^p,\ f_{ly}^p$	Lateral forces in $x, y-$ direction in palpation plane
f_p^t	Palpation force in tissue plane
f_p^p	Palpation force in palpation plane
F_{avg}	Average force
F_{max}	Maximum force
T_{ct}	Task completion time

Chapter 1

Introduction

Surgery is a common medically invasive procedure often resulting in huge discomfort for the patient during recovery. In its conventional way, i.e., open surgery, surgeons need to cut skin and tissues to get access to the structures or organs involved. To reduce negative side effects of open surgery, a new type of surgery has been used over the past several decades, called Minimally Invasive Surgery (MIS) or laparoscopic surgery. In MIS, laparoscopic instruments are inserted into the body cavity through small incisions and surgeons perform surgical intervention by remotely controlled manipulation of the instruments with indirect observation of the surgical field through

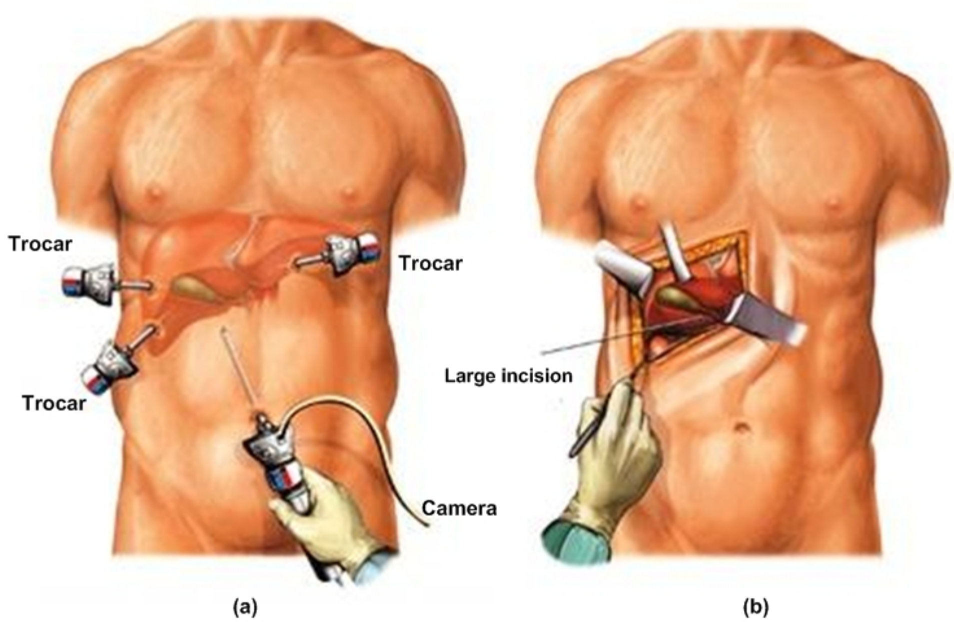

Figure 1.1: Laparoscopic vs Open Surgery (©gallbladder-help.com).

an endoscope. Fig. 1.1 shows a comparison between open surgery and minimally invasive surgery.

Although minimally invasive surgery significantly reduces trauma to the body, post-operative pain and length of hospital stay compared to open surgery, it has inherent drawbacks and pitfalls in terms of human motor functioning and sensory capabilities that impact the conduct of the surgery. These drawbacks include lack of dexterity, lack of fine manipulation capability (due to hand tremors), and significant degradation of haptic feedback (the sense of touch) concerning tool-tissue interactions.

Figure 1.2: The da Vinci surgical robotic system (©Intuitive Surgical Inc.).

Over the last twenty years, much research has been directed at taking advantage of the benefits of incorporating robotics in surgery and therapy by developing appropriate tools for assisting clinicians [2]. In this context, a major area of research has focused on the development of robotic systems and tools for minimally invasive surgery and therapy (MIST). Robotics-assisted minimally invasive surgery (RAMIS) is a specialized form of minimally invasive surgery which can bring many advantages to patients and the health care system: to increase dexterity in manipulating laparoscopic instruments, to significantly reduce the surgeon's hand tremor during an MIS task, and to increase precision by scaling down the surgeon's hand motion. A well-known and widely used robot-assisted minimally invasive telesurgical system is the da Vinci surgical robotic system (Fig. 1.2) from Intuitive Surgical Inc. (currently the only minimally invasive surgical robotic system approved for clinical use) [3].

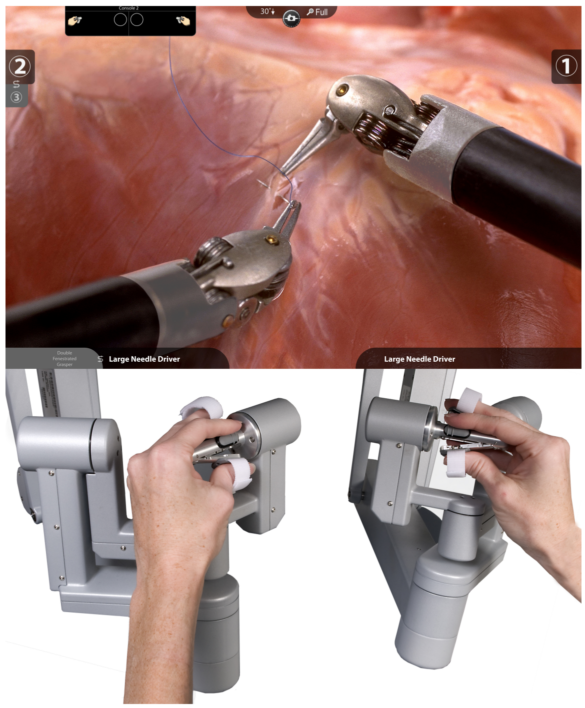

Figure 1.3: Hand control units of the surgeon console and the operative screen (©Intuitive Surgical Inc.).

This master-slave (teleoperated) system consists of a surgeon's console with the hand control interface, shown in Fig. 1.3. This console is used to control four interactive robotics arms using foot pedals that perform surgery on the patient's body through EndoWrist instruments. Two foot pedals provide additional maneuvering capability. The slave system includes three robot arms for manipulating tools and objects and one arm for holding endoscopic camera with two eye pieces that gives the surgeon full stereoscopic vision from the console. The surgeon sits at the console and looks through the binocular eye pieces at a 3D image of the procedure, while maneuvering the arms with two foot pedals and two hand controllers.

EndoWrist instruments designed by da Vinci can provide surgeons with natural dexterity and full range of motion for precise operation through tiny incisions (Fig. 1.4). The EndoWrist Instruments are available in a wide selection of specialized tip designs to enable a broad range of da Vinci procedures in different applications. Fig. 1.5 shows the variety of the instruments which can be used in MIS. These include

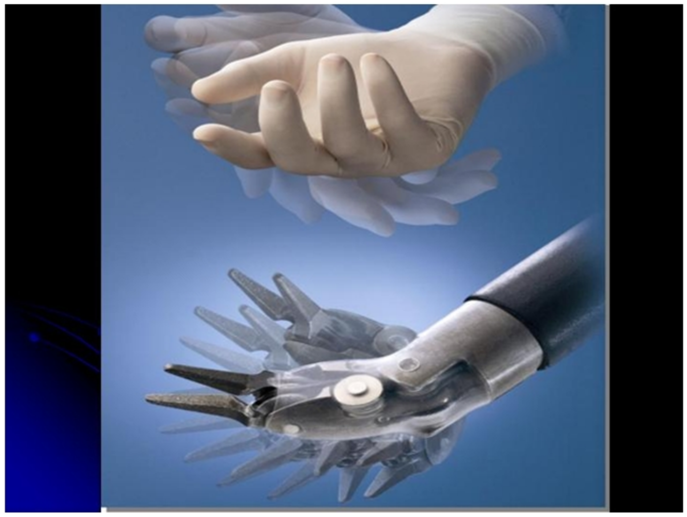

Figure 1.4: Comparison of the dexterity of the EndoWrist with that of the human hand (©Intuitive Surgical Inc.).

Figure 1.5: Different types of EndoWrist instruments: needle driver, energy instrument, forceps, retractor, and cardiac stabilizer (from left to right) (©Intuitive Surgical Inc.).

needle driver, energy instrument, forceps, retractor, and cardiac stabilizer.

While the da Vinci robotic surgical system offers superior dexterity and position control, it has a drawback of not reflecting haptics to the surgeon's side. The lack of haptic interaction has been identified by many surgeons as being a major drawback of the da Vinci system. Incorporating haptics in a surgical teleoperation system is a critical issue as it would provide the surgeon with the feel of interaction between the instrument and tissue during MIS [4]. The lack of haptic feedback in robotic surgery can be considered to be a safety risk: it might lead to accidental tissue damage and puncturing of blood vessels due to excessive forces being applied to tissue and vessels or to inefficient control over the instruments because of insufficient forces of grasping. Although the da Vinci robotic surgical system relays some force feedback sensations from the operative field back to the surgeon throughout the procedure, since this force feedback is based on position error and not direct force sensing, it is very sensitive to the feedback gain. Higher gains may cause disturbances in force perception even when the surgical instrument is not in contact with its environment and no force is being applied [5]. To partially compensate for the loss of force feedback, the da Vinci has offered a high-definition 3D visual system providing depth perception of the surgical field. However, relying on visual 3D images showing deformation of the tissue means that the surgeon could have already damaged the tissue. Besides, for the tasks without the element of elasticity or in the case where the view is slightly obstructed, the lack of force feedback might result in a considerable damage [6]. Moreover, as can be seen later, tactile perception can help surgeons for many applications such as manipulation on delicate tissues and soft-tissue palpation to locate embedded anatomical objects such as tumors, blood vessels, nerves, etc. which are not visually observable during surgical intervention. Therefore, the necessity of a sensing system capable of measuring tactile perception is inevitable in RAMIS. Relying on 3D visual clues obtained from the da Vinci vision system cannot be sufficient for those application.

A haptics-enabled master-slave teleoperation system can take surgery to a new level very similar to real life scenario where the surgeon conducts the surgical procedure by his/her hands while providing significant precision improvement with the highest level of dexterity in a minimally invasive manner. The control architecture that can offer such a capability in RAMIS is called bilateral control providing an interactive environment between the surgeon and the surgical field by transmitting position data from the master to the slave and force data from the slave to the master (as opposed to unilateral control architecture where only position commands are sent to the slave side from the master unit). The main challenge in a bilateral teleoperation system is to maintain transparency while preserving the stability of the system. Transparency is defined as a correspondence between the impedance perceived by the operator and that of the environment such that the remote environment is displayed in a natural way and the operator feels as if he or she is physically present at the remote environment (telepresence).

1.1 Haptics in Teleoperation

Haptics is the science of providing the sensation of touch to human operator through computer applications. In a master-slave RAMIS system, haptics involves the reflection of the interaction between the laparoscopic instrument and tissue to the surgeon through an interface. This interaction can be in the form of cutaneous perception (tactile feedback) or kinesthetic perception (force feedback). Tactile feedback is the perception of shapes, textures, and distributed pressure which is measured by different receptors in skin and force feedback is the perception of weight and resistance to motion which relies on muscles, tendons and joint sensory receptors. In order to have a telepresence RAMIS system, both tactile and force perceptions are required to be reflected to the surgeon's side. Tactile perception needs to be available for the contact area between the laparoscopic instrument and the tissue while force feedback should be available for all 7 degrees of freedom (DOFs) required for MIS: three translations, three rotations and pinch. The main challenge of haptics in RAMIS is how to capture and measure the interaction between the tissue and the instrument in 7-DOFs and how to reflect them to the surgeon's side.

The main issue with capturing tool-tissue interaction is to measure the contact forces at the tip of the instrument without interference from the friction between the trocar and the instrument. If the force sensor is mounted outside the patient's body, all forces applied to the shaft of the instrument are measured and it would be difficult to distinguish the contact force from the rest of unwanted forces applied to the instrument. In order to measure the contact forces accurately, a force sensor needs to be mounted as close as possible to the tip of the instrument inside the patient's body and in direct contact with the tissue. An important concern for the force sensor inserted into the patient's body is its bicompatibility and strerilizability.

With an accurate measurement of the contact forces, the next step in haptics is to reflect them to the surgeon through a haptic interface. Haptic devices are basically small robots enabling a user to remotely interact with an environment. An ideal haptic device needs to meet the following requirements to be effective for use in MIS applications: large workspace which increases the manoeuvrability of the surgeon, low inertia and friction which enables the surgeon to move the device freely when it is not in contact, lightweight and comfortable for use that can help reduce fatigue for the surgeon during MIS intervention, statically balanced to remove the need for active gravity compensation, and the capability to apply enough torques to actuators, based on force reflection required for MIS applications. However, providing the aforementioned requirements along with the force reflection capability in all 7-DOFs is almost impossible in practice and sometimes satisfying one may be in conflict with another.

Due to some practical limitations, it might not be possible to reflect forces to the surgeon's hand through a haptic interface in all 7-DOFs or the force reflection capability of the haptic interface might not be sufficient for effective use in teleoperation systems. Sensory substitution is the solution proposed in the literature to replace kinesthetic haptic feedback to the surgeon by some sensory cues. Sensory substitution/augmentation for haptic feedback involves replacing or complementing haptic feedback by other sensory cues such as visual or auditory representation of haptic information (visual or auditory force feedback). Visual display of haptic information, for instance, can provide feedback from tool-tissue interaction based on the size and color of the visual stimuli. Using sensory substitution, the only concern would be an appropriately sensorized instrument to be inserted into the patient's body and measure the interaction of the instrument with the tissue.

Despite the fact that incorporating haptics in RAMIS can make it similar to how the surgeon performs during open surgery, force reflection in 7-DOFs might not necessarily end up with the best performance in MIS [7, 8, 9]. One of the objectives of this research is to explore how many DOFs are required to be reflected to the surgeon's side in different application and determining effective ways of presenting haptic perception for those applications.

1.2 RAMIS Applications

To explore the necessity of haptics in robot-assisted telesurgical systems, two important applications have been considered in this project: soft-tissue palpation, and endoscopic suturing. Various challenges regarding these two applications will be addressed in this project and new approaches will be proposed for use in real-life MIS.

Palpation is one of the most important parts of a surgical procedure which can be used to estimate tissue properties and locate embedded anatomical objects such as tumors, blood vessels, nerves, etc. that are not visually observable during surgical intervention. The most common application of soft-tissue palpation is for tumor localization as the first step taken in cancer treatment (-the focus of the work in this project is on

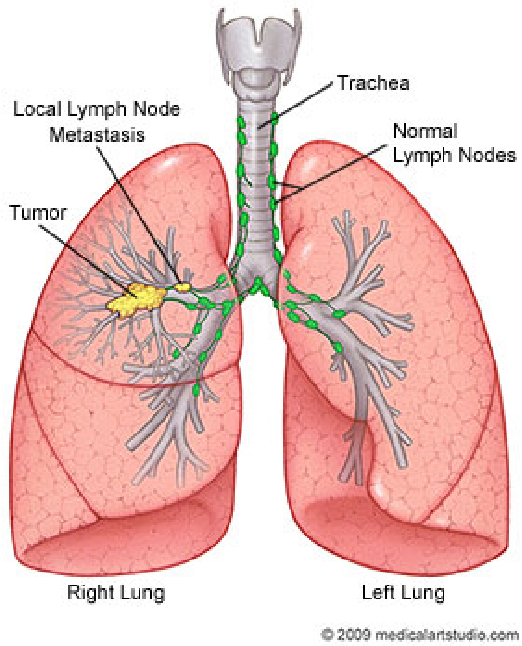

Figure 1.6: A picture of a tumor in lung tissue.

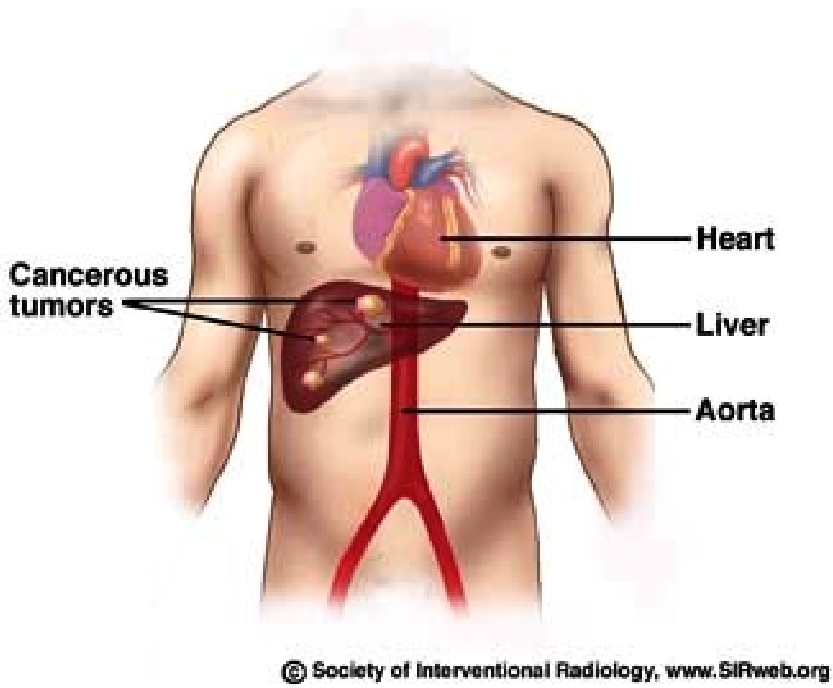

Figure 1.7: A picture of a tumor in liver tissue.

lung cancer, Fig. 1.6, and liver cancer, Fig. 1.7). There are different preoperative and intraoperative methods for tumor localization: methods like MRI and CT which are normally used preoperatively, cannot be used intraoperatively because of tumor shift during tumor resection or ablation. Since the stiffness of a tumor is higher than that of healthy tissue, it can be distinguished as a hard nodule during direct palpation and can therefore be detected intraoperatively. However, this method requires direct access to the diseased tissue which is not possible in minimally invasive surgery. Then, we need to develop sensorized instruments to measure mechanical properties of the tissue remotely. Both force and tactile information from the tissue being palpated can be used for tumor localization in RAMIS. Tactile feedback is more of interest for this application because of the detail information it gives about the palpated area.

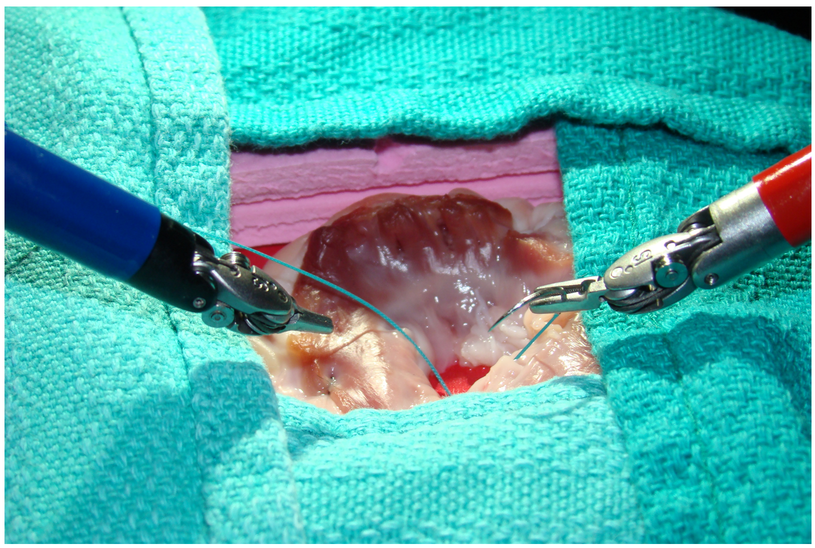

Figure 1.8: Endoscopic suturing using da Vinci needle drivers

.

The other MIS application chosen for this project is endoscopic suturing (Fig. 1.8). Suturing is one of the tasks frequently used in many surgical interventions and is one of the more complex tasks requiring precise and dexterous movements, puncturing and thread tightening [10]. The control of forces applied to sutures is critical in that the forces should be high enough to have a firm knot but should not damage tissue or break sutures. Force feedback during suturing can also help the surgeon to ensure that sufficient force is applied to grasp tissue and suture without slippage and loss of control. The hypothesis here is force feedback can decrease the number of broken sutures and the amount of damage to tissue that may occur during suturing due to over tightening suture knots.

1.3 Previous Work

This section presents some previous work that has been done in the area of haptics for MIS and discusses the challenges of soft-tissue palpation and endoscopic suturing in robot-assisted minimally invasive surgery.

1.3.1 The Role of Haptics in MIS

Many researchers have been working on evaluating the potential benefits of the integration of force feedback in RAMIS systems. Morimoto et al. [11] developed a haptics-enabled setup for laparoscopic surgery and ran some *in vivo* experiments on a pig and showed that using force feedback in robotics-assisted laparoscopic surgery could help to minimize tissue trauma. The importance of kinesthetic feedback was experimentally evaluated in [12] and [13]. The study revealed that robot-assisted surgery could reduce unintentional injuries when appropriate force feedback is available. Wagner and Howe [14] showed that force feedback can be beneficial for both surgeons and non-surgeons; however only surgically trained individuals could improve performance without a significant increase in trial time. Another study by Wagner et al. [15] and Kazi [16] showed that using force feedback could lower the magnitude of the force applied to tissue during a procedure. However, the force feedback did not reduce the task completion time. Reiley et al. [17] showed that graphical displays of applied forces can increase the overall performance mostly for novice surgeons. However, the results in [18] showed that experienced surgeons were able to take more advantage of haptic feedback. Tholey et al. [19] found that using both visual and force feedback led to better tissue characterization compared to each individual method.

Haptic feedback has also been used to develop training simulators by some researchers [20, 21, 22, 23]. Training simulators create a virtual environment for novice surgeons and give them the opportunity to practice as many times as required to become proficient for actual MIS. Haptics has been shown to have a significant role in shortening the process of learning. Judkins et al. [24] showed that using force feedback for training in MIS can cause novice surgeons to apply less force when performing surgery using the da Vinci surgical system in the absence of force feedback.

1.3.2 Tool-Tissue Interaction Measurement

Considerable work has been done on the problem of providing haptic information for minimally invasive surgical applications. One of the main challenges in tool-tissue interaction measurement is the location of the force sensor. Ideally, the force sensor mounted at the tip of the laparoscopic instrument can provide the most accurate measurement. However, the strerilizability and bicompatibility of the modified sensorized laparoscopic tool is an important concern. Moreover, such a force sensor which is capable of measuring tool-tissue interaction in 7-DOFs and can be inserted into the patient's body does not exist yet. The other option is to mount the force sensor outside the patient's body. This solution is also not effective in MIS due to external disturbances such as the friction between the trocar and the instrument, and the effect of gravity of the tool which reduces the reliability of the force readings. According to the nature of haptic perception, a number of techniques have been developed to date to measure tool-tissue interaction [25], [26], [27]. These can be classified into two groups: methods which are based on measuring the interaction force between the instrument and tissue [19, 28, 1] and those capturing tactile information [29] from the contact area between the instrument and tissue. Several researchers [30],[31] have developed sensorized laparoscopic instruments using strain gauges embedded inside the tools to measure the forces applied to the tips of the instruments and thereby to estimate the properties of the manipulated tissue. A high-frequency miniature force sensor was used in [32] to measure tip forces by measuring forces on the shaft of the instrument. Rosen et al. [33] developed a sensorized laparoscopic grasper equipped with a 6-DOF ATI mini force sensor. Piezoelectric sensors have also been used in the design of a sensorized laparoscopic grasper in [19]. Tactile feedback is another source of haptic information which enables a surgeon to get feedback from tissue deformation and pressure distribution on the tissue during surgery. Several researchers have incorporated tactile sensors with laparoscopic instruments to enable surgeons to measure mechanical properties of tissue during an MIS surgical task [29, 34, 30]. In general, tactile sensors are constructed from capacitive elements [35], [36], strain gauges [37] or piezoelectric ceramics [38]. In [31], a sensorized minimally invasive surgery tool has been developed for detecting elastic properties of tissue. Takashima et al. [39] have developed a tactile sensor that measures the tactile force by means of image processing. An array of capacitive elements [40] incorporated into a surgical probe suitable for MIS in [41],[42]. Perri et al. [41] have done extensive tests showing the effectiveness of this hand-held probe and compared the results with those form other traditional tumor localization methods.

1.3.3 Haptic Interface

Different types of haptic interfaces [43],[44] have been designed and developed for use in telesurgery and virtual training including devices that use gloves [45],[46], exoskeletons [47], pens [48], a serial architecture [49], and a parallel architecture [50],[51]. Fig. 1.9 shows some of the currently available haptic interfaces. Serial haptic devices in

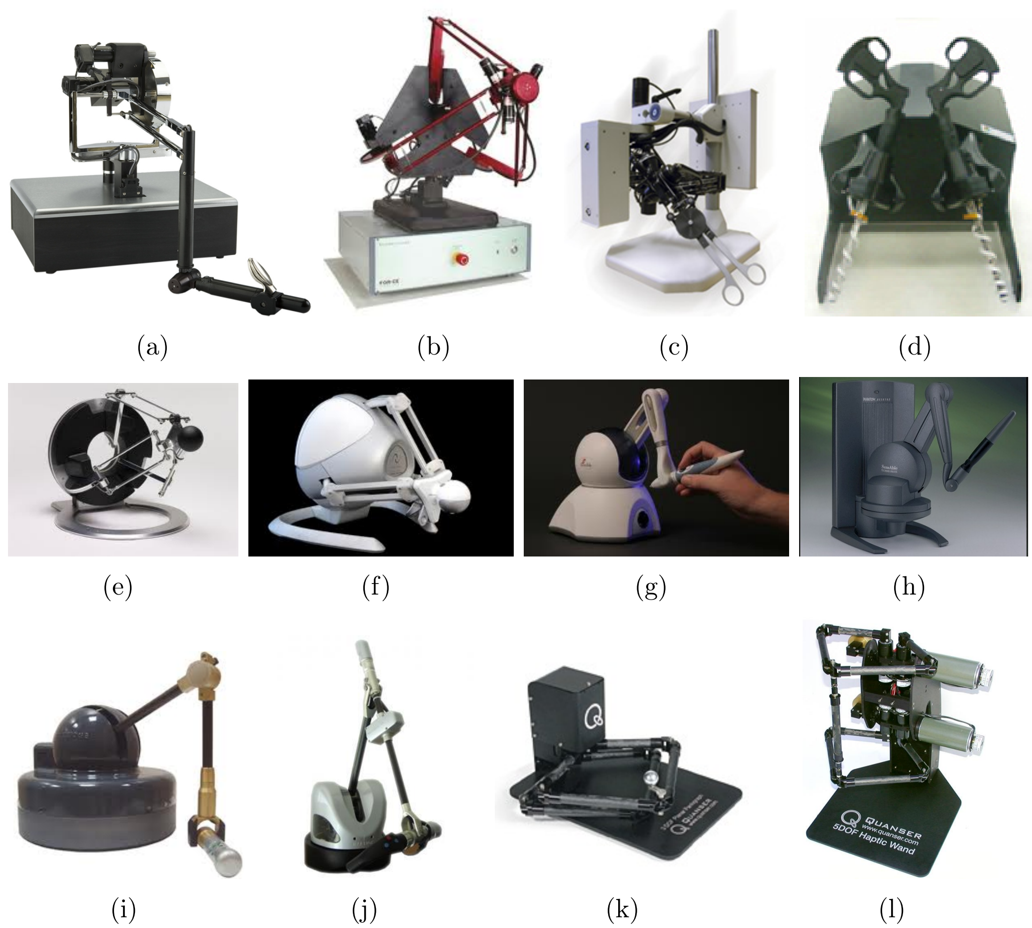

Figure 1.9: Some commercially available haptic devices: a) The Phantom Premium from Sensable, b) Delta from Force Dimension, c) Freedom 7S from MPB Technologies, d) The Laparoscopic Surgical Workstation form Immersion, e) Omega from Force Dimension, f) Novint Falcon form Novint Technoligies, g) Phantom Omni form Sensable, h) Phantom Desktop from Sensable, i) 3-DOD Virtuose from Haption, j) 6-DOF Virtuose from Haption, k) 3-DOF Planar Pantograph from Quanser, l) 5-DOF Haptic Wand from Quanser.

comparison with those with parallel mechanisms have the advantage of having a larger workspace but because of the chain of links, the total inertia increases and the stiffness decreases which results in the lack of sufficient force feedback (Figs. 1.9(g)-1.9(j)). As another example of trade-offs for haptic devices, getting high force feedback and higher stiffness for a haptic device increases its weight and consequently increases the static friction present in the mechanism. Therefore, we need to compromise among the characteristics required for a haptic device and select those with higher priorities. One of the most important features that a haptic device needs to have to be effectively used in a RAMIS application is the capability of force reflection in 7-DOFs: three translational and three rotational DOFs and one DOF for the grasping motion. In [52], a 7-DOF haptic interface for applications in RAMIS is presented. However, the device is capable of force reflection in 4-DOFs and position sensing in 7-DOFs. A haptic interface capable of force reflection in 5-DOFs for MIS is presented in [53]. The design utilizes an off-the-shelf 3-DOF commercial haptic interface [54] and a custom designed grasping and roll assembly. In [55], a 7-DOF haptic interface based on a parallel kinematic structure is described. The device has a large number of links (21) arranged as a dual 3-legged structure and is capable of force feedback in 7-DOFs. The Freedom 7S, shown in Fig. 1.9(c) (MPB Technologies, Montreal, Canada) is another haptic interface with a 7-DOF force reflection capability [56]. The device is available with a scissor-like end-effector or an optional handle or a scalpel. However, this device is capable of very limited continuous force reflection due to the direct-drive actuators employed in the design. Another commercial haptic device with 6-DOF force reflection and 7-DOF position sensing is the PHANToM, shown in Fig. 1.9(a), [49] (Sensable Technologies, MA, U.S.A.). The grasping motion in this device is passive and is available either as a thumb-pad or a scissor-like handle. Based on a parallel kinematic structure for positioning and a serial-chain structure for orientation, Omega [57] is another commercial haptic interface capable of force reflection in 7-DOF (Fig. 1.9(e)). These haptic devices have limited applicability in MIS research due to one or more of the following shortcomings: insufficient DOFs, limited continuous force reflection, limited workspace or high cost.

1.3.4 Sensory Substitution

As a remedy for limited continuous force reflection for haptic interface, sensory substitution can be effectively used by replacing haptic feedback by other sensory cues. Sensory substitution can also be useful where direct force reflection in the presence of time delay causes instability in bilateral teleoperation system. On the other hand, a combination of haptic feedback with another modality might increase the performance of the surgeon in RAMIS. Different modalities have been proposed in the literature; most commonly method is visual presentation of the force or tactile feedback. A visual presentation through some LEDs has been used by Tavakoli et al. in [58] to monitor the intensity of the force applied by the laparoscopic instrument to the tissue. Visualization of the pressure data obtained from the tactile sensors in palpation application is used in [59] to detect the location of tumor in diseased tissue. In [42], Perri et al. combined visual force feedback with visual tactile feedback to get better performance of using tactile feedback for tumor localization. A finite element method was used in [60] to monitor the embedded object in the tissue in the form of stress graphs and tactile maps. Dargahi et al. [61] proposed a signal processing based approach to display tactile information by means of a color coding method. In [62], a tactile stimulator was designed to give the sense of touch to the operator through an array of pins each actuated independently via software. A similar approach has been used by others but different actuating methods have been implemented. Ottermo et al. [63] designed an electromechanical system to actuate the pins. A pneumatic balloon-based system was used in [64] to provide tactile feedback to the fingers of the surgeon during robotic surgery. Auditory display is another substitution to reflect the haptic information to the surgeon. However, the continual noise in operating room was found distractive by many surgeons. Different force feedback modalities including auditory, visual and combination of these two were considered in [65] and [26] for performing knot tying task. Vibro-tactile feedback is another example of sensory substitution used in [66]. In this method, an array of vibrating pins is used where the amplitude or the frequency of vibration depends on the magnitude of the measured forces. A totally different way of sensory substitution was proposed by Fischer et al. [67] based on the level of tissue oxygenation. They found out that trauma occurs in tissue when the tissue oxygenation level decreases below a certain level and then designed a sensor to measure the oxygenation level of tissue.

1.3.5 Haptics-Enabled Teleoperation Setups Developed for MIS

Some master-slave teleoperation systems have been reported in the literature with force reflection capability developed for exploring the effect of haptics in RAMIS. Tavakoli et al. [68, 69, 7] developed a 5-DOF master-slave setup which was sensorized using some strain gauges and a single-axis load cell integrated into a custom-designed endoscopic instrument. Cavusoglu et al. [70] and Mayer et al. [71] designed electromechanical master-slave systems for MIS procedures. The telesurgical workstation developed in [70] is a master-slave telerobotic system designed for testing in animal experiments as well as testing with ex vivo tissue and in training box. This system has two pairs of 6-DOF master and slave robotic manipulators, designed for laparoscopic surgery. The slave manipulators have 2-DOF wrists inside the body in addition to the 4-DOFs of motion through the entry ports which are actuated by external gross motion platforms. The master workstation consists of two Phantom1.5 haptic devices where 3 actuated DOFs were modified to be kinematically similar to the wrist configuration of the slave manipulators. A robot manipulator was developed in [72] for surgical telemanipulation. The main feature of this robot is the capability of measuring tool-tissue interaction without the need of any miniaturized force sensor to be integrated into surgical instruments. To do so, Zemiti et al. [72] attached a Nano ATI force sensor inside a trocar and modified that in such a way that friction between the trocar and instrument shaft has no effect on force measurement at the tip of the instrument. Tadano and Kawashima [73] developed a master-slave setup for MIS including a 3-DOF manipulator for supporting forceps actuated by pneumatic cylinders and a master manipulator which has been designed based on a delta mechanism and a gimbal mechanism and equipped with a force sensor and motors with reduction gears. A robotic surgical system with two portable surgical robots, called Raven, was developed at the BioRobotics Lab., University of Washington (Seattle, WA) [74]. This robotic system works along the same principle as the da Vinci with two articulated, tendon driven arms, each holding a stainless steel shaft for different surgical tools. The force sensor integrated into this robot allows to measure the tool-tissue interaction at the tip of the laparoscopic instrument. The German Aerospace Center (DLR) [75] has developed its second generation robotic arm (MIRO) that is used in its MiroSurge robotic system. This system consists of a master console including two Omega 7 haptic devices and a surgical platform including three surgical robots (MIRO); two for carrying surgical instruments which are equipped with miniaturized force/torque sensors to capture interaction forces between instruments and tissue and one for guiding a stereo video laparoscope.

Different simulators have been also designed in the literature exploring the effect of haptics in the process of training. Wu et al. [23] developed a surgical training simulator for robotics-assisted Pyeloplasty which has been used to correct a kidney ureteropelvic junction obstruction. This simulator provides visual and haptic feedback to the trainee during doing the procedure. In [20], a virtual-reality motor-skills simulator was created for surgical training purposes. This haptics-enabled surgical simulator has been designed based on the SPRING software framework aiming at evaluating trainees' performance for some surgical procedures. Maass et al. [21] presented a flexible interface for general force feedback applications in virtual-reality surgical training systems. This interface is capable of controlling several different force feedback hardware systems such as the SensAble PHANTOM, the Laparoscopic Impulse Engines from Immersion, and the VS-One virtual endoscopic surgery trainer. A virtual surgical practice environment has been developed in [22] for robot assisted minimally invasive neurosurgery. This simulator has been facilitated with haptic rendering and collision detection algorithm and enables the surgeon to do virtual neurosurgery using a virtual robot on a 3D model of the patient's brain while giving him/her the feeling of the interaction forces through a haptic device.

1.3.6 RAMIS Applications

Tumor Localization in Soft-Tissue Palpation

Tumor localization has been the subject of considerable research in the literature in recent years. In order to localize tumors in diseased tissue, haptic feedback in both forms of tactile sensing [34],[30] and force reflection [76],[77] have been demonstrated in the literature. Kinesthetic and visual force feedback were used to detect lump in an artificial tissue in [68] and [69]. The setup in this work was equipped with a number of strain gauges and a single-axis load cell integrated into a custom-designed endoscopic instrument to measure interaction forces. A modified da Vinci Surgical System was used in [77] for soft-tissue palpation. In this work, different force feedback modalities have been used for tumor localization including direct force feedback, graphical force feedback and a combination of these two. A tactile sensing instrument was used in [41] to localize tumors by an operator in a minimally invasive training box. A comparison between palpation with gloved fingers, conventional laparoscopic instruments and a sensorized laparoscopic instrument was presented in [34]. The sensor array at the tip of the sensorized instrument provided the surgeon the location of the tumor with visually presented tactile information.

Although both force feedback and tactile feedback have been used for tumor localization, each suffers from some disadvantages: It has been shown that the overall performance of a tactile sensor is highly dependent on consistency of the force applied to the sensor[78], [79]. If too little force is applied, the tactile sensor may not make proper contact with the tissue or may not deform the tissue sufficiently to be sensitive to an underlying tumor. On the other hand, excessive force applied to the tissue may damage the tissue and also cause artifacts to appear as tumors and lead to false positives. Force reflection based methods for tumor localization also have some restrictions in practice: the main issue with force feedback in tumor localization is to control the depth of palpation during the task. If the operator pushes the palpation instrument hard on tissue, he/she may feel higher forces reflected to his/her hand and recognize it as a tumor when there is no tumor in that area. Then, tactile feedback or force feedback alone cannot be effectively employed to localize tumors in an MIS palpation task. Some work has been reported on integrating tactile sensing with force feedback for tumor localization. In [80], experiments were conducted to determine whether providing visual force feedback (VFF) to the operator can improve the performance of a tactile sensor in a directly manipulated system. However, the exploration force was measured by the same sensor used as the tactile sensor. therefore, if a false positive is detected because of improper contact between the sensor and the tissue, the exploration force measured by the sensor would not help to correct this failure. Feller et al. integrated an ATI force sensor with a tactile sensor in [79]. Although their setup is not suitable for use in MIS, but they have shown that using force feedback can significantly reduce the force applied to tissue during exploration for tumors. A similar study with a finite element model of a compliant environment was conducted by Wagner et al. [81] but not specifically in the context of MIS.

Haptics-Enabled Endoscopic Suturing

The problem of incorporating haptic feedback in robot-assisted endoscopic suturing has been also investigated by some researchers [82, 58, 6]. Peddamatham et al. [66] studied the effect of vibrotactile feedback for a needle insertion task. Some participants were asked to perform the task in three modes; manually (by hand), using a surgical manipulator in the presence of vibrotactile feedback and with no feedback. The results showed that vibrotactile feedback could reduce the magnitude of force in the perpendicular direction to the suturing surface, but not the forces along the suturing surface. However, the task took longer time to complete in the presence of vibrotactile feedback. Kitagawa et al. [65] explored the effect of different force feedback modalities in a knot tying task including no force feedback, visual force feedback, auditory force feedback and the combination of auditory and visual force feedback. They concluded that visual force feedback could increase the performance of knot tying; however, auditory feedback could only improve the performance if it was presented in a discrete mode. Continuous auditory feedback as mentioned earlier could be a distraction for the surgeon during the procedure in an already noisy operating room environment. In [83], a tension measuring device was developed to measure the forces applied during knot tying. These forces were then visualized and given to some participants to see how useful they could be to increase the performance of the knot tying task. The results showed that, this method results in fine sutures without breakage while consistent forces are applied during the procedure. Akinbiyiet et al. [6] presented an augmented reality system for sensory substitution for the knot tying task. The participants were asked to tighten a loose knot. In the experiments, the force applied by the user during knot-tying was measured by strain gauges embedded inside the shaft of the da Vinci tools and visually presented to him/her along with 3D images of the experimental environment. A kinematic tool tracker was used in this work to track the location of the moving instrument tip and to overlay the visual representation of force levels on top of that. The results showed that the augmented reality system decreases the number of broken sutures, decreases the number of loose knots, and results in more consistent application of forces. Judkins et al. [24] showed that if novice surgeons were trained using a setup providing grasping force feedback, they would be able to apply less force during some surgical procedures such as needle passing and suture tying even if the force feedback is not available anymore. Reiley et al. in [17] showed that graphical displays of applied forces during the knot tying task reduced suture breakage and increased the overall performance mostly for novice surgeons.

1.4 Contributions and Thesis Outline

In this section, we briefly describe the contribution of the research project carried out to address the aforementioned challenges and then present outline of the thesis.

Despite the advances in the field of haptics in RAMIS, a master-slave teleoperation setup which is capable of providing force feedback in all 7-DOFs required for MIS has not been developed yet. The lack of fully haptics-enabled setup in RAMIS is mostly because of the lack of an appropriate haptic interface with force reflection capability in 7-DOFs and the lack of a force sensing system to accurately measure tool-tissue interaction. The main contribution of this work is to develop a research platform capable of measuring forces in 7-DOFs using embedded sensory system and reflecting them to the operator's hand through a modified 7-DOF haptic device. This setup enables the exploration of the effect of haptics in various single-arm as well as dual-arm teleoperation surgical scenarios. The test-bed also enables the evaluation of the effect of replacing haptic feedback by other sensory cues such as visual representation of haptic information (sensory substitution) and the hypothesis that surgical outcomes may be improved by substituting or augmenting haptic feedback by such sensory cues. The 7-DOF haptics-enabled setup developed in this project is used to explore the effect of tactile perception as well as kinesthetic perception for two important applications; Tumor localization in soft-tissue palpation and endoscopic suturing.

The first application which has been considered in this project is soft-tissue palpation for localizing tumors in lung and liver cancer. In this application, both force feedback and tactile feedback are used to localize tumors in diseased tissue through our single-arm teleoperation system. Although many force feedback palpation applications have been implemented through teleoperated (master-slave) systems, most of the tactile sensing instruments developed for the application have not been tested in RAMIS systems. Moreover, the consistency of exploration force in the palpation direction has always been the main concern in tactile sensing tumor localization. Using our master-slave teleoperation system for tumor localization, our work explores how force feedback can be incorporated with tactile sensing to provide consistent palpation and to improve the performance of tumor localization when the tissue is palpated in a minimally invasive manner. The first objective in this work is to compare the performance of tactile feedback with force feedback to localize tumors in bovine livers or lungs. During experiments, tactile feedback is presented in a visual form to show the pressure distribution on the palpated area. Force feedback can be either reflected to the operator's hand or visually presented on a screen.

The problem of incorporating haptic feedback in robot-assisted endoscopic suturing is the second application that is considered in this project. In this project, we explore the effect of force feedback in 7-DOFs on the performance of suturing task (mimicking what occurs in real life scenarios where the surgeon performs suturing in open surgery) and we also consider a very complex task with different presentations of force feedback: no force feedback, direct force reflection and sensory substitution. In this work, sensory substitution is provided by a bar indicator whose height varies with the magnitude of the interaction forces between the instrument and its environment (tissue, needle or thread) which is added to the camera vision overlooking the surgical field. The experiments designed for this work include all the actions needed for a complex suturing task while comparing the performance of suturing for three different presentation modes of force feedback: no force feedback, visual force feedback and direct reflection of the force feedback. To the best of our knowledge, this is the first work that explores the effect of direct haptic feedback in 7-DOF for a suture-manipulation task in robotics-assisted master-slave teleoperated system for MIS.

The setup developed in this project can not only be used to explore the effectiveness of haptics in RAMIS applications, but can also provide novice surgeons the opportunity to practice so as feel comfortable using a RAMIS system in real-life applications and to increase their dexterity. Using the force feedback capability of this setup makes the process of learning faster and decreases possible damage to tissue.

The main contributions of the work presented in this thesis can then be summarized as follows:

1. Designing, developing and integrating a 7-DOF haptics-enabled master-slave robotic research platform for minimally invasive surgery that is capable of providing both kinesthetic and cutaneous feedback.

2. Performing detailed analysis of the kinematics, statics, and dynamics for the 7-DOF Haptic Wand.

3. Design, simulation and real-time implementation of complex control algorithms and safety system for the 7-DOF dual arm teleoperation system.

4. Quantitative assessment of the effect of force feedback, in different scenarios, on the performance of tactile sensing tumor localization in RAMIS.

5. Development of a closed-loop semi-autonomous force control method for ensuring the consistency of the exploration force for tactile sensing tumor localization in RAMIS.

6. Investigation of the effect of force feedback in both forms of direct reflection and sensory substitution in all 7 DOFs for a suture manipulation task using an experimental setup close to the one that could be applied for real RAMIS.

The outline of the thesis is shown diagrammatically in Fig. 1.10. The organization of this thesis is as follows:

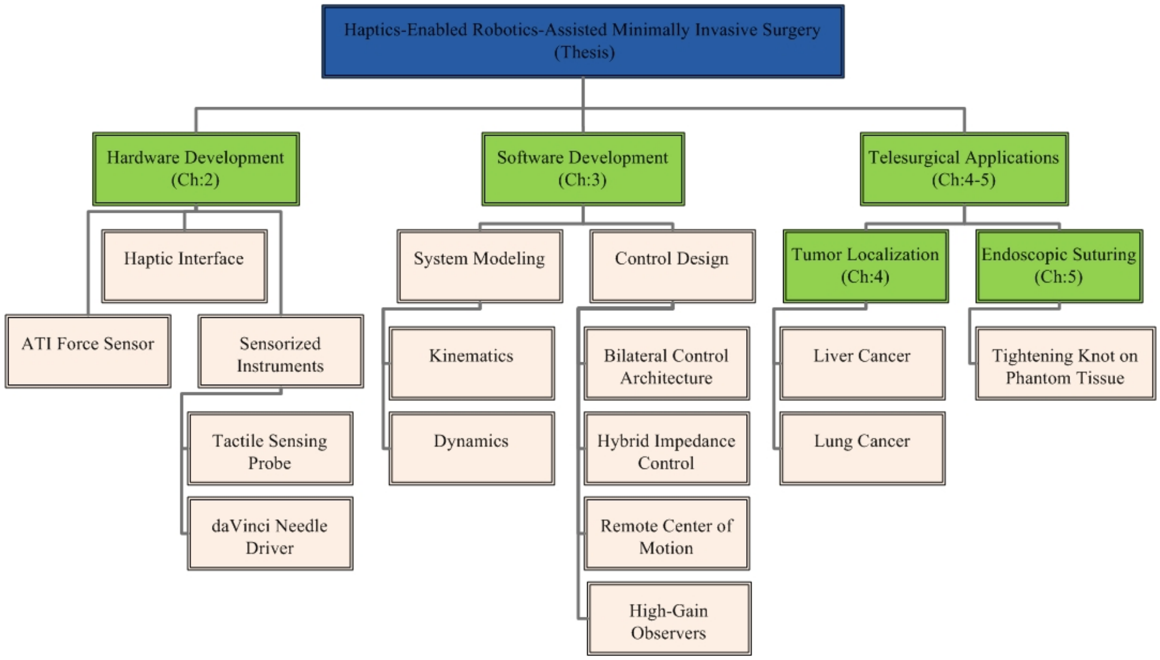

Figure 1.10: Thesis outline.

Chapter 2 describes our dual-arm master-slave teleoperation setup and explains the hardware modifications which have been done on the haptic interface and laparoscopic instruments. The sensory system which is used to measure the interaction force acting at the tip of the instruments is also introduced and calibration software which is developed to measure the forces as accurate as possible is explained thereafter.

Chapter 3 describes the software development for the dual-arm master-slave teleoperation system including system modeling and control design. Kinematics and dynamics models of the robot manipulators are extracted in this chapter and the control design algorithms that are used to control the behavior of the robot manipulator when in contact with their environments are explained in details.

Chapter 4 presents a soft-tissue palpation application for tumor localization. The first work presented in this Chapter shows the necessity of force feedback for tactile sensing tumor localization in RAMIS. Different modalities are used to address tumor localization problem in RAMIS; tactile feedback with visual presentation of pressure distribution over the tissue palpated, force feedback directly reflected to the operator's hand, visually presented force feedback, visual presentation of tactile feedback in a force controlled environment when it is reflected to the operator's hand and then when it is visually presented on a screen. These modalities are explored in the case of tumor localization in liver tissue. The second work presents a new method for tumor localization in lung cancer where a hybrid impedance control approach is used to resolve the consistency problem of the exploration force on the tissue in the palpation direction.

In Chapter 5, we evaluate human performance of a suturing task in three modes: without force feedback, with visual force feedback and with direct force reflection on the surgeon's hand. The suturing task is divided into two different phases: stitching phase and knot tying phase. The stitching phase includes four subtasks; grabbing the needle in order to position the needle in the right place before inserting it in the tissue, inserting the needle with penetration of the tissue, grabbing the tip of the needle after penetration of the tissue, pulling the needle through the tissue. The knot tying phase is also divided into three subtasks: looping the wire around one of the instruments, grabbing the wire prior and directly after looping, pulling the loop over the instrument and tightening the knot. In this chapter, we focus on the effect of force feedback in both forms (haptics and sensory substitution) in the performance of knot tightening in RAMIS endoscopic suturing. Seven participants are asked to secure the second throw of surgical knots using our dual-arm teleoperation system.

Chapter 6 summarizes the main contributions of the thesis, and provides concluding remarks about the main results of the paper and suggests possible directions for future work.

1.5 Publications and Intellectual Property

Chapters 2 and 3 have resulted in two conference papers and one journal paper: one paper published in the proceeding of the IEEE/RSJ International Conference on Intelligent Robots and Systems (IROS); one paper published in the proceeding of the IEEE International Conference on Biomedical Robotics and Biomechatronics (BIOROB2010), and one journal paper which is currently under preparation for submission to International Journal of Robotics Research. Chapter 4 includes the results of three papers, one that has been published in the proceeding of IEEE International Conference on Robotics and Automation (ICRA2010), another has been accepted for publication in the proceeding of IEEE International Conference on Robotics and Automation (ICRA2012), and the third which is submitted for the publication in the Transactions on Haptics and is under the second review. Chapter 5 has also resulted in two papers: one which has been accepted for publication in the proceeding of the International Conference on Biomedical Robotics and Biomechatronics (BIOROB2012), and the other which is currently under preparation for submission to the International Journal of Robotics Research.

Chapter 2

Dual-Arm Teleoperation Setup

Fig. 2.1 shows our haptics-enabled dual-arm teleoperation setup which consists of two Mitsubishi PA10-7C robots as the slave system controlled remotely over a dedicated network through two customized Quanser Haptic Wands [84] as the master interface. The Haptic Wand used in our test-bed is a 7-DOF haptic device which is capable of position and force reflection in three translational DOFs, three rotational DOFs, in addition to grasping motion. This device originally had 5-DOFs [84] and was modified at CSTAR to add yaw and grasp motions [85]. At the other end, two 7-DOF Mitsubishi PA10-7C robots were employed as the slave arms in the teleoperation test-bed. Each application requires specific tools to be mounted on the robot arms as the end effectors. For suturing application, two daVinci needle drivers, as seen in Fig. 2.1, have been sensorized and mounted on the 7-DOF Mitsubishi PA10-7C robots. The sensorized instruments enable us to measure the grasping forces at the tips of the instruments. For palpation application, a tactile sensor has been used and attached to a probe to capture the pressure distribution over the tissue. This tactile sensing instrument is used for tumor localization in soft-tissue palpation.

The implementation of the controllers was done on two Windows-based systems, one for the master and the other for the slave. The communication between the two computers was done using the User Datagram Protocol (UDP). All control algorithms were implemented on the QuaRC Real-Time software which automatically generates real-time code directly from Simulink designed controllers targeting Windows [84]. All of the controllers for the master and slave manipulators were implemented at a sampling frequency of 1 kHz. The communication between the master and the slave PCs and transmission of the force and position data were also made at the same rate.

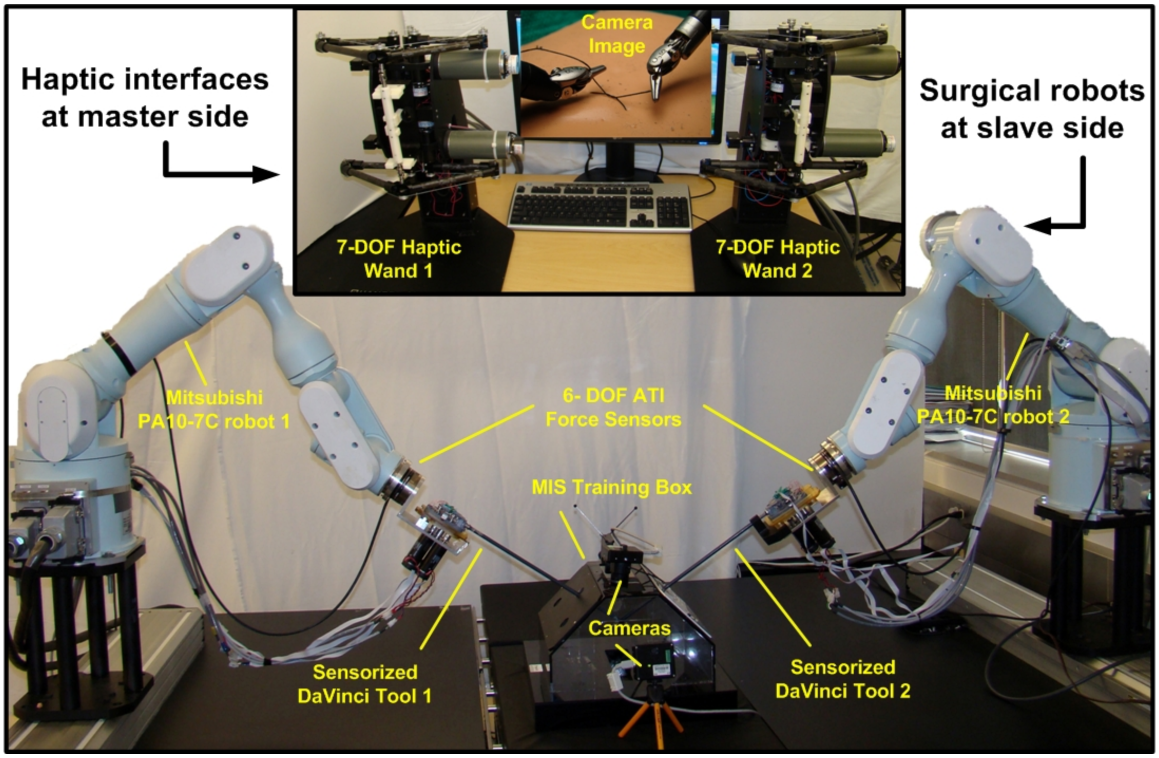

Figure 2.1: Dual-arm master-slave teleoperation robotic setup.

2.1 The Master - Haptic Wand

The kinematic structure of the original Haptic Wand utilizes dual 5-bar linkage mechanisms interfaced to the output handle through two Cardan joints. The 5-bar linkages are built of a carbon-fiber material to minimize inertia. This device employs direct-drive actuators to minimize friction and maximize transparency. Each closed-chain 5-bar linkage mechanism is actuated through the use of two shoulder motors which are supported on a single DOF waist joint resulting in a kinematic chain with three DOFs. The addition of a Cardan joint at each end of the handle constrains the total number of DOFs of the haptic interface to five (three translation and two rotation: roll and pitch) with a redundant waist joint that eliminates a workspace singularity of the mechanism. The motion about the handle axis in the original device is passive and unencoded. By this structure, the original Haptic Wand is capable of force reflection in 5-DOFs (see [48] for further schematics).

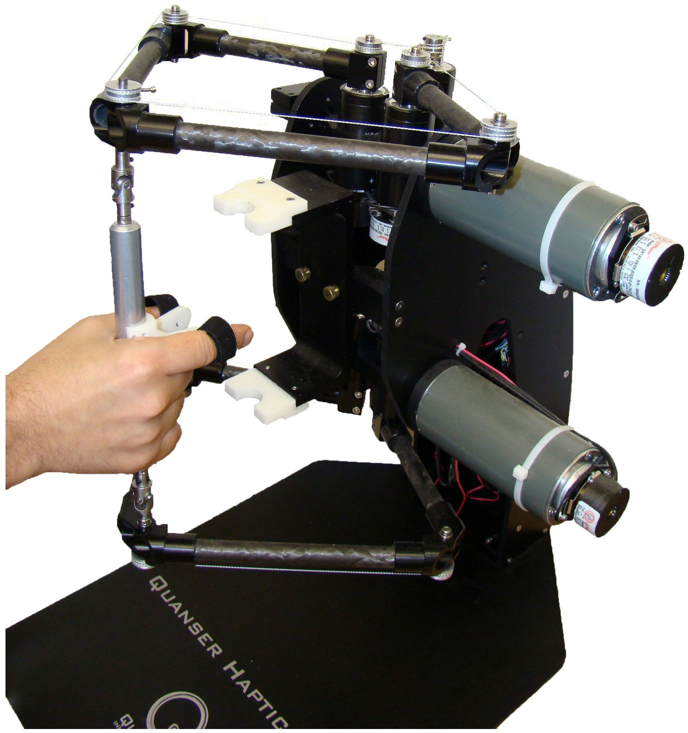

Figure 2.2: Modified Haptic Wand.

2.1.1 Hardware Modifications

The original Haptic Wand was found to have limited applicability in MIS due to the lack of force reflection in the yaw direction and grasping. Thus, it was required to modify the device to include force reflection in those DOFs. Various design modifications were explored and their effects on the device performance were examined. A common approach would have been to redesign the output handle to include two actuators that would provide decoupled force reflection in the yaw and grasping. This approach however, would result in increased handle mass and therefore higher inertia and reduced force reflection capability and transparency. Even though it was possible to compensate for the increased mass to a certain extent by incorporating extra counterbalance weights, the particular kinematics of the Haptic Wand made it difficult to fully eliminate the effect. Increased handle mass would also have made it difficult for the user to manipulate the device for prolonged periods, a common requirement in surgical scenarios. A novel and more elegant approach was devised to include the required DOF to the Haptic Wand. In this approach, the output handle of the haptic interface was designed to have two split sections, each attached to a corresponding pinch lever (end effector). Two handle drive actuators (Maxon Motor RE35) were

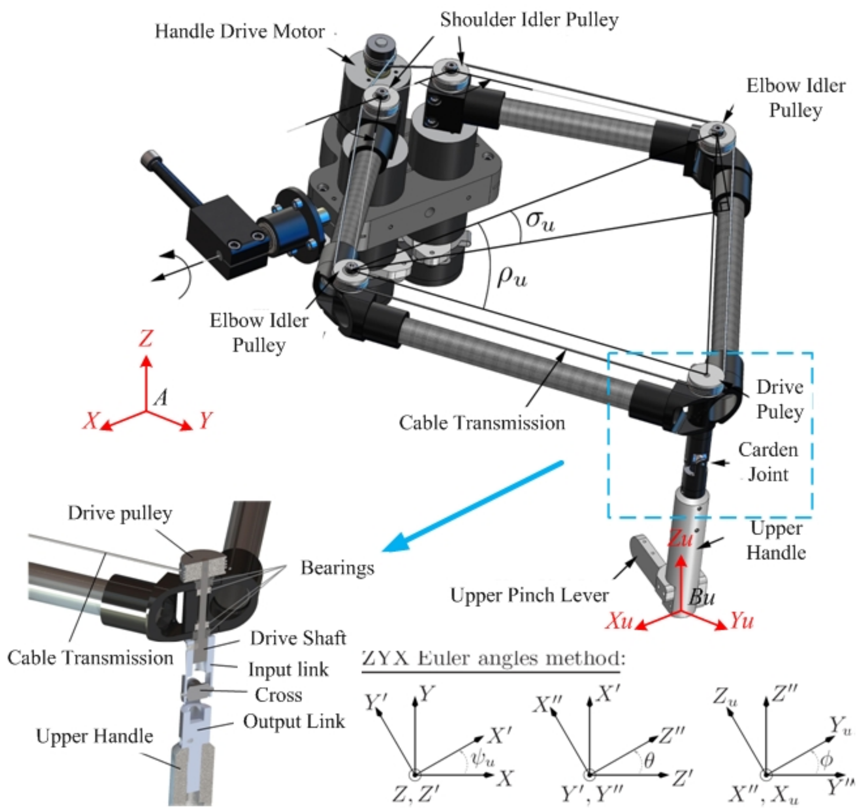

Figure 2.3: CAD rendering of the upper handle drive.

included in the mechanism, each independently controlling the corresponding handle. The resulting design is symmetrical about a horizontal plane and required minimal modifications to the existing components of the Haptic Wand. Figure 2.2 shows the modified 7-DOF Haptic Wand. Figure 2.3 also shows the close-up view of one 5-bar linkage mechanism with its associated handle drive transmission. A cable transmission was utilized to transfer motor torques to the drive pulley in this design. This approach had the benefit that it allowed the handle drive motor to be located on the other side of the waist axis and therefore act as a partial counterweight (fully balanced in the middle of the workspace) to the 5-bar linkages. The introduction of the handle drive motors as partial counterweights eliminated the need of the original counterweights, which were therefore removed from the device. Four idler pulleys were introduced in each 5-bar linkage at the shoulder and elbow joints to assist with cable routing. The cable windup drum on the handle drive motor was designed as having two split sections which facilitated in proper tensioning of the cable. One end of the cable loop was terminated on the first windup drum section, wrapped over shoulder and elbow idler pulleys a few turns and then terminated at the drive pulley. Similarly, the other end of the cable loop was terminated on the second windup drum section, wrapped over the other shoulder and elbow idler pulleys a few turns and then terminated at the drive pulley to complete the loop. The actuator torque was therefore transferred from the handle drive motor utilizing the cable transmission to the drive pulley in a continuous fashion. The sectional view of the Cardan joint drive of each 5-bar linkage has also been shown in Fig. 2.3. The drive shaft is supported by four idler bearings to create a passive joint with the 5-bar linkage and therefore can be independently rotated with respect to the 5-bar linkage. At each end, the drive shaft is firmly attached to the drive pulley and the input link of the Cardan joint, respectively. The output link of the Cardan joint is firmly attached to the handle and therefore actuator torque is transferred from the drive pulley through the drive shaft, through the Cardan joint to the handle and to the corresponding pinch lever. The

Table 2.1: 7-DOF Haptic Wand characteristics

7-DOF Haptic Wand Workspace	
Translation (mm)	480W x 450H x 250D
Rotation (deg)	±85 (roll) ±65 (pitch) ±160 (yaw) 90 (grasp)
Maximum Continuous/Peak Force	
Force (N)	2.3/7.7 (X) 2.1/7.0 (Y) 3.0/9.0 (Z)
Torque (N.mm)	230/750 (roll) 250/810 (pitch) 113/368 (yaw) 113/368 (grasp)

upper and lower handles are coupled to each other through a passive joint (with its axis aligned with the longitudinal axes of the handles). In a typical setting, the user would hold the pinch levers utilizing the thumb and the index finger and could utilize the remaining fingers and palm to hold onto one of the handles for a better support. Velcro straps are attached to the pinch levers to maintain a firm contact with user's fingers at all times. The pinch levers were designed to be removable and can be easily replaced with other types of end-effectors (such as scissor handles), if required. Fig. 2.3 also shows the translational and rotational motion (Euler angles method) of the Haptic Wand. The Euler angles method is a series of three consecutive rotations that define the orientation of frame Bu (attached to to the upper pinch lever, Fig. 2.3) from the reference frame A (attached to the base of the Haptic Wand). The chosen method is ZYX, which means that the first rotation is about the axis Z, the second rotation is about the axis Y' and the third rotation is about the axis X'' (frames X', Y', Z' and X'', Y'', Z'' are just intermediate virtual frames).

The joint angles of the 7-DOF Haptic Wand are measured by a digital optical encoder installed on the motor shafts. The haptic device workspace is defined in Table 2.1. This table also shows the maximum continuous and peak force/torques along the translational and orientational directions at operating position. Referring to Fig. 2.3, the home and operating positions of the Haptic Wand end effector in the world frame are defined at $y = 124\,mm$ and $y = 210\,mm$, respectively (they are located at zero for the other 6-DOFs).

2.2 The Slave system

The slave side of each single-arm teleoperation system is composed of a Mitsubishi PA-10 robot arm, a sensorized instrument at the robot end effector which can be either a da Vinci tool or a tactile sensing instrument (TSI) mounted on the wrist of the robot arm, and an ATI force sensor which is mounted between the arm and the instrument to measure the interaction forces at the tip of the instrument.

2.2.1 Mitsubishi PA10-7C Robot

The Mitsubishi PA-10 robot arm is a 7 degree-of-freedom arm with an open-control architecture manufactured by Mitsubishi Heavy Industries (Fig. 2.4). The four-layer control architecture for each 7-DOF Mitsubishi PA10-7C robot consists of the host control computer, a motion control card, a servo controller and the robotic arm. A flow chart for the control system is also shown in Fig. 2.4. The host computer communicates with the servo controller of the robot over the ARCNET protocol though the motion control card. However, the problem with the motion control card provided by Mitsubishi is that it does not support open-architecture programming. The robot's open-architecture (hardware and software) provides the possibility to control and modify any aspect of the robot's behavior as well as to include new sensor information in the control loop. Using the PCI20U ARCNET card from Contemporary Control Inc. [86], the host computer can communicate with the servo controller while supporting open-control architecture. To reduce the amount of noise and to provide fast data transfer rate, the communication between the servo driver and the host computer is by means of an optical fiber. The host computer communicates with the PA10-7C arm at a sampling rate of 1 kHz.

The robot joints are actuated by three-phase AC servo motors and harmonic gear transmissions. The harmonic drive assemblies in the Mitsubishi PA-10 are manufactured by Harmonic Drive Systems Inc. (model CSF-32-50-2A-GR for joints 1 and 2, model CSF-32-50-2A-GR for joints 3 and 4, and CSF-32-50-2A-GR for joints 5, 6, and 7). Joint positions are measured through resolvers at the joint output axis, with a resolution of 0.000439 over ± 3 output revolutions. Control of the robot can be achieved in either 'velocity mode' or 'torque mode'. In 'velocity mode', the desired velocity for each joint is sent to the servo driver from the host computer. A high-gain digital PI feedback loop running at 1538 Hz on the servo driver controls the joint velocity. In 'torque mode' the desired joint torque is sent to the servo driver. To get full advantage of the well-tuned built-in controller for the Mitsubishi PA10-7C, we control the robot in velocity mode in this project.

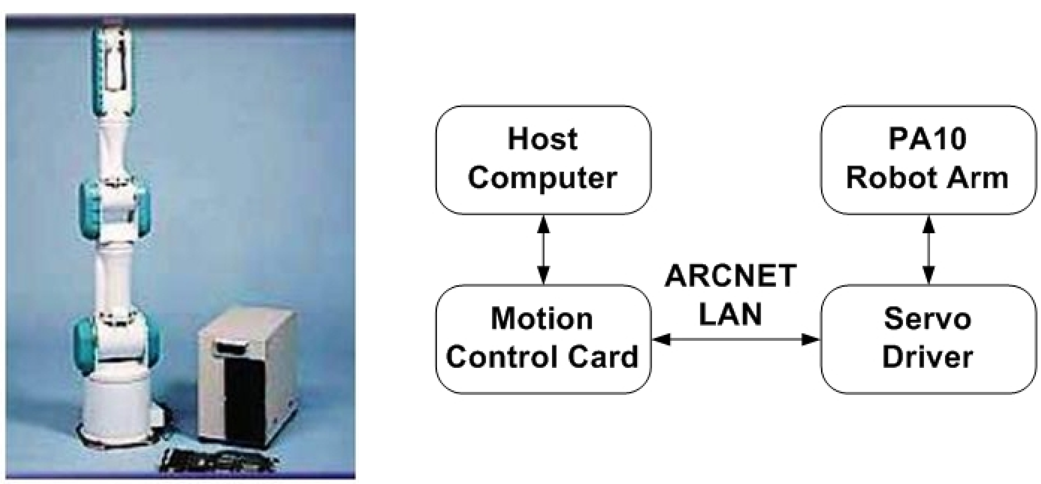

Figure 2.4: Mitsubishi PA10-7C robot arm and servo driver (left), and flowchart of the Mitsubishi PA10-7C four-layer control architecture (right).

2.2.2 Sensorized Instruments

As stated earlier, two types of instruments were used in this project. The sensorized da Vinci tool which is used for suturing task and the tactile sensing instrument which is used for tumor localization in soft-tissue palpation [41].

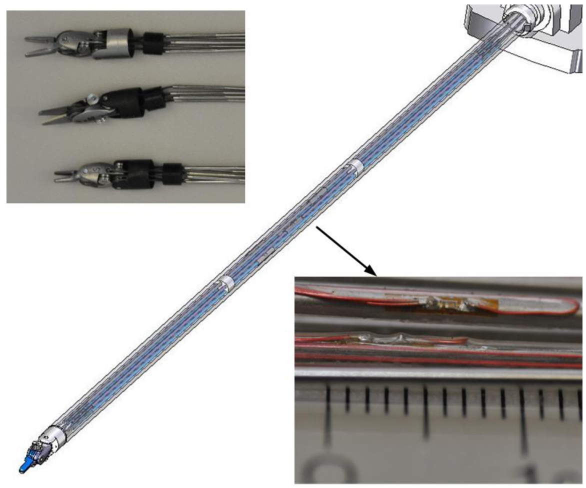

Figure 2.5: Sensorized instruments showing various tips and a closeup of the strain gauges applied to the cable shafts [1].

Sensorized da Vinci Tool

In this section, we describe the modifications that have been made to a cable-actuated endoscopic instrument to integrate strain gauges for grasping force sensing. Initially, the motion of the instrument wrist is controlled through four pairs of cable-shaft-cable assemblies for each of the 4 DOFs (roll (θ) about the instrument axis, pitch (ϕ), yaw of gripper 1 (ψ_1) and yaw of gripper 2 (ψ_2)). In order to measure the forces acting at the tip of these instruments, strain gauges were added to three of the pairs of cable shafts (see Fig. 2.5). The roll about the instrument axis would cause the wires from the strain gauges to tangle and so the cable assemblies controlling this extra DOF were eliminated from the design. Instead, this motion is provided by the Mitsubishi PA10-7C robot and the interaction force for this motion is also captured by the ATI force sensor mounted between the robot arm and the instrument. Six EA-09-015DJ-120 strain gauges (Vishay Micro-Measurements) were mounted and rigidly glued to stainless steel shafts (1.1 mm in diameter) belonging to the six remaining cable assemblies. The gauges on each cable pair were connected in a Type II Half Bridge configuration using Quanser strain gauge amplifiers. A Quanser Q8 Hardware-in-the-Loop board is responsible for capturing the signals from the amplifiers. Customized software running on a computer serves to capture, process and record the information from the strain gauges for calibration. The calibration [1] of the strain gauges was performed using a customized holder for the instruments that allows applying forces in each of the degrees of freedom individually in the positive and negative directions (Fig. 2.6). Forces were applied to the tip of the instruments in 100 g increments from

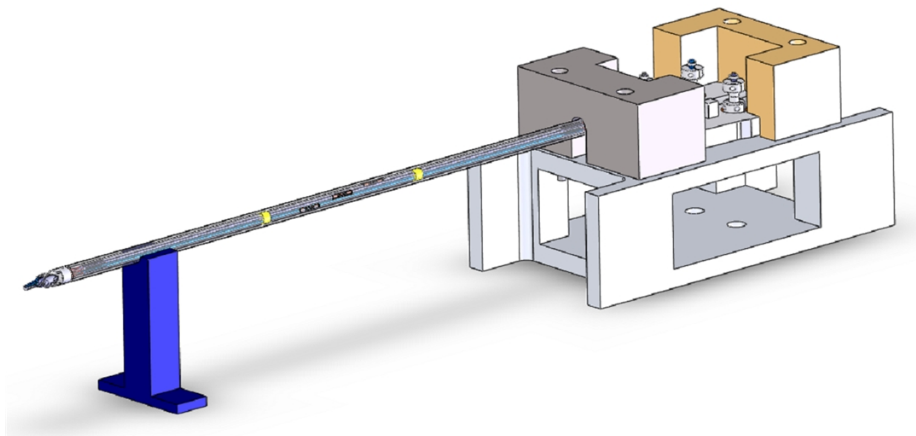

Figure 2.6: CAD model of the calibration jig.

0 to 500 g. The slopes of the signal to weight ratio were then used to compute the applied forces at the tips of the instruments.

Tactile Sensing Instrument

The tactile sensor instrument (TSI) used in this project is a two-dimensional array (15×4) of pressure sensing capacitive elements in a thin and continuous sheet (Pressure Profile Systems Inc. [87]) developed for measuring the tactile pressure distribution between objects in direct physical contact. Each element is 2 mm $\times$2 mm and the total size of the sensor is 30 mm $\times$8 mm. This sensor is attached to a probe, with the shaft length of 385 mm and the shaft diameter of 10 mm, that is suitable for use in MIS. In order to address biocompatibility issues, a disposable laparoscopic latex sleeve is placed over the sensor and shaft of the probe. The tactile data obtained from the sensor contains information about the magnitudes, distributions and locations of forces.

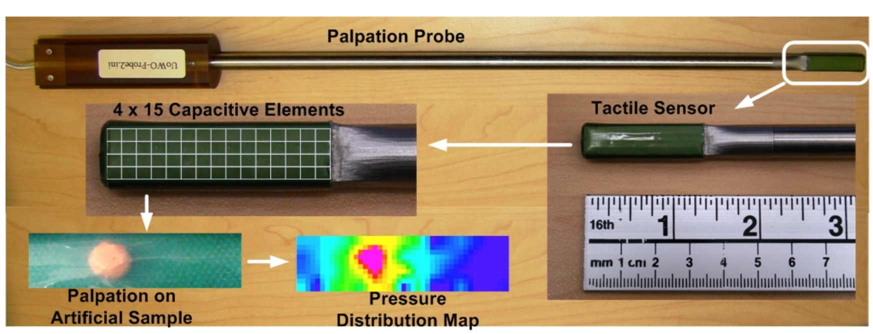

Figure 2.7: The tactile sensing instrument with a tactile sensor at the tip.

Figure 2.8: ATI Gamma force sensor with the capability of force/torque measurement in 6-DOF.

2.2.3 Wrist-Mounted Force Sensor

The sensor which is used to measure the interaction force between the laparoscopic instrument and the tissue is an ATI Gamma six-DOF force sensor [88] (Fig. 2.8) which is mounted between the wrist of the Mitsubishi PA10-7C robot and the laparoscopic instrument. Using an external force sensor needs a special calibration routine to get an accurate measurements of the the interaction between the tool and the tissue [72]. There are several sources of the error which may affect the force readings. They can be classified into four groups;

1. Initial offset of the force sensor: the origin of this offset is because of the strain gauges used in the internal structure of the force sensor. This offset depends on the preload applied to the force sensor, the torques and forces exerted on the force sensor when screwing the tool on the force sensor and the experimental conditions such as temperature.

2. Gravity effect on the laparoscopic tool and the plate of the sensor that the tool is attached to; this external force varies depending on the geometry and the weight of the end effector and has different effect for different orientation of the robot. Since different instruments can be used based on the MIS application, a compensation approach should be developed to estimate the location of the center of mass of the instrument and the total weight of the tool before running the experiment.

3. Dynamic effect of the tool due to the motion of the robot: this is also a consequence of the geometry and the weight of the instrument attached to the robot end effector which can be significant if the acceleration and velocity of the robot are high. However, for MIS applications with low velocity and acceleration of the laparoscopic tool, the dynamic effect of the instrument is negligible and can be ignored.

4. Friction effect and the interaction of the laparoscopic tool with the trocar at the entry point is the other part which needs to be compensated for in order to determine the interaction force at the tip of the instrument with the tissue.

Considering all of the aforementioned sources of error affecting tip wrench measurements, the force and torque measured by the wrist-mounted force sensor in the sensor frame can be written as

$$\begin{bmatrix} \boldsymbol{f}_{mes} \\ \boldsymbol{\tau}_{mes} \end{bmatrix} = \begin{bmatrix} \boldsymbol{f}_{tip} + \boldsymbol{f}_{friction} + \boldsymbol{f}_{nc} \\ \boldsymbol{\tau}_{tip} + \boldsymbol{\tau}_{friction} + \boldsymbol{\tau}_{nc} \end{bmatrix} \tag{2.1}$$

where $\boldsymbol{f}_{nc}$ and $\boldsymbol{\tau}_{nc}$ are the non-contact force and torque created by the initial offset of the force sensor and the gravity effect of the laparoscopic tool (- As stated, the dynamics effect of the tool can be ignored because of its low velocity and acceleration in MIS applications) which can be expressed as

$$\begin{bmatrix} \boldsymbol{f}_{nc} \\ \boldsymbol{\tau}_{nc} \end{bmatrix} = \begin{bmatrix} \boldsymbol{f}_{off} + {}^{o}_{s}\boldsymbol{R}\, m\boldsymbol{g} \\ \boldsymbol{\tau}_{off} + \boldsymbol{l}_{cm} \times {}^{o}_{s}\boldsymbol{R}\, m\boldsymbol{g} \end{bmatrix} \tag{2.2}$$

in which $\boldsymbol{f}_{off}$ and $\boldsymbol{\tau}_{off}$ are the force and torque measurement offset and m denotes the total mass of the end effector tool and the mounting plate in the force sensor to which the tool is attached. $\boldsymbol{g}$ is also the gravity vector with the norm of 9.81 N/ms^{-2}. Here, $\boldsymbol{l}_{cm}$ represents the location of the center of mass for the laparoscopic instrument attached to the force sensor, and ${}^{o}_{s}\boldsymbol{R}$ is the rotation matrix from the robot base to the sensor frame which can be obtained from the kinematics of the Mitsubishi PA10-7C robot.

To accurately measure the interaction force at the tip of the instrument, at the first step, we identify the initial offset of the force sensor, the weight of the instrument and the position of its center of mass. Since the sensor measurement offset varies based on the preload applied to the force sensor and the mass a parameters are not precisely known in advance for the laparoscopic instrument attached to the force sensor, parameter identification routine was used before running the experiments. For this purpose, the robot was commanded to move randomly in free space within its workspace, while holding the laparoscopic instrument attached to the ATI force sensor. The force sensor data and robot rotation matrix were recorded for different configurations to be used later for parameter identification. The least-squares method was used to estimate the unknown parameters. For the ith robot configuration, the force is measured during the identification procedure as

$$\begin{bmatrix} \boldsymbol{f}_{free,i} \\ \boldsymbol{\tau}_{free,i} \end{bmatrix} = \begin{bmatrix} \boldsymbol{f}_{off} + {}^{o}_{s}\boldsymbol{R}_i \, m\boldsymbol{g} \\ \boldsymbol{\tau}_{off} + \boldsymbol{l}_{cm} \times {}^{o}_{s}\boldsymbol{R}_i \, m\boldsymbol{g} \end{bmatrix} \tag{2.3}$$

$\boldsymbol{f}_{free,i}$ and $\boldsymbol{\tau}_{free,i}$ can be rewritten in matrix form as

$$\boldsymbol{f}_{free,i} = \begin{bmatrix} \boldsymbol{I}_3 & {}^{o}_{s}\boldsymbol{R}_i \end{bmatrix} \begin{bmatrix} \boldsymbol{f}_{off} \\ m\boldsymbol{g} \end{bmatrix} \tag{2.4}$$

and

$$\boldsymbol{\tau}_{free,i} = \begin{bmatrix} \boldsymbol{I}_3 & -[{}^{o}_{s}\boldsymbol{R}_i \, m\boldsymbol{g}]_\times \end{bmatrix} \begin{bmatrix} \boldsymbol{\tau}_{off} \\ \boldsymbol{l}_{cm} \end{bmatrix} \tag{2.5}$$

where

$$[\boldsymbol{a}]_\times = \begin{bmatrix} 0 & -a_3 & a_2 \\ a_3 & 0 & -a_1 \\ -a_2 & a_1 & 0 \end{bmatrix} \tag{2.6}$$

We first estimate the mass parameter of the tool as it is used in the torque equation (Eq. 2.5) as well. By collecting force data for n points in the robot workspace, we would have

$$\boldsymbol{F}_{free} = P \begin{bmatrix} \boldsymbol{f}_{off} \\ m\boldsymbol{g} \end{bmatrix} \tag{2.7}$$

where

$$\boldsymbol{F}_{free} = \begin{bmatrix} \boldsymbol{f}_{free,1} \\ \vdots \\ \boldsymbol{f}_{free,n} \end{bmatrix}, \; P = \begin{bmatrix} \boldsymbol{I}_3 & {}^{o}_{s}\boldsymbol{R}_1 \\ \vdots & \vdots \\ \boldsymbol{I}_3 & {}^{o}_{s}\boldsymbol{R}_n \end{bmatrix} \tag{2.8}$$

Then, the force measurement offset and the weight of the tool can be estimated by the least-squares method as

$$\begin{bmatrix} \boldsymbol{f}_{off} \\ m\boldsymbol{g} \end{bmatrix} = (\boldsymbol{P}^T\boldsymbol{P})^{-1}\boldsymbol{P}^T \, \boldsymbol{F}_{free} \tag{2.9}$$

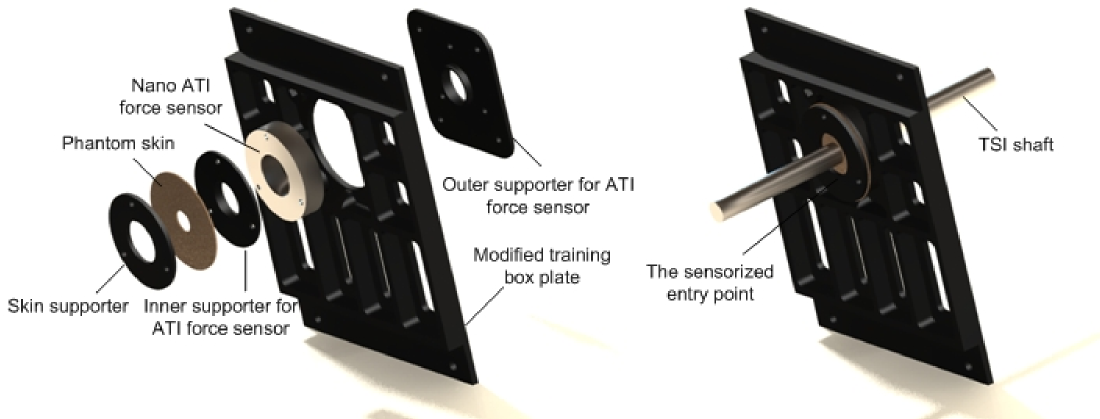

Figure 2.9: Modified entry point integrated with an ATI Nano force sensor to measure friction and interaction between the laparoscopic tool and the artificial skin.

By estimating the weight of the laparoscopic tool, we would be able to estimate the torque measurement offset $\boldsymbol{\tau}_{off}$ and the position of the center of mass $\boldsymbol{l}_{cm}$. With the same procedure used for the force, the following equation can be obtained for the torque measurements:

$$\boldsymbol{T}_{free} = Q \begin{bmatrix} \boldsymbol{\tau}_{off} \\ \boldsymbol{l}_{cm} \end{bmatrix} \tag{2.10}$$

where

$$\boldsymbol{T}_{free} = \begin{bmatrix} \boldsymbol{\tau}_{free,1} \\ \vdots \\ \boldsymbol{\tau}_{free,n} \end{bmatrix}, \; Q = \begin{bmatrix} \boldsymbol{I}_3 & -[{}^{o}_{s}\boldsymbol{R}_1 \, m\boldsymbol{g}]_{\times} \\ \vdots & \vdots \\ \boldsymbol{I}_3 & -[{}^{o}_{s}\boldsymbol{R}_n \, m\boldsymbol{g}]_{\times} \end{bmatrix} \tag{2.11}$$

Then, we have

$$\begin{bmatrix} \boldsymbol{\tau}_{off} \\ \boldsymbol{l}_{cm} \end{bmatrix} = (\boldsymbol{Q}^T\boldsymbol{Q})^{-1}\boldsymbol{Q}^T \, \boldsymbol{T}_{free} \tag{2.12}$$

For the experiment running inside the MIS training box, the interaction between the laparoscopic instrument and the entry point needs to be canceled out as well. In order to measure this external force at the entry point, we have embedded an ATI Nano force sensor at the entry point as shown in Fig. 2.9. By mapping the measured forces and torques at the wrist of the Mitsubishi PA10-7C robot and also at the entry point of the MIS training box into the world frame of the Mitsubishi PA10-7C robot,

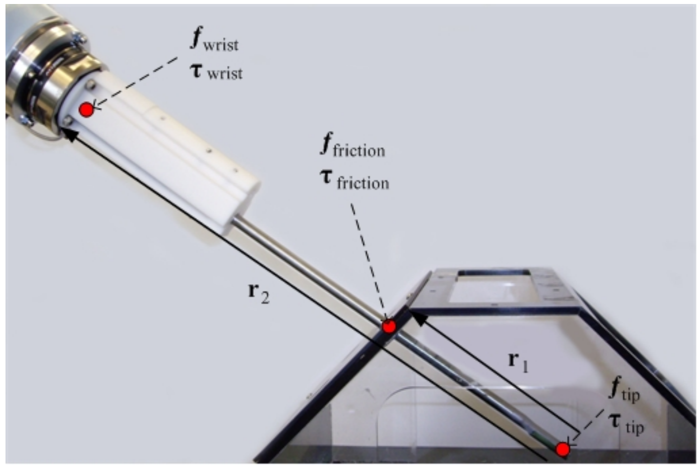

Figure 2.10: The wrench applied on the TSI while doing palpation in the MIS training box.

the force applied to the tip of the tool in the world frame can be measured as

$$\boldsymbol{f}_{tip} = -(\boldsymbol{f}_{wrist} + \boldsymbol{f}_{friction}) \tag{2.13}$$

and the torque applied by tissue to the tool in the world frame is also given by

$$\boldsymbol{\tau}_{tip} = -(\boldsymbol{\tau}_{wrist} + \boldsymbol{\tau}_{friction} + \boldsymbol{r}_1 \times \boldsymbol{f}_{friction} + \boldsymbol{r}_2 \times \boldsymbol{f}_{wrist}) \tag{2.14}$$

where $\boldsymbol{r}_1$ and $\boldsymbol{r}_2$ are shown in Fig. 2.10. The norms of $\boldsymbol{r}_1$ and $\boldsymbol{r}_2$ are equal to the length of insertion and the length of the tool, respectively. Here, $\boldsymbol{f}_{wrist}$ and $\boldsymbol{\tau}_{wrist}$ denote the force and torque measured by the Gamma force sensor after compensating the weight effect of the tool and the initial offset of the force sensor.

Here, we present the results of calibration procedure for the tactile sensing instrument. To identify the parameters of the non-contact force model, the Mitsubishi PA10-7C robot with the TSI attached was commanded to move to sixty points in the robot workspace with no contact with its environment (free-motion). Then the force data were collected to form $\boldsymbol{F}_{free}$. The estimation results obtained from Eqs. (2.9) and (2.12) are

$$\boldsymbol{f}_{off} = \begin{bmatrix} 3.11 \\ 3.52 \\ -0.71 \end{bmatrix} \text{N}\ ,\ \boldsymbol{\tau}_{off} = \begin{bmatrix} 0.16 \\ -0.24 \\ -0.03 \end{bmatrix} \text{Nm} \tag{2.15}$$

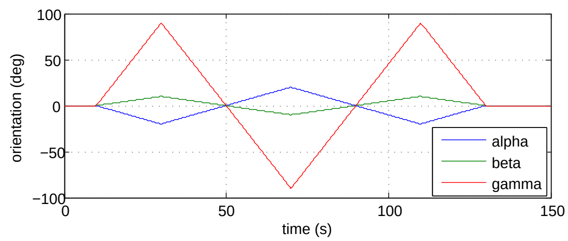

Figure 2.11: Desired orientation trajectory used for the model validation.

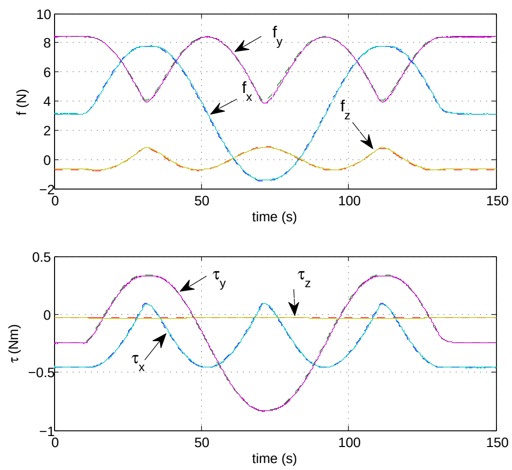

(a) Force tracking: the force sensor readings vs. the model output

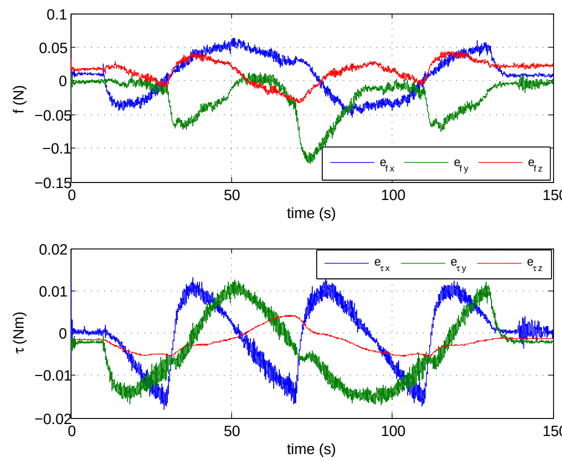

(b) The modeling error

Figure 2.12: Non-contact wrench model validation for the given desired orientation trajectory.

and

$$m = 0.498 \text{ Kg} \ , \ \boldsymbol{l}_{cm} = \begin{bmatrix} 0 \\ 0 \\ 12.64 \end{bmatrix} \text{cm} \tag{2.16}$$

To verify the accuracy of the model using the estimated parameters, the Mitsubishi PA10-7C robot was commanded to follow a reference trajectory in free space different from that used for parameter identification. Since the gravity effect of the tool varies based on the orientation of the tool, the desired trajectory was defined in orientation space (Fig. 2.11). Force/torque measurements of the Gamma force sensor and the

Table 2.2: The modeling errors of the non-contact wrench

Modeling Error	f_x	f_y	f_z	τ_x	τ_y	τ_z
Average (N/Nmm)	0.01	-0.03	0.01	-0.5	-3.7	-2.1
Min (N/Nmm)	-0.05	-0.12	-0.03	-18.1	-16.9	-5.5
Max (N/Nmm)	0.06	0.01	0.04	13.1	12.6	4.2

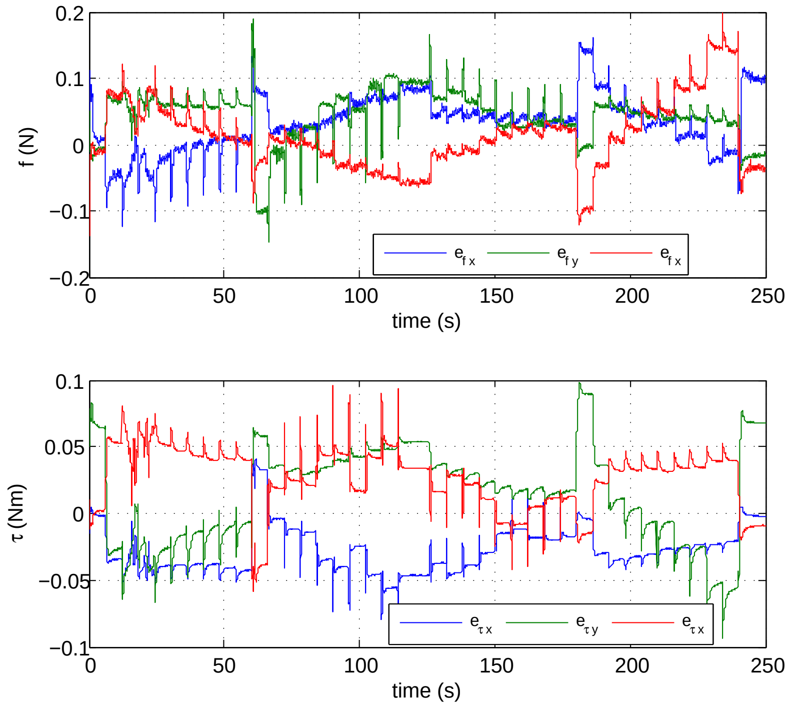

Figure 2.13: Wrench measurement error in free motion inside the MIS training box

non-contact wrench obtained from the model (Eq. (2.2)) are shown in Fig. 2.12(a). The modeling errors are also shown in Fig. 2.12(b). The average, minimum and maximum error for the model are summarized in Table 2.2.

The next step was to explore the accuracy of the measurements at the tip of the palpator when palpation is done inside the training box and the interaction between the tool and the entry point affects the force readings. Here, the Mitsubishi PA10-7C robot was commanded to follow a linear trajectory containing 40 points across the workspace inside the MIS training box while the palpator was not in contact with its environment (covering a volume of size of $6cm \times 8cm \times 3cm$, for x, y and z, respectively). Fig. 2.13 shows the force and the torque at the tip calculated by the model in (2.13) and (2.14). Since the palpator did not touch the environment during the experiment, the model should ideally give zero value for the forces and torques;

Table 2.3: The error of the model developed to measure the wrench at the tip of the TSI

Modeling Error	f_x	f_y	f_z	τ_x	τ_y	τ_z
Average (N/Nmm)	0.03	0.04	0.01	-27	14	26
Min (N/Nmm)	-0.12	-0.14	-0.13	-85	-94	-58
Max (N/Nmm)	0.16	0.18	0.19	40	97	95

however due to modeling errors for the non-contact wrench and some error introduced by the contact between the palpator and the artificial skin (non-rigid contact), it has a larger error as summarized in Table 2.3.

2.2.4 Force-Sensor Integrated Test-Bed

One of the main advantages of using haptics in RAMIS is to prevent too much force being applied to tissue or blood vessels during surgical interventions. This excessive forces might damage tissue or puncture blood vessels. To explore the effectiveness of haptics in RAMIS, the forces applied to tissue need to be measured. Fig. 2.14 shows an experimental setup developed for conducting a series of RAMIS tasks including pushing on tissue (mimicking a palpation motion), pulling on an elastic band (as in trying to lift a flap of tissue) and pull on suture (as in tightening a knot). To measure the forces applied on the setup, an ATI Gamma force/torque sensor was mounted below the setup and rigidly fixed to the experimental table. This sensor can measure forces and torques in 6-DOF. However, the force applied on the tissue is the norm of forces applied to the force sensor.

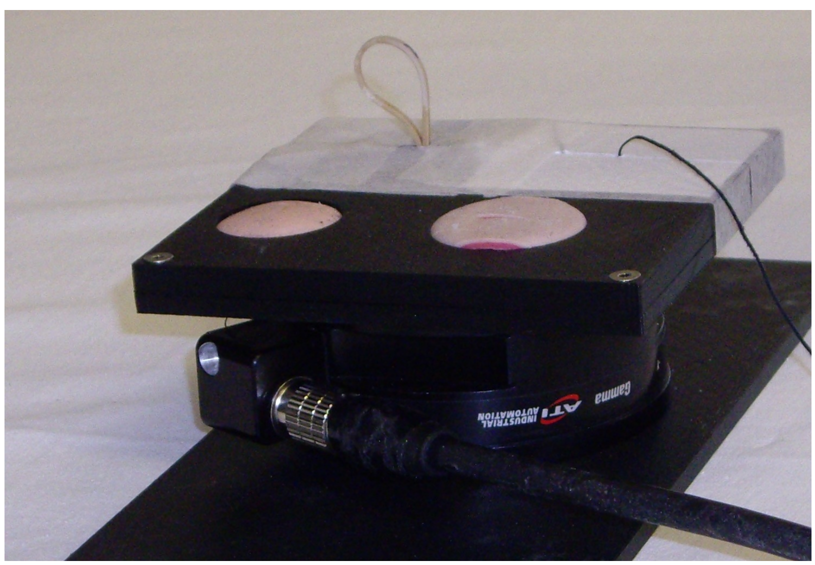

Figure 2.14: Experimental test-bed for measurement of applied forces.

2.3 Controller Implementation

The implementation of the controllers was done on two Windows-based systems. Fig. 2.15 shows the schematic diagram of the controller implemented on our dual arm master-slave teleoperation system. Two computers have been assigned to control the robot manipulators in the setup: one for the master and one for the slave. Both haptic wands interface with the same computer through two Hardware-in-Loop (HIL) cards [84]. The Mitsubishi PA10-7C robots also communicate with the host computer (the slave computer) by sending data packets via the ARCNET protocol. All control algorithms developed for the Haptic Wands and Mitsubishi PA10-7C robots

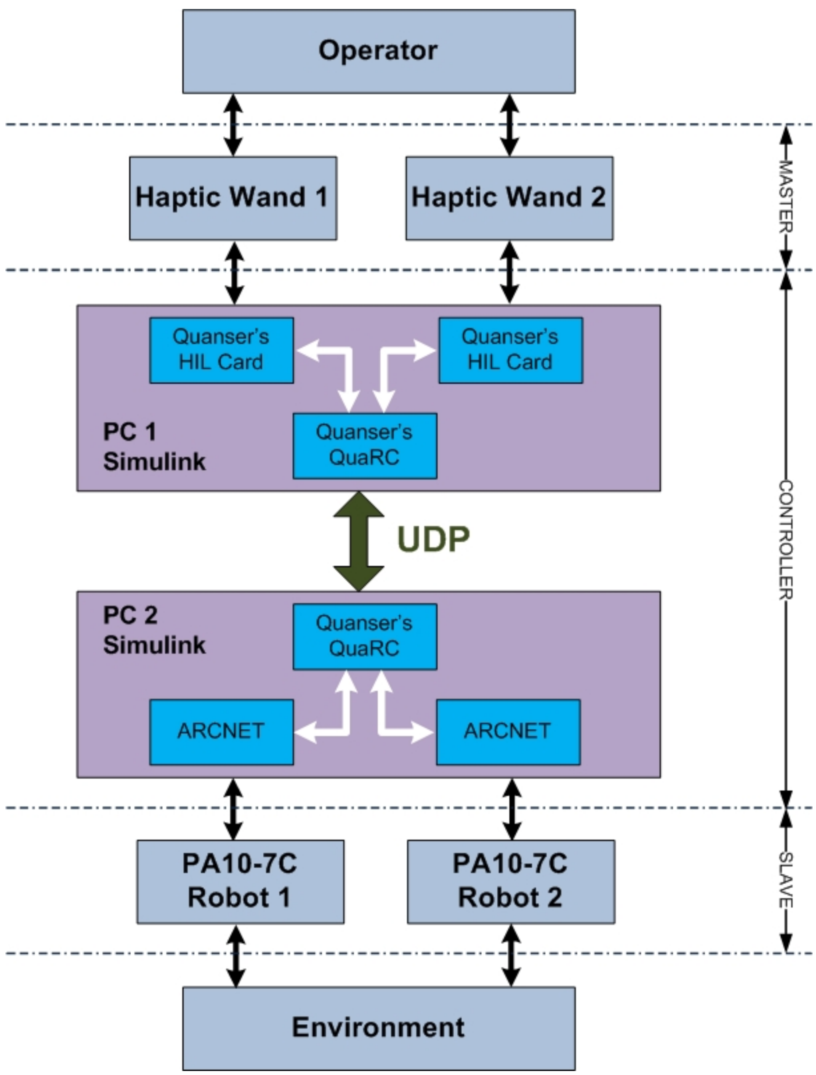

Figure 2.15: The schematic diagram of the controller for the dual arm teleoperation system.

were implemented in Quanser's Real-Time Control (QuaRC) software [84]. QuaRC is an open-architecture software which can be integrated with Simulink/MATLAB® for rapid controls prototyping and hardware-in-the-loop testing. This software automatically generates real-time code directly from Simulink designed controllers that can run on many target processors and operating systems combinations. An Application Programming Interface (API) is provided with QuaRC. Using Quanser's HIL card and this API, any of the QuaRC-supported data acquisition cards can be read and written externally for use in different applications.

To implement bilateral teleoperation system, the master and slave computers communicate with each other through the User Datagram Protocol (UDP) at a sampling frequency of 1 kHz. All of the controllers designed for the master and slave manipulators were also implemented at the same sampling frequency.

Several control design algorithms have been developed for the master and the slave manipulators which will be described in the next Chapter. Fig. 2.16 and 2.17 show the pictures of the models, interface blocks and the controller developed in MATLAB®/Simulink for the Haptic Wands (the master) and the Mitsubishi PA10-7C robots, respectively.

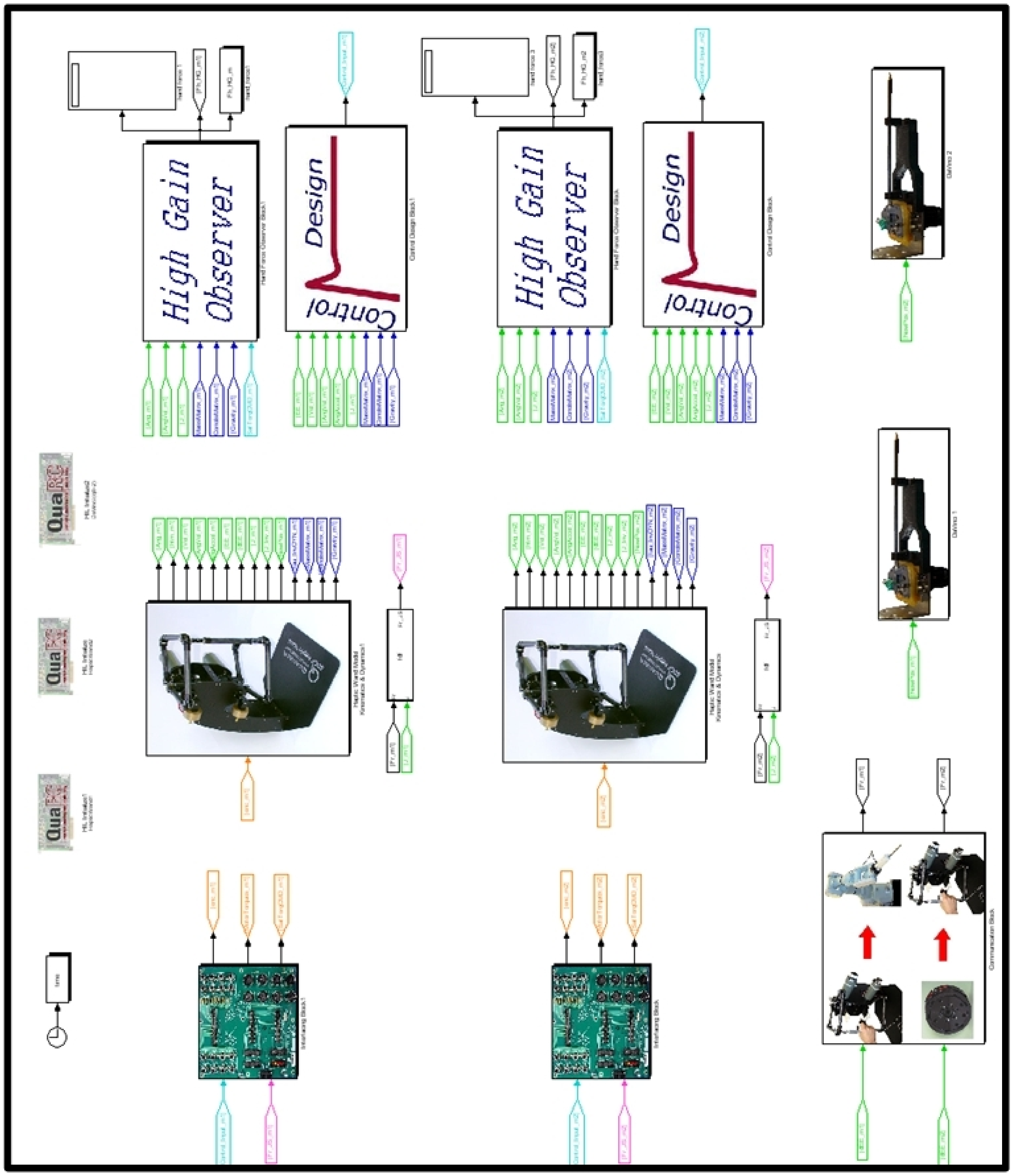

Figure 2.16: A diagram of the models, interface blocks and the controller developed for the Haptic Wands (the master) in MATLAB®/Simulink.

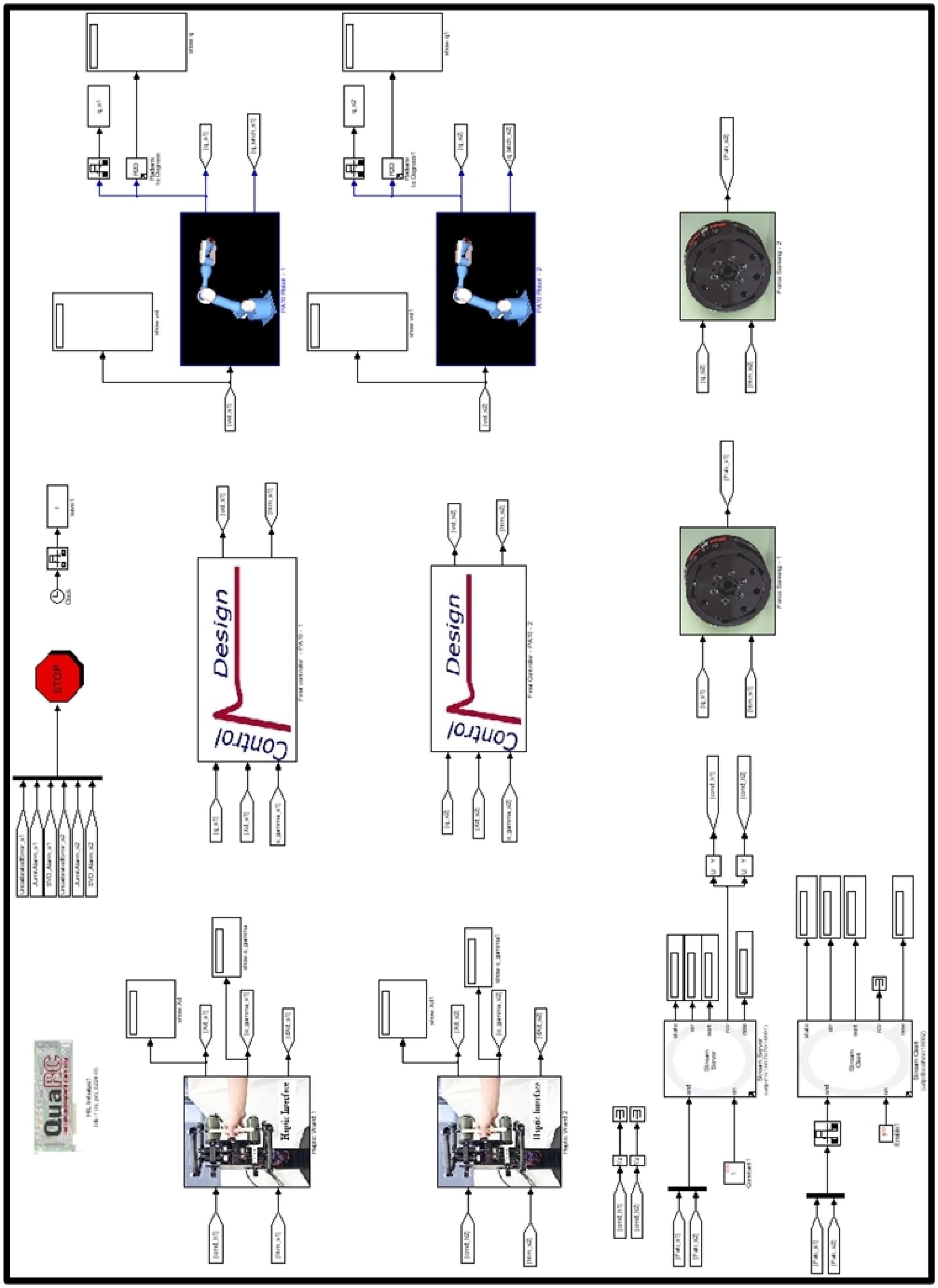

Figure 2.17: A diagram of the models, interface blocks and the controller developed for the Mitsubishi PA10-7C manipulators (the slave) in MATLAB®/Simulink.

Chapter 3

Controller Design for Teleoperation

To implement control algorithms effectively on the dual-arm teleoperation system described in the previous chapter, both the master and slave robot manipulators need to be modeled as accurately as possible. Since the kinematics and dynamics of the Mitsubishi PA10-7C robot have already been developed in the literature [89],[90], we will only focus on the modeling problem for the de Vinci instrument and the Haptic Wand in this chapter. After describing the models for the manipulators, the control methods which have been used for the dual-arm teleoperation system will be explained in detail.

3.1 Manipulator Modeling

3.1.1 The Sensorized da Vinci Instrument

Kinematic Model of the Sensorized da Vinci Instrument

Figure 3.1 shows different components of the wrist of a da Vinci needle driver instrument used for MIS. The tip contains four main components: the base of the wrist, the proximal part of the gripper which can rotate along the ϕ axis, and the two distal parts (numbered 1 and 2), which can independently rotate along the ψ_i axis and constitute the jaw of the gripper. This figure also presents the kinematic model of this instrument. This model can be used to determine the equations describing the behavior of the tool, as a function of the rotation about ψ_i $(i = 1, 2)$ and ϕ.

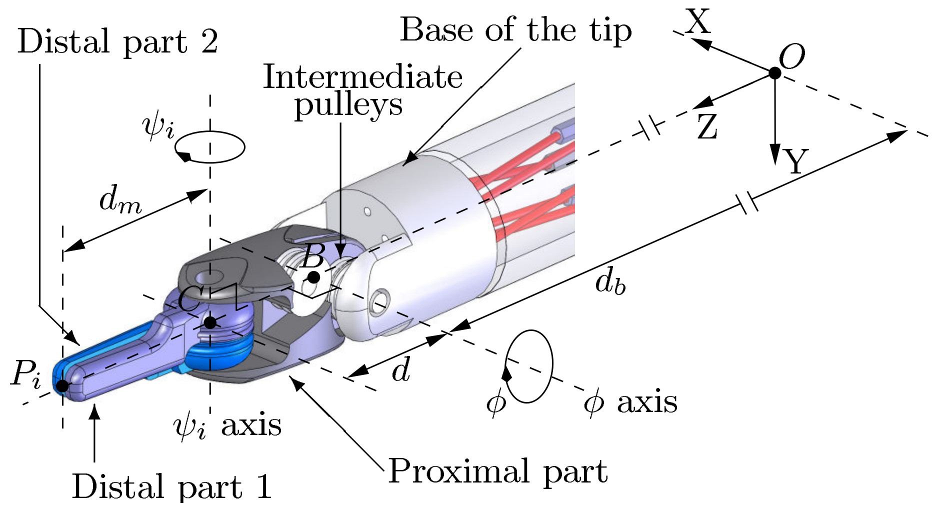

Figure 3.1: Kinematic modeling of a cable-driven endoscopic tool.

Looking at Fig. 3.1, the position vector of the tool is defined by the following equation

$$\mathbf{p}_i = \begin{bmatrix} x_i \\ y_i \\ z_i \end{bmatrix} = \begin{bmatrix} d_m \sin\psi_i \\ -(d + d_m \cos\psi_i)\sin\phi \\ (d + d_m \cos\psi_i)\cos\phi + d_b \end{bmatrix}, \tag{3.1}$$

where d_m represents the length of the segment $\overline{CP_i}$, d is the length of $\overline{BC}$, and d_b is the length of $\overline{OB}$.

Since the tool is controlled from the opposite end using electrical motors, the relationship between $\{\psi_1,\psi_2,\phi\}$ and joint angles $\{\Theta_1,\Theta_2,\Theta_\phi\}$ is as follows:

$$\begin{bmatrix} \psi_1 \\ \psi_2 \\ \phi \end{bmatrix} = \mathbf{S} \begin{bmatrix} \Theta_1 \\ \Theta_2 \\ \Theta_\phi \end{bmatrix} = \begin{bmatrix} \frac{r_{\Theta_1}}{r_{\psi_1}} & 0 & \frac{-r_{1p} r_{\Theta_\phi}}{r_\phi r_{\psi_1}} \\ 0 & \frac{r_{\Theta_2}}{r_{\psi_2}} & \frac{-r_{2p} r_{\Theta_\phi}}{r_\phi r_{\psi_2}} \\ 0 & 0 & \frac{-r_{\Theta_\phi}}{r_\phi} \end{bmatrix} \begin{bmatrix} \Theta_1 \\ \Theta_2 \\ \Theta_\phi \end{bmatrix}, \tag{3.2}$$

where, as shown in Fig. 3.1, r_{Θ_i} is the radius of the pulleys associated with Θ_i, r_{ψ_i} is the radius of the pulleys associated with ψ_i, r_{ip} is the radius of the intermediate pulleys mounted on the axis ϕ of the gripper, r_{Θ_ϕ} is the radius of the pulley associated with Θ_ϕ, and r_ϕ is the radius of the pulley associated with ϕ. Since the motion of the gripper will be controlled by specifying their respective rotation displacements through the master handle, the inverse of the matrix S in Eq. (3.2) should be used to solve for $\{\Theta_1,\Theta_2,\Theta_\phi\}$.

Experimental Verification of the Kinematic Model

To verify the accuracy of the previous kinematic model, the displacements of a chosen point on the two parts of the gripper's jaw needed to be measured, while controlling the joint angles $\{\Theta_1,\Theta_2,\Theta_\phi\}$ with electrical drives. The Aurora® electromagnetic tracking system from Northern Digital Inc. [91] was used to track the position of the tool tip. The trajectory obtained was compared to the one calculated from the kinematic model presented in the previous section.

The resulting errors were determined as the root mean square error (RMSE). The RMSE corresponding to the sensor attached on the distal part 2 of the endoscopic tool was 0.848 mm for x position, 0.902 mm for y position, and 1.269 mm for z position. Moreover, RMSE associated with the sensor mounted on the distal part 1 were respectively 0.740 mm, 1.338 mm, and 1.551 mm. These results are obtained for a chosen trajectory denoting displacements of sensors inside a rectangular polyhedron of dimensions 200 × 200 × 100 mm, after increasing the length of the gripper's jaw from 10 mm to 100 mm (variable d_m in Fig. 3.1). Hence, these results ensure that the potential error at the tip would be much less than 1 mm, and that the expression for the matrix $\mathbf{S}$ is suitable to map the transformation between joint angles $\{\Theta_1,\Theta_2,\Theta_\phi\}$ and rotation displacements at the tip $\{\psi_1,\psi_2,\phi\}$.

3.1.2 The 7-DOF Haptic Wand

Forward Kinematics of the 7-DOF Haptic Wand

The Forward Kinematics Problem (FKP) for the haptic device is to determine the Cartesian pose of the handle and the gripper $\{x,y,z,\phi,\theta,\psi_l,\psi_u\}$ when knowing the joint angles $\{\theta_1,\ldots,\theta_8\}$. Here, the indices l and u are related to the lower and the upper part of the Haptic Wand, respectively. We start with Fig. 3.2 which represents the wire frame model of the architecture of the 7-DOF Haptic Wand. In this figure, the point O represents the origin of the world frame $\mathcal{A}$ of the mechanism, while the point P represents the origin of the moving frame $\mathcal{B}_i$ attached to the handle and each part of the gripper. This point is also defined as the reference point of the end effector of the 7-DOF Haptic Wand. The axes of the passive revolute joints pass through the points $\{A,B,C,E,F,G\}$ and the axes of the two actuated revolute joints pass through the point P. The axes of the actuated universal joints pass through the points $\{F_a,F_b,F_e,F_f\}$, the axes of the passive universal joints pass through the points

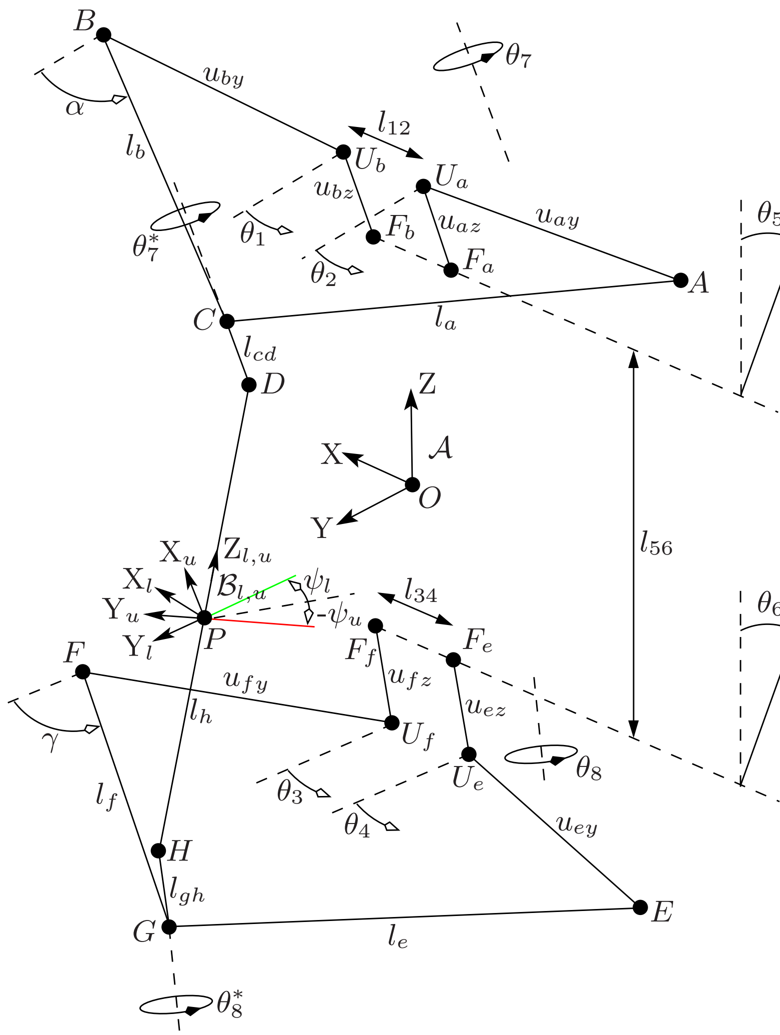

Figure 3.2: Wire frame model of the 7-DOF Haptic Wand.

$\{D,H\}$, and the points $\{U_a,U_b,U_e,U_f\}$ are the reference points of the rigid joints. Finally, this mechanism has the property that the points $\{U_a,A,C,B,U_b\}$ are always coplanar. The same is the case for the set of the points $\{U_e,E,G,F,U_f\}$. Moreover, we note that $\theta_7^* = R_7\theta_7$ and $\theta_8^* = R_8\theta_8$, where R_7 and R_8 are constant known ratio generated by the cable-driven differential transmission related to these joint angles.

To solve the FKP for this mechanism, it is first required to know the positions of the points D and H, i.e., the vectors $\mathbf{d} \equiv \overline{OD}$ and $\mathbf{h} \equiv \overline{OH}$, respectively. In order to determine the vector $\mathbf{d}$, we define vectors belonging to the upper part of the device. The vector $\mathbf{f}_b$ points from O to F_b, $\mathbf{u}_{bz} \equiv \overline{F_bU_b}$, $\mathbf{u}_{by} \equiv \overline{U_bB}$, $\mathbf{l}_b \equiv \overline{BC}$, and $\mathbf{l}_{cd} \equiv \overline{CD}$ (or if we chose the other side, $\mathbf{f}_a$ points from O to F_a, $\mathbf{u}_{az} \equiv \overline{F_aU_a}$, $\mathbf{u}_{ay} \equiv \overline{U_aA}$, and

$\mathbf{l}_a \equiv \overline{AC}$). By defining $\mathbf{b} \equiv \overline{OB}$, the vector $\mathbf{d}$ can be obtained as:

$$\begin{aligned}
\mathbf{b} &= \mathbf{f}_b + \mathbf{u}_{bz} + \mathbf{u}_{by} \\
&= \begin{bmatrix} \frac{l_{12}}{2} \\ 0 \\ \frac{l_{56}}{2} \end{bmatrix} + \begin{bmatrix} 0 \\ -u_{bz}\mathrm{s}\theta_5 \\ u_{bz}\mathrm{c}\theta_5 \end{bmatrix} + \begin{bmatrix} -u_{by}\mathrm{s}\theta_1 \\ u_{by}\mathrm{c}\theta_1\mathrm{c}\theta_5 \\ u_{by}\mathrm{c}\theta_1\mathrm{s}\theta_5 \end{bmatrix}, \\
\mathbf{d} &= \mathbf{b} + \mathbf{l}_b + \mathbf{l}_{cd} = \mathbf{b} + \begin{bmatrix} -l_b\mathrm{s}\alpha \\ l_b\mathrm{c}\alpha\mathrm{c}\theta_5 \\ l_b\mathrm{c}\alpha\mathrm{s}\theta_5 \end{bmatrix} + \begin{bmatrix} 0 \\ l_{cd}\mathrm{s}\theta_5 \\ -l_{cd}\mathrm{c}\theta_5 \end{bmatrix},
\end{aligned} \tag{3.3}$$

where s $\equiv$ sin and c $\equiv$ cos. The angle α, which is a function of θ_1 and θ_2 (the angle between the plane YZ and the segment $\overline{BC}$), is unknown. It can be calculated using the fact that the points $\{U_a,A,C,B,U_b\}$ are coplanar and a closed-loop vector is easily defined. By defining $\mathbf{f} \equiv \overline{OF}$, the vector $\mathbf{h}$ can be also achieved as:

$$\begin{aligned}
\mathbf{f} &= \mathbf{f}_f + \mathbf{u}_{fz} + \mathbf{u}_{fy} \\
&= \begin{bmatrix} \frac{l_{34}}{2} \\ 0 \\ \frac{-l_{56}}{2} \end{bmatrix} + \begin{bmatrix} 0 \\ u_{fz}\mathrm{s}\theta_6 \\ -u_{fz}\mathrm{c}\theta_6 \end{bmatrix} + \begin{bmatrix} -u_{fy}\mathrm{s}\theta_3 \\ u_{fy}\mathrm{c}\theta_3\mathrm{c}\theta_6 \\ u_{fy}\mathrm{c}\theta_3\mathrm{s}\theta_6 \end{bmatrix}, \\
\mathbf{h} &= \mathbf{f} + \mathbf{l}_f + \mathbf{l}_{gh} = \mathbf{f} + \begin{bmatrix} -l_f\mathrm{s}\gamma \\ l_f\mathrm{c}\gamma\mathrm{c}\theta_6 \\ l_f\mathrm{c}\gamma\mathrm{s}\theta_6 \end{bmatrix} + \begin{bmatrix} 0 \\ -l_{gh}\mathrm{s}\theta_6 \\ l_{gh}\mathrm{c}\theta_6 \end{bmatrix},
\end{aligned} \tag{3.4}$$

where γ, which is the angle between the plane YZ and the segment $\overline{FG}$ and is a function of θ_3 and θ_4, is calculated by using a similar method as for α, but on the lower part of the mechanism. Also, the definitions of the required vectors are as follows: $\mathbf{f}_f$ points from O to F_f, $\mathbf{u}_{fz} \equiv \overline{F_fU_f}$, $\mathbf{u}_{fy} \equiv \overline{U_fF}$, $\mathbf{l}_f \equiv \overline{FG}$, and $\mathbf{l}_{gh} \equiv \overline{GH}$ (or if we chose the other side, $\mathbf{f}_e$ points from O to F_e, $\mathbf{u}_{ez} \equiv \overline{F_eU_e}$, $\mathbf{u}_{ey} \equiv \overline{U_eE}$, and $\mathbf{l}_e \equiv \overline{EC}$). Therefore, the position of the point P is

$$\mathbf{p} = \begin{bmatrix} x & y & z \end{bmatrix}^T = \frac{\mathbf{d}+\mathbf{h}}{2}. \tag{3.5}$$

It is noticed that the redundant waist joint cannot be actuated independently. Once $\mathbf{d}$ and $\mathbf{h}$ are know, they must satisfy the constraint $(\mathbf{d}-\mathbf{h})^T(\mathbf{d}-\mathbf{h}) = l_h^2$, where l_h is the length of the segment $\overline{DH}$.

In order to determine the orientation of the end effector, a series of frames are defined

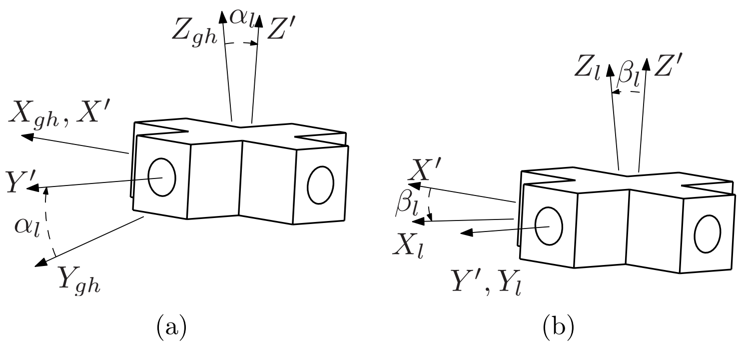

Figure 3.3: Frames attached to the U-joint on the lower part of the 7-DOF Haptic Wand: (a) First rotation α_l between the U-joint cross (frame $\mathcal{O}'$) and the link $\overline{GH}$ (frame $\mathcal{L}_{gh}$) and (b) Second rotation β_l between the first part of the gripper (frame $\mathcal{B}_l$) and the U-joint cross (frame $\mathcal{O}'$).

and attached to the different moving links from the base frame $\mathcal{A}$ to the mobile frame $\mathcal{B}_i$ attached to each of the two parts of the gripper, i.e., $\mathcal{B}_l$ and $\mathcal{B}_u$. Specifically, to obtain the rotation matrix $\mathbf{Q}_l$ corresponding to the transformation $\mathcal{A} \to \mathcal{B}_l$, we start with determining the rotation matrix between $\mathcal{A}$ and the frame $\mathcal{L}_{gh}$ attached to the link $\overline{GH}$ of the lower part of the 7-DOF Haptic Wand. Since the body attached to segment $\overline{GH}$ is always perpendicular to the plane formed by the points $\{U_e, E, G, F, U_f\}$, and hence its orientation in the workspace only depends on the joint angles corresponding to θ_6 and θ_8, we can easily define this rotation matrix as:

$$\mathbf{Q}_{\mathcal{A},\mathcal{L}_{gh}} = \begin{bmatrix} c\theta_8^* & -s\theta_8^* & 0 \\ s\theta_8^* c\theta_6 & c\theta_8^* c\theta_6 & -s\theta_6 \\ s\theta_8^* s\theta_6 & c\theta_8^* s\theta_6 & c\theta_6 \end{bmatrix}. \tag{3.6}$$

Then we know that universal joint only allows two relative rotations along each axis of the cross [92], i.e., in the current case, one related to its input part (link $\overline{GH}$) and one related to its output part (lower link of the handle). Therefore, based on the Fig. 3.3, the internal rotation matrices can be expressed as:

$$\mathbf{Q}_{\mathcal{L}_{gh},\mathcal{O}'} = \begin{bmatrix} 1 & 0 & 0 \\ 0 & c\alpha_l & -s\alpha_l \\ 0 & s\alpha_l & c\alpha_l \end{bmatrix},$$

$$\mathbf{Q}_{\mathcal{O}',\mathcal{B}_l} = \begin{bmatrix} c\beta_l & 0 & s\beta_l \\ 0 & 1 & 0 \\ -s\beta_l & 0 & c\beta_l \end{bmatrix}. \tag{3.7}$$

Finally, $\mathbf{Q}_l$ is given by:

$$\mathbf{Q}_{\mathcal{A},\mathcal{L}_{gh}}\mathbf{Q}_{\mathcal{L}_{gh},\mathcal{O}'}\mathbf{Q}_{\mathcal{O}',\mathcal{B}_l} \equiv \mathbf{Q}_l = \begin{bmatrix} \mathbf{x}_l & \mathbf{y}_l & \mathbf{z}_l \end{bmatrix}, \tag{3.8}$$

where $\mathbf{x}_l$, $\mathbf{y}_l$, and $\mathbf{z}_l$ are the orthonormal vectors attached to $\mathcal{B}_l$ and these vectors are defined as follows:

$$\begin{aligned}
\mathbf{x}_l &= \begin{bmatrix} \mathrm{c}\theta_8^*\mathrm{c}\beta_l - \mathrm{s}\theta_8^*\mathrm{s}\alpha_l\mathrm{s}\beta_l \\ \mathrm{s}\theta_8^*\mathrm{c}\theta_6\mathrm{c}\beta_l + \mathrm{s}\beta_l(\mathrm{c}\theta_8^*\mathrm{c}\theta_6\mathrm{s}\alpha_l + \mathrm{s}\theta_6\mathrm{c}\alpha_l) \\ \mathrm{s}\theta_8^*\mathrm{s}\theta_6\mathrm{c}\beta_l + \mathrm{s}\beta_l(\mathrm{c}\theta_8^*\mathrm{s}\theta_6\mathrm{s}\alpha_l - \mathrm{c}\theta_6\mathrm{c}\alpha_l) \end{bmatrix}, \\
\mathbf{y}_l &= \begin{bmatrix} -\mathrm{s}\theta_8^*\mathrm{c}\alpha_l \\ \mathrm{c}\theta_8^*\mathrm{c}\theta_6\mathrm{c}\alpha_l - \mathrm{s}\theta_6\mathrm{s}\alpha_l \\ \mathrm{c}\theta_8^*\mathrm{s}\theta_6\mathrm{c}\alpha_l + \mathrm{c}\theta_6\mathrm{s}\alpha_l \end{bmatrix}, \\
\mathbf{z}_l &= \begin{bmatrix} \mathrm{c}\theta_8^*\mathrm{s}\beta_l + \mathrm{s}\theta_8^*\mathrm{s}\alpha_l\mathrm{c}\beta_l \\ \mathrm{s}\theta_8^*\mathrm{c}\theta_6\mathrm{s}\beta_l - \mathrm{c}\beta_l(\mathrm{c}\theta_8^*\mathrm{c}\theta_6\mathrm{s}\alpha_l - \mathrm{s}\theta_6\mathrm{c}\alpha_l) \\ \mathrm{s}\theta_8^*\mathrm{s}\theta_6\mathrm{s}\beta_l - \mathrm{c}\beta_l(\mathrm{c}\theta_8^*\mathrm{s}\theta_6\mathrm{s}\alpha_l + \mathrm{c}\theta_6\mathrm{c}\alpha_l) \end{bmatrix}.
\end{aligned} \tag{3.9}$$

Also, since we know the position of the points D and H, the internal angles α_l and β_l can be easily determined (see Fig. 3.3). Indeed, α_l is determined in projecting $\mathbf{z}_l$ on the plane spanned by $\mathbf{y}_{gh}$ and $\mathbf{z}_{gh}$, following with the projection on $\mathbf{z}_{gh}$ ($\mathbf{z}_{gh}$ is equivalent to $\mathbf{l}_{gh}/l_{gh}$), and β_l is simply determined in projecting $\mathbf{z}_l$ on $\mathbf{z}'$. It is noticed that the third vector relation of Eq. (3.9) can be also used to determine α_l and β_l. For the case of $\mathcal{A} \rightarrow \mathcal{B}_u$, a similar method is used to represent the rotation matrix $\mathbf{Q}_u$ of the second part of the gripper $\{\mathbf{x}_u, \mathbf{y}_u, \mathbf{z}_u\}$, but the variables $\{\theta_8^*,\theta_6,\alpha_l,\beta_l\}$ are replaced by $\{\theta_7^*,\theta_5,\alpha_u,\beta_u\}$, which correspond to the upper part of the mechanism, and the value of $\{\alpha_u,\beta_u\}$ can be similarly found as well. Then, by comparing the matrix $\mathbf{Q}_i$ with the rotation matrix $\mathbf{Q}_{\phi\theta\psi_i}$, defined by the ZYX Euler angles method (see Fig. 2.3), the orientation of the handle $\{\phi, \theta\}$ and the rotation displacements of each part of the gripper $\{\psi_l, \psi_u\}$ are determined. It should be noted that both comparisons, i.e., using $\mathbf{Q}_l$ or $\mathbf{Q}_u$, will lead to the same $\{\phi, \theta\}$ values since they directly emerge from the knowledge of the vector $\mathbf{d} - \mathbf{h}$.

Inverse Kinematics (IK) of the 7-DOF Haptic Wand

In the Inverse Kinematics Problem (IKP), the Cartesian pose $\{x,y,z,\phi,\theta,\psi_l,\psi_u\}$ of the 7-DOF Haptic Wand is given and the joint angles $\{\theta_1,\ldots,\theta_8\}$ are the unknowns.

First, since $\mathbf{p}$ and $\mathbf{Q}_{\phi\theta\psi_i}$ are known in this new problem, we simply obtain the vectors $\mathbf{d}$ and $\mathbf{h}$ as follows

$$\mathbf{d} = \mathbf{p} + \mathbf{Q}_{\phi\theta\psi_i}\mathbf{u}, \quad \text{and} \quad \mathbf{h} = \mathbf{p} - \mathbf{Q}_{\phi\theta\psi_i}\mathbf{u}, \quad i = l, u, \tag{3.10}$$

where the vector $\mathbf{u}$ represents the segment $\overline{PD}$—upper half-part of the complete handle $\overline{DH}$—expressed in the moving frame $\mathcal{B}_i$, and it is defined as $\mathbf{u} = [\begin{array}{ccc} 0 & 0 & \frac{l_h}{2} \end{array}]^T$.

The next step is to determine the angles θ_5 and θ_6. Let us start with the former angle and use the projection on the plane YZ of the closed-loop vector belonging to the constraint equation containing the point B. Based on Fig. 3.2, this linkage is defined as follows:

$$\mathbf{f}_b + \mathbf{u}_{bz} + \mathbf{d}_b + \mathbf{l}_{cd} - \mathbf{d} = 0, \tag{3.11}$$

where $\mathbf{d}_b = \mathbf{u}_{by} + \mathbf{l}_b$. Then, in using the projection matrix $\mathbf{P}$, i.e., the matrix projecting a vector on the plane spanned by unit vectors $\mathbf{y}$ and $\mathbf{z}$, it is possible to write Eq. (3.11) as

$$\mathbf{P}(\mathbf{f}_b + \mathbf{u}_{bz} + \mathbf{l}_{cd} - \mathbf{d}) + ||\mathbf{d}_b||_2^{\mathbf{P}} \begin{bmatrix} 0 \\ \text{c}\theta_5 \\ \text{s}\theta_5 \end{bmatrix} = \mathbf{0}_3, \tag{3.12}$$

where $||\mathbf{d}_b||_2^{\mathbf{P}} = \sqrt{||\mathbf{P}(\mathbf{d} - \mathbf{f}_b)||_2^2 - (u_{bz} - l_{cd})^2}$. Since Eq. (3.12) has only components following the axis Y and Z of the base frame $\mathcal{A}$ (does not depend on θ_1 and θ_2), they can be added and formulated as follows:

$$A_5\text{c}\theta_5 + B_5\text{s}\theta_5 + C_5 = 0, \tag{3.13}$$

where $A_5 = ||\mathbf{d}_b||_2^{\mathbf{P}} - (u_{bz} - l_{cd})$, $B_5 = l_{cd} - u_{bz} - ||\mathbf{d}_b||_2^{\mathbf{P}}$, and $C_5 = (l_h/2)\text{c}\theta\text{s}\phi - y - ((l_{56}/2) - (l_h/2)\text{c}\theta\text{c}\phi - z)$. Finally, θ_5 is given by

$$\theta_5 = 2\,\text{atan}\left(\frac{-B_5 \pm \sqrt{B_5^2 - (C_5^2 - A_5^2)}}{C_5 - A_5}\right). \tag{3.14}$$

It should be noted that this quadratic problem allows two solutions for θ_5 and we choose the minimum value in comparing their absolute values. Also, a similar method is followed to determine θ_6, but the constraint equation containing the point F is used, which is defined as follows:

$$\mathbf{f}_f + \mathbf{u}_{fz} + \mathbf{d}_f + \mathbf{l}_{gh} - \mathbf{h} = 0, \tag{3.15}$$

where $\mathbf{d}_f = \mathbf{u}_{fy} + \mathbf{l}_f$. The next step is to determine θ_1, and $\mathbf{d}_b$, $\mathbf{u}_{by}$, and $\mathbf{l}_b$ are used to reach this goal since those vectors are always coplanar. Then, these constraint closed-loop vectors may be squared and written as follows

$$\mathbf{d}_b^T\mathbf{d}_b - 2\mathbf{d}_b^T\mathbf{u}_{by} + \mathbf{u}_{by}^T\mathbf{u}_{by} = \mathbf{l}_b^T\mathbf{l}_b = l_b^2, \tag{3.16}$$

and this equation can be written as

$$A_1\text{c}\theta_1 + B_1\text{s}\theta_1 + C_1 = 0, \tag{3.17}$$

where $A_1 = -2\mathbf{d}_b^T(\mathbf{e}_2\text{c}\theta_5 + \mathbf{e}_3\text{s}\theta_5)u_{by}$, $B_1 = 2\mathbf{d}_b^T\mathbf{e}_1u_{by}$, $C_1 = ||\mathbf{d}_b||_2^2 + u_{by}^2 - l_b^2$, with $\mathbf{e}_1 = [\ 1 \ \ 0 \ \ 0\ ]^T$, $\mathbf{e}_2 = [\ 0 \ \ 1 \ \ 0\ ]^T$, and $\mathbf{e}_3 = [\ 0 \ \ 0 \ \ 1\ ]^T$. It is noticed that $\mathbf{d}_b$ is known since θ_5 is determined by Eq. (3.14). Finally, θ_1 is given by

$$\theta_1 = 2\text{atan}(\frac{-B_1 \pm \sqrt{B_1^2 - (C_1^2 - A_1^2)}}{C_1 - A_1}). \tag{3.18}$$

Here again, there are two possible solutions for θ_1. Similar methods are used to determine θ_2, θ_3, and θ_4. Finally, θ_7 and θ_8 are readily determined in a similar manner as in the FKP. In the case of determining θ_8, we use the fact that we can express the matrix $\mathbf{Q}_{\mathcal{A},\mathcal{L}_{gh}}$ in two different ways. The first approach is as in Eq. (3.6), where at this step, the only unknown is θ_8^*, and the second one is in expressing this matrix as a function of the Cartesian angular positions $\{\phi, \theta, \psi_l\}$ and the internal angles of the lower universal joint $\{\alpha_l, \beta_l\}$ as follows:

$$\mathbf{Q}^*_{\mathcal{A},\mathcal{L}_{gh}} \equiv \mathbf{Q}_{\phi\theta\psi_l}\mathbf{Q}^T_{\mathcal{O}',\mathcal{B}_l}\mathbf{Q}^T_{\mathcal{L}_{gh},\mathcal{O}'}. \tag{3.19}$$

Finally, comparing $\mathbf{Q}^*_{\mathcal{A},\mathcal{L}_{gh}}$ with $\mathbf{Q}_{\mathcal{A},\mathcal{L}_{gh}}$ allows us to determine the value of θ_8:

$$\theta_8 = \frac{\text{atan2}(-\mathbf{Q}^*_{\mathcal{A},\mathcal{L}_{gh}}(1,2), \mathbf{Q}^*_{\mathcal{A},\mathcal{L}_{gh}}(1,1))}{R_8}. \tag{3.20}$$

A similar method is used to determine the value of θ_7.

Now, the IKP and FKP are completely defined for the 7-DOF Haptic Wand. Hence, the next step is to determine the Jacobian matrix of this device to suitably provide force feedback to the user's hand while he/she is controlling the motion of the handle in Cartesian space.

Jacobian of the 7-DOF Haptic Wand

It should be noted that the mechanism is a redundant one—eight electrical motors are used to fully constrain only 7 DOFs. Hence, the following system of velocity equations can be obtained:

$$\dot{\boldsymbol{\theta}} = \mathbf{W}\mathbf{t}, \tag{3.21}$$

where $\mathbf{t} = \left[\dot{x}, \dot{y}, \dot{z}, \dot{\phi}, \dot{\theta}, \dot{\psi}_l, \dot{\psi}_u\right]$ and $\dot{\boldsymbol{\theta}} = \left[\dot{\theta}_1, \ldots, \dot{\theta}_8\right]$. The Jacobian matrix, $\boldsymbol{J}$, is given by the pseudo-inverse of the matrix $\mathbf{W}$. Eq. (3.21) can be also written as

$$\mathbf{I}\mathbf{t} = \mathbf{K}\dot{\boldsymbol{\theta}}, \tag{3.22}$$

where the matrices $\mathbf{I}$ and $\mathbf{K}$ are determined using the eight velocity constraint equations of the mechanism. In fact, we symbolically determined time derivatives of the constraint equations used while defining the IK model of the mechanism for variables $\{\theta_1, \ldots, \theta_6\}$, i.e., Eq. (3.17) for θ_1 and similar equations for θ_2, θ_3, and θ_4, and Eq. (3.14) for θ_5 and a similar equation for θ_6, as the six first velocity constraint equations, and the two more necessary velocity constraint equations are given using the following relation:

$$\boldsymbol{\omega}_i = \mathrm{vect}(\boldsymbol{\Omega}_i^*) = \frac{1}{2}\begin{bmatrix} \boldsymbol{\Omega}^*_{i_{3,2}} - \boldsymbol{\Omega}^*_{i_{2,3}} \\ \boldsymbol{\Omega}^*_{i_{1,3}} - \boldsymbol{\Omega}^*_{i_{3,1}} \\ \boldsymbol{\Omega}^*_{i_{2,1}} - \boldsymbol{\Omega}^*_{i_{1,2}} \end{bmatrix} = \mathbf{R}\dot{\boldsymbol{\phi}}_i, \quad i = l, u, \tag{3.23}$$

where $\boldsymbol{\omega}_i$ is the Cartesian angular velocities vector attached to each moving part of the gripper, $\boldsymbol{\Omega}_i^* \equiv \dot{\mathbf{Q}}_i\mathbf{Q}_i^T$, $\dot{\mathbf{Q}}_i$ is time derivative of the rotation matrix $\mathbf{Q}_i$, $\dot{\boldsymbol{\phi}}_i$ is the vector containing time derivative of each component of the Euler angles, and $\mathbf{R}$ is defined as follows:

$$\mathbf{R} = \begin{bmatrix} 1 & 0 & s\theta \\ 0 & c\phi & -c\theta s\phi \\ 0 & s\phi & c\theta c\phi \end{bmatrix}. \tag{3.24}$$

To determine the velocity constraint equation related to the joint velocity $\dot{\theta}_8$, the third component of the vector relation $\mathrm{vect}(\dot{\mathbf{Q}}_l\mathbf{Q}_l^T) = \mathbf{R}\dot{\boldsymbol{\phi}}_l$ provides us an equation of $\dot{\psi}_l$ as a function of $\dot{\alpha}_l$ and $\dot{\beta}_l$, whose values can be determined by comparing $\dot{\mathbf{Q}}_l$ with $\dot{\mathbf{Q}}_{\phi\theta\psi_l}$. Using this method leads to a linear velocity constraint equation which only depends on $\mathbf{t}$ and $\dot{\boldsymbol{\theta}}$. Similarly, the velocity constraint equations corresponding to $\dot{\theta}_7$ can be found. Finally, the matrix $\mathbf{I}$ is given by

$$
\mathbf{I} = \begin{bmatrix}
\mathbf{l}_b^T & \mathbf{l}_b^T\mathbf{q}_2 & \mathbf{l}_b^T\mathbf{q}_1 & 0 & 0 \\
\mathbf{l}_a^T & \mathbf{l}_a^T\mathbf{q}_2 & \mathbf{l}_a^T\mathbf{q}_1 & 0 & 0 \\
\mathbf{l}_f^T & -\mathbf{l}_f^T\mathbf{q}_2 & -\mathbf{l}_f^T\mathbf{q}_1 & 0 & 0 \\
\mathbf{l}_e^T & -\mathbf{l}_e^T\mathbf{q}_2 & -\mathbf{l}_e^T\mathbf{q}_1 & 0 & 0 \\
\mathbf{q}_3^T\mathbf{P} & \mathbf{q}_3^T\mathbf{P}\mathbf{q}_2 & \mathbf{q}_3^T\mathbf{P}\mathbf{q}_1 & 0 & 0 \\
-\mathbf{q}_4^T\mathbf{P} & \mathbf{q}_4^T\mathbf{P}\mathbf{q}_2 & \mathbf{q}_4^T\mathbf{P}\mathbf{q}_1 & 0 & 0 \\
\mathbf{0}_3^T & i_1 & i_2 & 0 & i_3 \\
\mathbf{0}_3^T & i_4 & i_5 & i_6 & 0
\end{bmatrix}, \tag{3.25}
$$

where

$$
\begin{aligned}
i_{1,4} =& -\left(k_{\alpha_{u,l}}\mathbf{U}^I_{u,l_{1,3}} + k_{\beta_{u,l}}\mathbf{U}^I_{u,l_{2,3}}\right)\mathrm{c}\phi\mathrm{c}\theta, \\
i_{2,5} =& \left(k_{\alpha_{u,l}}\mathbf{U}^I_{u,l_{1,1}} + k_{\beta_{u,l}}\mathbf{U}^I_{u,l_{2,1}}\right)\mathrm{s}\theta\mathrm{s}\psi_{u,l} \\
&+ \left(k_{\alpha_{u,l}}\mathbf{U}^I_{u,l_{1,2}} + k_{\beta_{u,l}}\mathbf{U}^I_{u,l_{2,2}}\right)\mathrm{c}\theta \\
&+ \left(k_{\alpha_{u,l}}\mathbf{U}^I_{u,l_{1,3}} + k_{\beta_{u,l}}\mathbf{U}^I_{u,l_{2,3}}\right)\mathrm{s}\phi\mathrm{s}\theta, \\
i_{3,6} =& \mathrm{c}\theta - \left(k_{\alpha_{u,l}}\mathbf{U}^I_{u,l_{1,1}} + k_{\beta_{u,l}}\mathbf{U}^I_{u,l_{2,1}}\right)\mathrm{c}\theta\mathrm{c}\psi_{u,l},
\end{aligned} \tag{3.26}
$$

with $\mathbf{U}_u^I$ and $\mathbf{U}_l^I$ defined as Moore-Penrose pseudo-inverse of the matrix $\mathbf{U}_u$ and $\mathbf{U}_l$, respectively, which are defined as follows

$$
\mathbf{U}_u = \begin{bmatrix}
\mathrm{s}\theta^*_{7,8}\mathrm{s}\alpha_u & 0 \\
\mathrm{s}\theta^*_{7,8}\mathrm{c}\alpha_u\mathrm{c}\beta_u & \begin{bmatrix} \mathrm{c}\theta^*_{7,8}\mathrm{c}\beta_u \\ -\mathrm{s}\theta^*_{7,8}\mathrm{s}\alpha_u\mathrm{s}\beta_u \end{bmatrix} \\
\begin{matrix} \mathrm{c}\beta_u(\mathrm{s}\theta_{5,6}\mathrm{s}\alpha_u \\ -\mathrm{c}\theta^*_{7,8}\mathrm{c}\theta_{5,6}\mathrm{c}\alpha_u) \end{matrix} & \begin{bmatrix} \mathrm{s}\theta^*_{7,8}\mathrm{c}\theta_{5,6}\mathrm{c}\beta_u \\ +\mathrm{s}\beta_u(\mathrm{s}\theta_{5,6}\mathrm{c}\alpha_u \\ +\mathrm{c}\theta^*_{7,8}\mathrm{c}\theta_{5,6}\mathrm{s}\alpha_u) \end{bmatrix}
\end{bmatrix}, \tag{3.27}
$$

and

$$
\mathbf{U}_l = \begin{bmatrix}
\mathrm{s}\theta^*_{7,8}\mathrm{s}\alpha_l & 0 \\
\mathrm{s}\theta^*_{7,8}\mathrm{c}\alpha_l\mathrm{c}\beta_l & \begin{bmatrix} \mathrm{c}\theta^*_{7,8}\mathrm{c}\beta_l \\ -\mathrm{s}\theta^*_{7,8}\mathrm{s}\alpha_l\mathrm{s}\beta_l \end{bmatrix} \\
\begin{matrix} \mathrm{c}\beta_l(\mathrm{s}\theta_{5,6}\mathrm{s}\alpha_l \\ -\mathrm{c}\theta^*_{7,8}\mathrm{c}\theta_{5,6}\mathrm{c}\alpha_l) \end{matrix} & \begin{bmatrix} \mathrm{s}\theta^*_{7,8}\mathrm{c}\theta_{5,6}\mathrm{c}\beta_l \\ +\mathrm{s}\beta_l(\mathrm{s}\theta_{5,6}\mathrm{c}\alpha_l \\ +\mathrm{c}\theta^*_{7,8}\mathrm{c}\theta_{5,6}\mathrm{s}\alpha_l) \end{bmatrix}
\end{bmatrix}, \tag{3.28}
$$

and where the indices u and l correspond to the upper and lower part of the Haptic Wand. Moreover,

$$
\begin{aligned}
\mathbf{q}_1 =& \frac{l_h}{2} \begin{bmatrix} \mathrm{c}\theta & \mathrm{s}\theta\mathrm{s}\phi & -\mathrm{s}\theta\mathrm{c}\phi \end{bmatrix}^T, \\
\mathbf{q}_2 =& \frac{l_h}{2} \begin{bmatrix} 0 & -\mathrm{c}\theta\mathrm{c}\phi & -\mathrm{c}\theta\mathrm{s}\phi \end{bmatrix}^T, \\
\mathbf{q}_3 =& \mathbf{P}\left(\mathbf{d}_b - \mathbf{d} + \mathbf{f}_b\right),
\end{aligned}
$$

$$
\begin{aligned}
\mathbf{q}_4 =& -\mathbf{P}\left(\mathbf{d}_f - \mathbf{h} + \mathbf{f}_f\right), \\
k_{\alpha_{u,l}} =& \mathrm{s}\theta^*_{7,8}\left(\mathrm{s}\phi\mathrm{c}\theta_{5,6} - \mathrm{c}\phi\mathrm{s}\theta_{5,6}\right), \\
k_{\beta_{u,l}} =& \mathrm{s}\phi\left(\mathrm{c}\theta^*_{7,8}\mathrm{c}\theta_{5,6}\mathrm{c}\alpha_{u,l} - \mathrm{s}\alpha_{u,l}\mathrm{s}\theta_{5,6}\right) \\
& -\mathrm{c}\phi\left(\mathrm{c}\theta^*_{7,8}\mathrm{s}\theta_{5,6}\mathrm{c}\alpha_{u,l} + \mathrm{s}\alpha_{u,l}\mathrm{c}\theta_{5,6}\right).
\end{aligned}
\tag{3.29}
$$

Then, the matrix $\mathbf{K}$ is expressed as follows:

$$
\mathbf{K} = \begin{bmatrix}
k_1 & 0 & 0 & 0 & k_2 & 0 & 0 & 0 \\
0 & k_3 & 0 & 0 & k_4 & 0 & 0 & 0 \\
0 & 0 & k_5 & 0 & 0 & k_6 & 0 & 0 \\
0 & 0 & 0 & k_7 & 0 & k_8 & 0 & 0 \\
0 & 0 & 0 & 0 & k_9 & 0 & 0 & 0 \\
0 & 0 & 0 & 0 & 0 & k_{10} & 0 & 0 \\
0 & 0 & 0 & 0 & k_{11} & 0 & k_{12} & 0 \\
0 & 0 & 0 & 0 & 0 & k_{13} & 0 & k_{14}
\end{bmatrix},
\tag{3.30}
$$

where the non-zero components are

$$
\begin{aligned}
k_1 =&(\mathbf{l}_b + \mathbf{u}_{by})^T \mathbf{s}_{u_{by},1},\\
k_2 =&\mathbf{l}_b^T(\mathbf{s}_{u_{bz}} + \mathbf{s}_{l_{cd}}) + (\mathbf{l}_b + \mathbf{u}_{by})^T \mathbf{s}_{u_{by},5},\\
k_3 =&(\mathbf{l}_a + \mathbf{u}_{ay})^T \mathbf{s}_{u_{ay},2},\\
k_4 =&\mathbf{l}_a^T(\mathbf{s}_{u_{az}} + \mathbf{s}_{l_{cd}}) + (\mathbf{l}_a + \mathbf{u}_{ay})^T \mathbf{s}_{u_{ay},5},\\
k_5 =&(\mathbf{l}_f + \mathbf{u}_{fy})^T \mathbf{s}_{u_{fy},3},\\
k_6 =&\mathbf{l}_f^T(\mathbf{s}_{u_{fz}} + \mathbf{s}_{l_{gh}}) + (\mathbf{l}_f + \mathbf{u}_{fy})^T \mathbf{s}_{u_{fy},6},\\
k_7 =&(\mathbf{l}_e + \mathbf{u}_{ey})^T \mathbf{s}_{u_{ey},4},\\
k_8 =&\mathbf{l}_e^T(\mathbf{s}_{u_{ez}} + \mathbf{s}_{l_{gh}}) + (\mathbf{l}_e + \mathbf{u}_{ey})^T \mathbf{s}_{u_{ey},6},\\
k_9 =&(\mathbf{P}\mathbf{d}_b)^T(\mathbf{P}(\mathbf{s}_{u_{bz}} + \mathbf{s}_{l_{cd}})),\\
k_{10} =&(\mathbf{P}\mathbf{d}_f)^T(\mathbf{P}(\mathbf{s}_{u_{fz}} + \mathbf{s}_{l_{gh}})),\\
k_{11,13} =&\mathbf{M}_{u,l_{3,1}}(k_{\alpha_{u,l}}\mathbf{U}^I_{u,l_{1,3}} + k_{\beta_{u,l}}\mathbf{U}^I_{u,l_{2,3}}),\\
k_{12} =&R(\mathrm{s}\phi\mathrm{s}\theta_5 + \mathrm{c}\phi\mathrm{c}\theta_5)\\
&+k_{\alpha_u}(\mathbf{U}^I_{u_{1,1}}\mathbf{M}_{u_{1,2}} + \mathbf{U}^I_{u_{1,2}}\mathbf{M}_{u_{2,2}} + \mathbf{U}^I_{u_{1,3}}\mathbf{M}_{u_{3,2}})\\
&+k_{\beta_u}(\mathbf{U}^I_{u_{2,1}}\mathbf{M}_{u_{1,2}} + \mathbf{U}^I_{u_{2,2}}\mathbf{M}_{u_{2,2}} + \mathbf{U}^I_{u_{2,3}}\mathbf{M}_{u_{3,2}}),\\
k_{14} =&R(\mathrm{s}\phi\mathrm{s}\theta_6 + \mathrm{c}\phi\mathrm{c}\theta_6)\\
&+k_{\alpha_l}(\mathbf{U}^I_{l_{1,1}}\mathbf{M}_{l_{1,2}} + \mathbf{U}^I_{l_{1,2}}\mathbf{M}_{l_{2,2}} + \mathbf{U}^I_{l_{1,3}}\mathbf{M}_{l_{3,2}})\\
&+k_{\beta_l}(\mathbf{U}^I_{l_{2,1}}\mathbf{M}_{l_{1,2}} + \mathbf{U}^I_{l_{2,2}}\mathbf{M}_{l_{2,2}} + \mathbf{U}^I_{l_{2,3}}\mathbf{M}_{l_{3,2}}),
\end{aligned}
\tag{3.31}
$$

where $\mathbf{s}_{u_{bz}}$ is the part multiplying the joint velocity $\dot{\theta}_5$ of the vector of time derivative of $\mathbf{u}_{bz}$ and $\mathbf{s}_{u_{by},1}$ is the part multiplying the joint velocity $\dot{\theta}_1$ of the vector of time derivative of $\mathbf{u}_{by}$. The terms, $\mathbf{s}_{u_{ez}}$, $\mathbf{s}_{l_{cd}}$, $\mathbf{s}_{l_{gh}}$, $\mathbf{s}_{u_{az}}$, $\mathbf{s}_{u_{fz}}$, $\mathbf{s}_{u_{ay},2}$, $\mathbf{s}_{u_{by},5}$, $\mathbf{s}_{u_{ay},5}$, $\mathbf{s}_{u_{fy},3}$, $\mathbf{s}_{u_{fy},6}$, $\mathbf{s}_{u_{ey},4}$, and $\mathbf{s}_{u_{ey},6}$ are similarly defined. Finally,

$$
\mathbf{M}_{u,l} = \begin{bmatrix}
0 & -R\mathrm{c}\theta^*_{7,8}\mathrm{c}\alpha_{u,l}\\
0 & \begin{bmatrix}(\mathrm{c}\theta^*_{7,8}\mathrm{s}\alpha_{u,l}\mathrm{c}\beta_{u,l}\\ -\mathrm{s}\theta^*_{7,8}\mathrm{s}\beta_{u,l})R\end{bmatrix}\\
\begin{matrix}-\mathrm{s}\theta^*_{7,8}\mathrm{s}\theta_{5,6}\mathrm{s}\beta_{u,l}\\ -\mathrm{c}\beta_{u,l}(\mathrm{c}\theta_{5,6}\mathrm{c}\alpha_{u,l}\\ -\mathrm{c}\theta^*_{7,8}\mathrm{s}\theta_{5,6}\mathrm{s}\alpha_{u,l})\end{matrix} & \begin{bmatrix}R\mathrm{c}\theta_{5,6}(\mathrm{c}\theta^*_{7,8}\mathrm{s}\beta_{u,l}\\ +\mathrm{s}\theta^*_{7,8}\mathrm{s}\alpha_{u,l}\mathrm{c}\beta_{u,l})\end{bmatrix}
\end{bmatrix}. \tag{3.32}
$$

Then, knowing $\mathbf{I}$ and $\mathbf{K}$, the matrix $\mathbf{W}$ is given by

$$\mathbf{W} = \mathbf{K}^{-1}\mathbf{I}. \tag{3.33}$$

Based on the Eq. (3.33) and the following virtual work relation:

$$\boldsymbol{\tau}^T \delta\boldsymbol{\theta} = \mathbf{f}^T \delta\mathbf{p} + t_\phi \delta\phi + t_\theta \delta\theta + t_{\psi_l} \delta\psi_l + t_{\psi_u} \delta\psi_u, \tag{3.34}$$

where $\boldsymbol{\tau} = [t_{\theta_1}, \ldots, t_{\theta_8}]^T$ are the torques generated by the motors, $\delta\boldsymbol{\theta}$ are small joint angles of the motors, $\mathbf{f} = [f_x, f_y, f_z]^T$ is the vector of forces applied at the reference point P of the end effector, $\delta\mathbf{p}$ are small translation displacements of the point P, $\{t_\phi, t_\theta, t_{\psi_l}, t_{\psi_u}\}$ are torques applied along the axes of the Euler angles defining the orientation of the two parts of the end effector and $\{\delta\phi, \delta\theta, \delta\psi_l, \delta\psi_u\}$ are small joint angles of the end effector, the force-torque mapping can be calculated as

$$\boldsymbol{\tau} = \mathbf{J}^T\mathbf{F} = \mathbf{W}\left(\mathbf{W}^T\mathbf{W}\right)^{-1}\mathbf{F}. \tag{3.35}$$

where $\mathbf{F} = \left[\mathbf{f}^T, t_\phi, t_\theta, t_{\psi_l}, t_{\psi_u}\right]^T$ and $\boldsymbol{J}$ is the Jacobian of the 7-DOF Haptic Wand.

This latter relation is expected since the mechanism is redundantly actuated. In fact, Eq. (3.35) represents only one possible solution, i.e., minimal norm solution, to reproduce a particular combination of forces and moments at the handle. Indeed, there are many solutions for a combination of joint torques, provided by the eight electrical motors, to generate specific forces and moments at the end effector of the 7-DOF Haptic Wand.

7-DOF Haptic Wand Dynamics Model

The general form of the dynamics of the 7-DOF Haptic Wand can be expressed as

$$\boldsymbol{D}(\boldsymbol{\theta})\ddot{\boldsymbol{\theta}} + \boldsymbol{C}(\boldsymbol{\theta}, \dot{\boldsymbol{\theta}})\dot{\boldsymbol{\theta}} + \boldsymbol{G}(\boldsymbol{\theta}) + \boldsymbol{\tau_f} = \boldsymbol{\tau} + \boldsymbol{J}^T\boldsymbol{F}_{\text{ext}}, \tag{3.36}$$

where $\boldsymbol{\theta}$, $\dot{\boldsymbol{\theta}}$, and $\ddot{\boldsymbol{\theta}}$ are the joint angle, velocity, and acceleration of the Wand, and $\boldsymbol{D}(\boldsymbol{\theta})$, $\boldsymbol{C}(\boldsymbol{\theta}, \dot{\boldsymbol{\theta}})$, $\boldsymbol{G}(\boldsymbol{\theta})$, and $\boldsymbol{\tau_f}$ denote the inertia matrix, Coriolis and centrifugal terms, gravity vector, and the vector of friction, respectively. $\boldsymbol{\tau}$ represents the vector of actuator torques for the 7-DOF Haptic Wand and $\boldsymbol{F}_{\text{ext}}$ is the external force applied to the Haptic Wand. Since motors 7 and 8 are decoupled from the rest of the mechanism and just drive the upper and lower parts of the handle respectively, in order to calculate

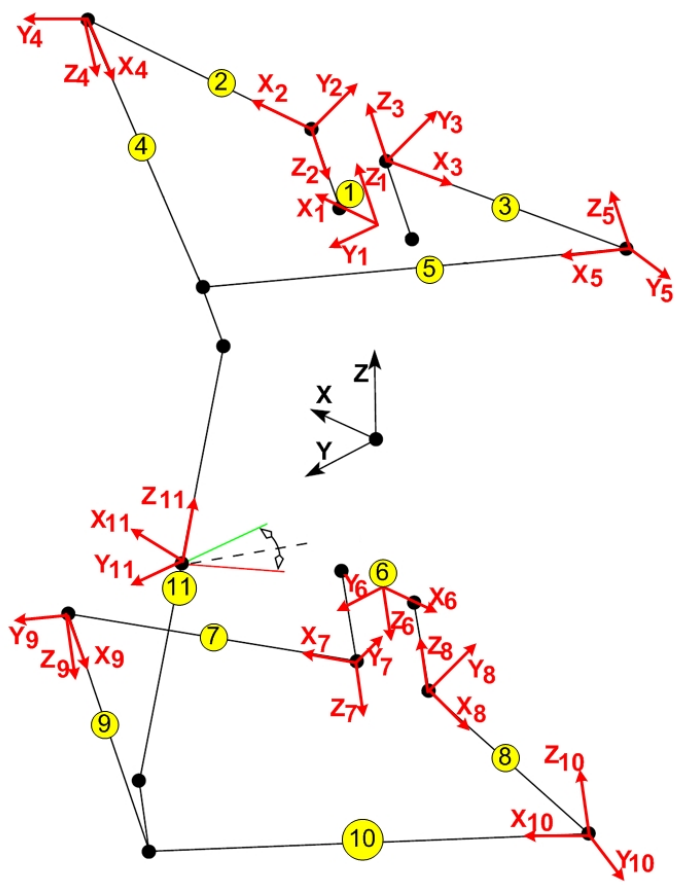

Figure 3.4: Wire-frame model of the 7-DOF Haptic Wand with the local frames

the dynamics of the 7-DOF Haptic Wand, we first derive the dynamics equations using the Lagrangian formulation for the first 6 joint angles, then add the dynamics equations for the handle to get the full dynamics of the mechanism. The friction part is measured experimentally and then added to the equations. For ease of dynamic analysis, the 7-DOF Haptic Wand has been divided into eleven segments with the local frames shown in Fig. 3.4. These segments include the top triple motor assembly, top left drive arm, top right drive arm, top left passive arm, top right passive arm, bottom triple motor assembly, bottom left drive arm, bottom right drive arm, bottom left passive arm and bottom right passive arm, labeled as 1 through 11, respectively. The origin of the local frames for these segments correspond with the joint points defined in wire frame model of the 7-DOF Haptic Wand (Fig. 3.2). The location of the center of mass for segment $\{i\}$ in the local frame, $\boldsymbol{r}^l_{cmi}$, can be expressed in world coordinates, $\boldsymbol{r}^w_{cmi}$, as

$$\boldsymbol{r}^w_{cmi} = \boldsymbol{r}^w_{oi} + \boldsymbol{R}_x(\phi_i)\,\boldsymbol{R}_z(\varphi_i)\,\boldsymbol{r}^l_{cmi}, \tag{3.37}$$

where $\boldsymbol{r}^w_{oi}$ is the position of the origin of the local frame for segment $\{i\}$. The center of mass in the local frame for $i = 1, 6$ is $\boldsymbol{r}^l_{cmi} = \begin{bmatrix} 0 & -l_{cmi} & 0 \end{bmatrix}^T$ and for the other segments is in the form of $\boldsymbol{r}^l_{cmi} = \begin{bmatrix} l_{cmi} & 0 & 0 \end{bmatrix}^T$ except for the handle which is zero because of the coincidence of the origin of the tool frame with the center of mass of the handle. ϕ_i is equal to θ_5 for the upper 5-bar linkage, and equal to θ_6 for the lower 5-bar linkage. The vector $\boldsymbol{\varphi}$ for $i = 1 : 10$ is

$$\begin{aligned} \boldsymbol{\varphi} &= \begin{bmatrix} 0 & \theta_1 & \theta_2 & \psi^*_u & \gamma_u & 0 & \theta_3 & \theta_4 & \psi^*_l & \gamma_l \end{bmatrix} \\ \psi^*_{u,l} &= \pi - (\rho_{u,l} - \sigma_{u,l}), \quad \gamma_{u,l} = \sigma_{u,l} + \rho_{u,l}, \end{aligned} \tag{3.38}$$

and

$$\begin{aligned} \rho_u &= acos(\frac{\overline{AB}}{2l_b}), \sigma_u = atan(\frac{s_1 u_{by} - s_2 u_{ay}}{l_{12} + c_1 u_{by} - c_2 u_{ay}}), \\ \rho_l &= acos(\frac{\overline{EF}}{2l_f}), \sigma_l = atan(\frac{s_3 u_{fy} - s_4 u_{ey}}{l_{34} + c_3 u_{fy} - c_4 u_{ey}}). \end{aligned} \tag{3.39}$$

Since the center of mass for the handle (segment 11) is matched with the origin of the tool frame, $\boldsymbol{r}^w_{cm11}$ would be the origin of the tool frame which is the position of the Haptic Wand end-effector. The rotational velocity, Ω_i for $i = 1, \ldots, 11$, in local frames is given by

$$\begin{aligned} &\boldsymbol{\Omega}_1 = \omega_5 \boldsymbol{i}, \qquad \boldsymbol{\Omega}_6 = \omega_6 \boldsymbol{i}, \qquad \boldsymbol{\Omega}_{11} = \omega_{11} \boldsymbol{k} \\ &\boldsymbol{\Omega}_2 = c_1 \omega_5 \boldsymbol{i} - s_1 \omega_5 \boldsymbol{j} + \omega_1 \boldsymbol{k}, \quad \boldsymbol{\Omega}_3 = c_2 \omega_5 \boldsymbol{i} - s_2 \omega_5 \boldsymbol{j} + \omega_2 \boldsymbol{k}, \\ &\boldsymbol{\Omega}_7 = c_3 \omega_6 \boldsymbol{i} - s_3 \omega_6 \boldsymbol{j} + \omega_3 \boldsymbol{k}, \quad \boldsymbol{\Omega}_8 = c_4 \omega_6 \boldsymbol{i} - s_4 \omega_6 \boldsymbol{j} + \omega_4 \boldsymbol{k}, \\ &\boldsymbol{\Omega}_4 = \boldsymbol{R}_z(-\psi^*_u)\, \boldsymbol{\Omega}_1 + \dot{\psi}^*_u \boldsymbol{k}, \ \boldsymbol{\Omega}_5 = \boldsymbol{R}_z(-\gamma_u)\, \boldsymbol{\Omega}_1 + \dot{\gamma}_u \boldsymbol{k}, \\ &\boldsymbol{\Omega}_9 = \boldsymbol{R}_z(-\psi^*_l)\, \boldsymbol{\Omega}_6 + \dot{\psi}^*_l \boldsymbol{k}, \ \boldsymbol{\Omega}_{10} = \boldsymbol{R}_z(-\gamma_l)\, \boldsymbol{\Omega}_6 + \dot{\gamma}_l \boldsymbol{k}. \end{aligned} \tag{3.40}$$

The translational velocity is also defined for the center of mass vector and is calculated as

$$\boldsymbol{v}_{cmi} = \dot{\boldsymbol{r}}^w_{cmi} \quad \text{for} \quad i = 1, \ldots, 11.$$

The kinetic energy for each segment is given by

$$K_i = \frac{1}{2}(\boldsymbol{v}^T_{cmi} \boldsymbol{M}_i \boldsymbol{v}_{cmi} + \boldsymbol{\Omega}^T_i \boldsymbol{I}_i \boldsymbol{\Omega}_i), \tag{3.41}$$

where $\boldsymbol{M}_i = m_i \boldsymbol{I}_{3\times 3}$ and $\boldsymbol{I}_i$ are respectively the translational and rotational inertia matrices for $i = 1, \ldots, 11$. The potential energy for segment $\{i\}$ is defined as

$$V_i = m_i \, g \, r^z_{cmi}, \tag{3.42}$$

where r^z_{cmi} is the third element of the vector $\boldsymbol{r}^w_{cmi}$ (z-direction). Then the Lagrangian for the 7-DOF Haptic Wand is given by

$$L = \sum_{i=1}^{11} K_i - \sum_{i=1}^{11} V_i. \tag{3.43}$$

Since the 5-bar linkages of the haptic interface are made up of hollow carbon-fiber tubing, they have negligible inertias. Therefore, these parameters are excluded from the calculations and only the inertia of the motor assemblies in the following form, expressed in local frames, are utilized.

$$\begin{bmatrix} I_{ixx} & 0 & 0 \\ 0 & I_{iyy} & 0 \\ 0 & 0 & I_{izz} \end{bmatrix}, \qquad i = 1, 6. \tag{3.44}$$

At the same time, the rotational velocity for the upper and lower motor assemblies is only about the X-axis and as a result, only I_{1xx} and I_{6xx} are involved in the kinetic energy calculation. The measured values for these parameters (in $kg\ m^2$) are $I_{1xx} = 0.0125$ and $I_{6xx} = 0.0125$. The mass parameters are also measured , in kg as $m_{1,6} = 1.1000$, $m_{2,7} = 0.0601$, $m_{3,8} = 0.0601$, $m_{4,9} = 0.0543$, $m_{5,10} = 0.0581$, $m_{11} = 0.0637$. By using a symbolical computation software, e.g., Maple$^{\text{TM}}$ [93], we can calculate the Lagrangian Eq. (3.43) with respect to $\boldsymbol{\theta}$ and write it as

$$L = \frac{1}{2} \dot{\boldsymbol{\theta}}^T \boldsymbol{\mathcal{D}}(\boldsymbol{\theta}) \, \dot{\boldsymbol{\theta}} - V, \tag{3.45}$$

where $\boldsymbol{\mathcal{D}}(\boldsymbol{\theta})$ is the Haptic Wand's mass matrix for the first 6 joint angles and V is the sum of the potential energy for segments 1-11. Eq. (3.45) can also be expressed in the following form:

$$L = \frac{1}{2} \sum_{i,j=1}^{n} \mathcal{D}_{ij} \dot{\theta}_i \dot{\theta}_j - V. \tag{3.46}$$

Then, the dynamics equations can be calculated from

$$\frac{d}{dt}\frac{\partial L}{\partial \dot{\theta}_i} - \frac{\partial L}{\partial \theta_i} = \tau_{m,i}, \quad i = 1, \ldots, 6. \tag{3.47}$$

where $\tau_{m,i}$ is the part of the torque computed from the mathematical model. It can be shown that the equations of motion are given by

$$\sum_{j=1}^{n} \mathcal{D}_{ij}\ddot{\theta}_j + \sum_{j=1}^{n} \mathcal{C}_{ij}\dot{\theta}_j + \mathcal{G}_i = \tau_{m,i}, \quad i = 1, \ldots, 6. \tag{3.48}$$

where

$$\mathcal{C}_{ij} = \frac{1}{2}\sum_{k=1}^{n}(\frac{\partial \mathcal{D}_{ij}}{\partial \theta_k} + \frac{\partial \mathcal{D}_{ik}}{\partial \theta_j} - \frac{\partial \mathcal{D}_{kj}}{\partial \theta_i})\dot{\theta}_k, \quad \mathcal{G}_i = \frac{\partial V}{\partial \theta_i}. \tag{3.49}$$

The dynamics Eq. (3.48) can be rewritten in vector form as

$$\boldsymbol{\mathcal{D}}(\boldsymbol{\theta})\ddot{\boldsymbol{\theta}} + \boldsymbol{\mathcal{C}}(\boldsymbol{\theta}, \dot{\boldsymbol{\theta}})\dot{\boldsymbol{\theta}} + \boldsymbol{\mathcal{G}}(\boldsymbol{\theta}) = \boldsymbol{\tau_m}. \tag{3.50}$$

Eq. (3.50) gives the dynamics equations for the first 6 joint angles. For motors 7 and 8 which drive the upper and lower parts of the handle, we also have

$$J_{eq}\ddot{\theta}_i + \frac{K_m^2}{R_m}\dot{\theta}_i = \tau_{m,i}, \qquad i = 7, 8, \tag{3.51}$$

where K_m and R_m are the motor torque constant and the motor armature resistance, respectively, and J_{eq} is the sum of the moment of inertia of the motor rotor and the moment of inertia of the load (upper or lower handle). The parameters for the motor used for driving the handle in the Haptic Wand are $J_{eq} = 0.000114 kg.m^2$, $R_m = 2.07\Omega$, and $K_m = 0.0525 N.m/A$, respectively. Considering Eqs. (3.50) and (3.51), we can get the following dynamics equation for the 7-DOF Haptic Wand

$$\boldsymbol{D}(\boldsymbol{\theta})\ddot{\boldsymbol{\theta}} + \boldsymbol{C}(\boldsymbol{\theta}, \dot{\boldsymbol{\theta}})\dot{\boldsymbol{\theta}} + \boldsymbol{G}(\boldsymbol{\theta}) = \boldsymbol{\tau_m}, \tag{3.52}$$

where

$$\boldsymbol{D} = \begin{bmatrix} \boldsymbol{\mathcal{D}} & \mathbf{0} \\ \mathbf{0} & J_{eq}\boldsymbol{I} \end{bmatrix}, \; \boldsymbol{C} = \begin{bmatrix} \boldsymbol{\mathcal{C}} & \mathbf{0} \\ \mathbf{0} & \frac{K_m^2}{R_m}\boldsymbol{I} \end{bmatrix}, \; \boldsymbol{G} = \begin{bmatrix} \boldsymbol{\mathcal{G}} \\ \mathbf{0} \end{bmatrix}. \tag{3.53}$$

Now, in order to get the full dynamics of the 7-DOF Haptic Wand, the vector of friction should also be determined and included into the equations.

Friction Analysis

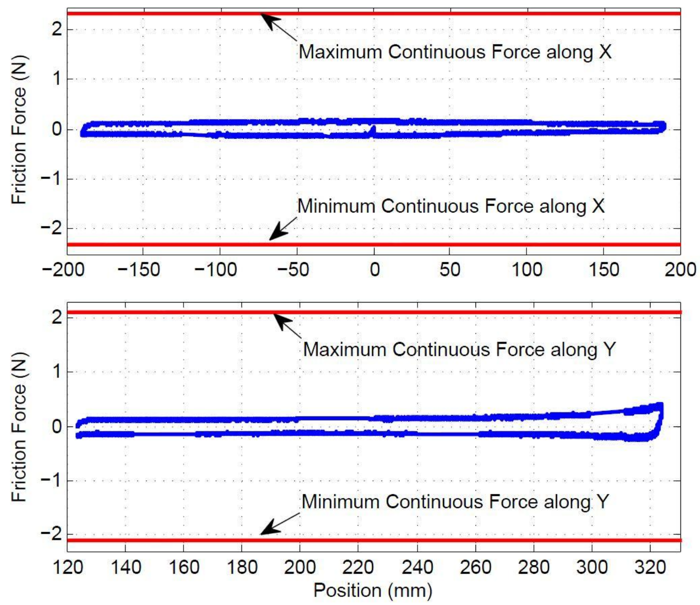

Figure 3.5: Friction measured along x and y axes.

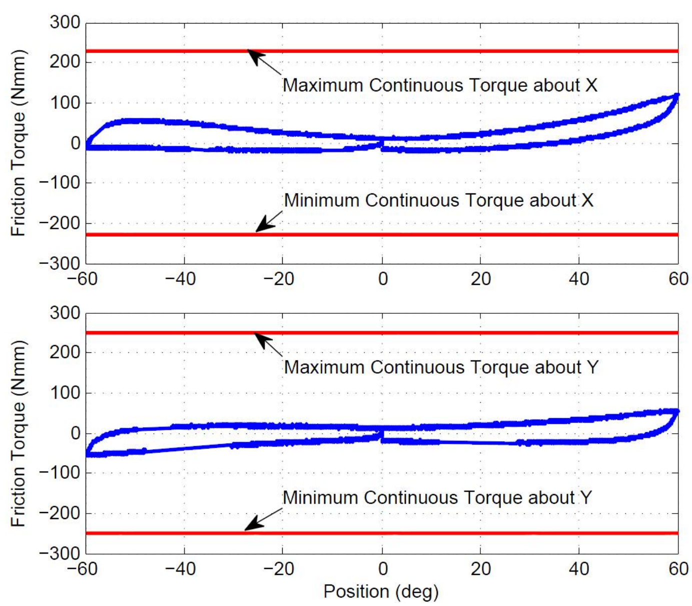

Figure 3.6: Friction measured about x and y axes.

To get fully transparent haptic interaction, the friction present in the Haptic Wand needs to be accurately estimated and fed forward to the actuators. In low-velocity applications like haptics, the dominant friction part is static friction which is defined as the torque required to maintain a very slow velocity over the entire range of motion in the workspace of the haptic device. Because of the coupling in the mechanism,

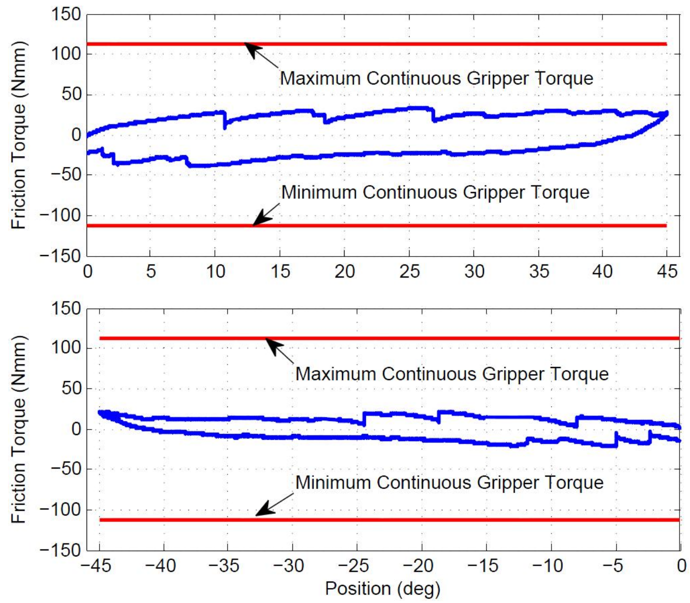

Figure 3.7: Friction measured for the grasping mechanism (ψ_l and ψ_u).

direct friction estimation for each joint is not possible for the Haptic Wand and the static friction should be determined in Cartesian space. To measure the friction torque as accurately as possible, we need to compensate for the effect of gravity during the friction data collecting experiment (the other terms of the dynamics equation have very negligible effect because of the very low velocity of the Haptic Wand for the friction measurement procedure). Using the closed-form dynamics model developed for the 7-DOF Haptic Wand, we can get a very good gravity-balanced haptic device within a wide range of its workspace. However, the experiments showed that the Haptic Wand is not very well balanced along the Z-axis where it is far from its operating point. This is due to the cables connected to the motors which apply some extra force on the mechanism and cannot be easily modeled in the dynamics of the Haptic Wand. For this reason, instead of modeling friction along the Z-axis which cannot be distinguished from the uncertainty present in the system, both friction and the model uncertainty along this direction would be compensated through the controller.

To measure static friction along each DOF, the Haptic Wand was commanded to follow a linear path from the minimum to the maximum point of the workspace in that DOF with a velocity of 0.001 m/s for the position and 0.001 rad/s for the orientation in its workspace. The torques needed to drive the mechanism with the aformentioned velocities mentioned were considered as the static frictions. These torques were calculated by measuring the currents of the motors. Since static friction is dependent on the direction of the velocity, we did the experiments for both positive and negative values. Fig. 3.5-3.7 show the friction force/torque measured over the workspace of the Haptic Wand for both forward and reverse motion. By looking through the results, we can see that the measured friction over the end points of the Haptic Wand workspace in Fig. 3.7 increases which is because of the model uncertainty created by the wires connected to the motors. However, if we consider the range of motion in the middle we can see that the average measured friction is reasonable. Table 3.1 also shows the average, maximum and the percent of maximum measured friction to the peak of the force/torque provided by the Haptic Wand actuators in Cartesian space. The results show that the measured friction lies within 5% of the peak force delivered by the actuators of the Haptic Wand except for the friction in grasping mechanism which is a little bit higher because of the pulley and cable transmission mechanism used for driving the handle.

Then, the measured friction data was collected in a lookup table and fed forward to the actuators of the Haptic Wand. A mathematical model could also be fit on the observed data. Now, we have the full dynamics of the Haptic Wand

$$\boldsymbol{D}(\boldsymbol{\theta})\ddot{\boldsymbol{\theta}} + \boldsymbol{C}(\boldsymbol{\theta},\dot{\boldsymbol{\theta}})\dot{\boldsymbol{\theta}} + \boldsymbol{G}(\boldsymbol{\theta}) + \boldsymbol{\tau_f} = \boldsymbol{\tau} + \boldsymbol{J}^T\boldsymbol{F}_{\text{ext}}, \tag{3.54}$$

We can also rewrite the dynamics aquation in Cartesian space as

$$\boldsymbol{M}_m\ddot{\boldsymbol{X}} + \boldsymbol{B}_m\dot{\boldsymbol{X}} + \boldsymbol{G}_m + \boldsymbol{F}_f = \boldsymbol{u} + \boldsymbol{F}_{\text{ext}} \tag{3.55}$$

where

$$\begin{array}{c} \boldsymbol{M}_m = \boldsymbol{J}^{-T}\boldsymbol{D}\boldsymbol{J}^{-1} \quad , \quad \boldsymbol{B}_m = \boldsymbol{J}^{-T}\boldsymbol{C}\boldsymbol{J}^{-1} - \boldsymbol{D}_x\dot{\boldsymbol{J}}\boldsymbol{J}^{-1} \\ \boldsymbol{G}_m = \boldsymbol{J}^{-T}\boldsymbol{G} \quad , \quad \boldsymbol{u} = \boldsymbol{J}^{-T}\boldsymbol{\tau} \quad , \quad \boldsymbol{F}_f = \boldsymbol{J}^{-T}\boldsymbol{\tau_f} \end{array} \tag{3.56}$$

and $\boldsymbol{J}^{-T}$ is the inverse of the Jacobian transpose for the Haptic Wand.

Table 3.1: The measured friction over the workspace

Friction	x	y	ϕ	θ	ψ_l	ψ_u
Average (N/Nmm)	0.13	0.15	15	23	24	13
Maximum (N/Nmm)	0.18	0.34	25	40	34	20
Max/Peak (%)	2.3	4.8	3.3	4.9	9.2	5.4

7-DOF Haptic Wand Model Verification

To validate the kinematics and dynamics models developed for the 7-DOF Haptic Wand and to determine the effectiveness of the model-based controller for the haptic device, a set of experiments was carried out and presented in this section. First of all, the accuracy of the kinematics model including forward kinematics, inverse kinematics and the Jacobian of the 7-DOF Haptic Wand was explored. Then the performance of feedforward control using the nonlinear dynamics model of the 7-DOF Haptic Wand was compared to that of a simple PD controller for the control problem of the 7-DOF Haptic Wand.

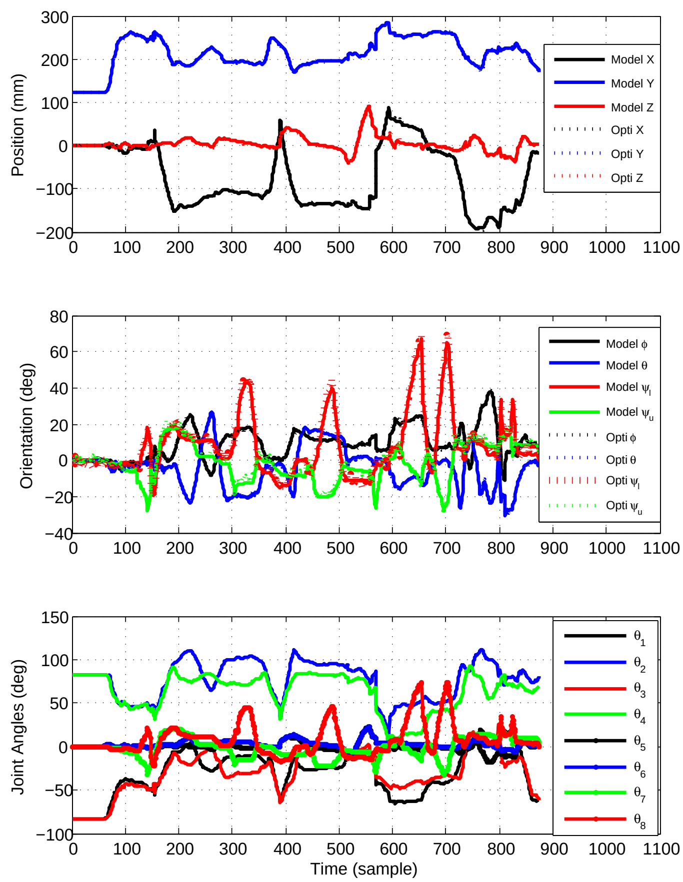

Figure 3.8: Comparison between the Cartesian trajectory obtained from the model with that of the optical tracker.

In order to verify the solution of the FKP for the 7-DOF Haptic Wand, an optical tracking system, i.e., the *Micron Tracker* from Claron Technology Inc. [94], was used. Three markers were mounted on the device, i.e., one fixed on the mechanism's base,

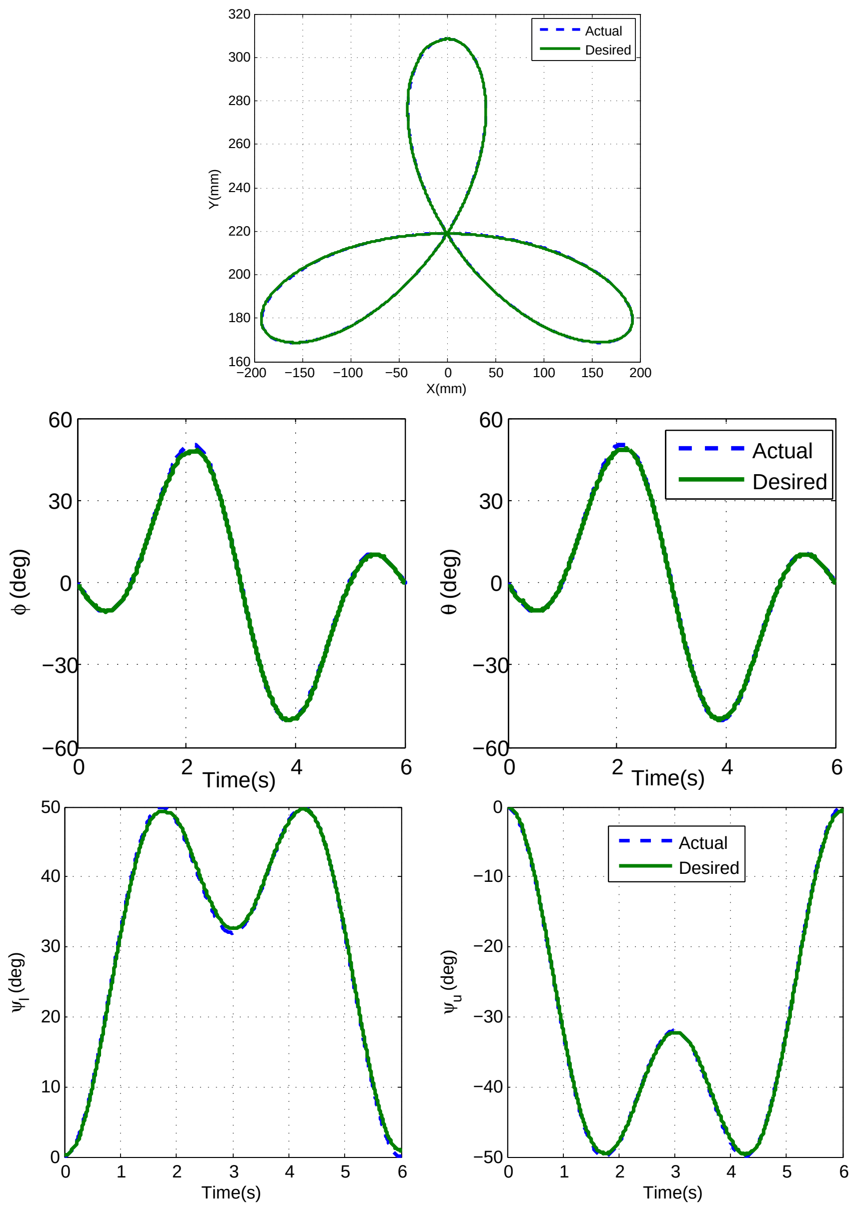

Figure 3.9: End-effector Cartesian position tracking performance using the model-based controller.

and the other two attached to each part of the gripper. In this way, all of the possible motions related to the 7 DOFs can be measured and compared. Then, the handle and the gripper were moved inside the mechanism workspace, given in Table 2.1, in order to cover the entire range of Cartesian motions. Fig. 3.8 shows the results obtained from the optical tracker and those computed by the FKP of the 7-DOF Haptic Wand for both position and orientation. The RMSE for the tracking error in position is 1.400 mm in the X direction, 1.060 mm in the Y direction, and 2.079 mm in the Z direction. Moreover, the RMSE obtained for the error in Euler angle tracking is

0.714^o for ϕ, 0.651^o for θ, 2.141^o for ψ_l, and 2.025^o for ψ_u. In order to verify the validity of the IK model, a numerical simulation using the MATLAB® software was performed. First, a sinusoidal trajectory was defined for each Cartesian DOF of the Haptic Wand. Then, the IK (Inverse Kinematic) model was used to compute the corresponding joint displacements $\{\theta_1, \ldots, \theta_8\}$. These results were then used as the input data for the FK (Forward Kinematic) model in order to compute the corresponding Cartesian displacements. Finally, the resulting Cartesian displacements from the FK model were compared with the initial sinusoidal trajectories to ensure the mutual equivalence between the FK and IK models. The results showed an error less than $|1.5| \times 10^{-10}$ mm and degrees was computed in comparing the Cartesian translationnal displacements $\{X, Y, Z\}$ (in mm) as well as the Cartesian angular displacements $\{\phi, \theta, \psi_l, \psi_u\}$ (in degrees). Using the same reference Cartesian trajectory utilized for IK validation and the corresponding joint angles computed by the IK of the Haptic Wand, the validity of the Jacobian matrix was also explored analytically. For the reference Cartesian velocity given by the vector $\mathbf{t} = \{\dot{x}, \dot{y}, \dot{z}, \dot{\phi}, \dot{\theta}, \dot{\psi}_l, \dot{\psi}_u\}$, time derivative of the vector $\boldsymbol{\theta}$ was analytically computed and compared with time derivatives of the joint angles $\{\theta_1, \ldots, \theta_8\}$ obtained from the IK. The resulting error was always less than $|1.2| \times 10^{-4}$ deg/s along the whole trajectory which confirms the validity of the Jacobian matrix.

The verification of the dynamics model was carried out through an end-effector trajectory tracking problem. In this experiment, a sinusoidal reference Cartesian trajectory was defined around the operating point of the Haptic Wand to almost cover its reachable workspace. In order to reduce the uncertainty in the dynamics model of the 7-DOF Haptic Wand created by the wires connected to the motors, the position of the end effector in the Z direction was kept fixed at zero during the experiment.

Given the reference Cartesian trajectory, the desired joint motions can be computed using the inverse kinematics of the 7-DOF Haptic Wand. The control approach chosen for this experiment was an inverse dynamics method in which the torque control command ($\boldsymbol{\tau}_c$) is in the form

$$\boldsymbol{\tau}_c = \boldsymbol{\tau}_f + \boldsymbol{\tau}_{ff} + \boldsymbol{\tau}_{fb}, \tag{3.57}$$

where $\boldsymbol{\tau}_f$ is the friction torque measured in Section (3.1.2) and fedforward in the controller through a look-up table; $\boldsymbol{\tau}_{ff}$ is the feed-forward vector of control torques corresponding to the desired configuration motions and velocities which are calculated

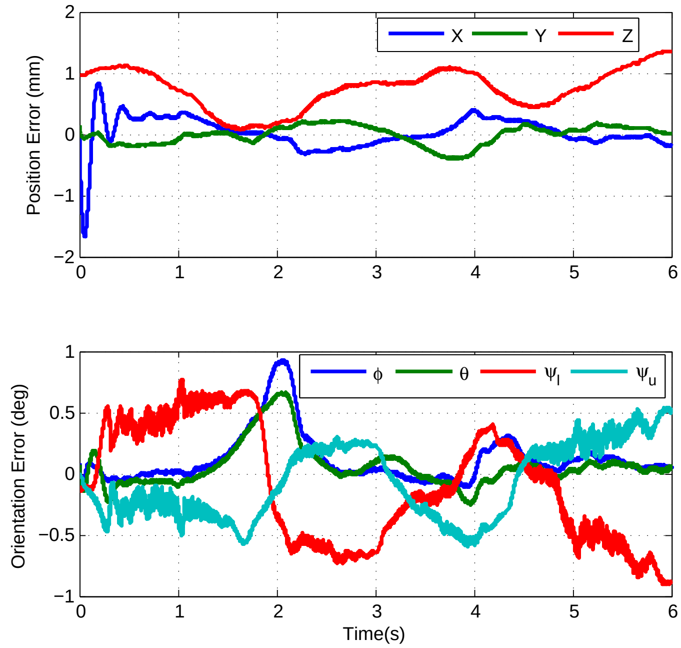

Figure 3.10: Tracking error using the model-based controller.

using the closed-form model developed for the dynamics of the 7-DOF Haptic Wand. This part is used to cancel out the nonlinear behavior of the Haptic Wand and to compensate for the gravity effect of the mechanism. The last term, $\boldsymbol{\tau}_{fb}$, is the feedback control signal computed by a PD controller. The total torque control command is then given by

$$\begin{aligned} \boldsymbol{\tau}_c = \boldsymbol{D}(\boldsymbol{\theta}_d)\ddot{\boldsymbol{\theta}}_d + \boldsymbol{C}(\boldsymbol{\theta}, \dot{\boldsymbol{\theta}}_d)\dot{\boldsymbol{\theta}}_d + \boldsymbol{G}(\boldsymbol{\theta}_d) + \boldsymbol{\tau}_f \\ + \boldsymbol{K}_p(\boldsymbol{\theta}_d - \boldsymbol{\theta}) + \boldsymbol{K}_v(\dot{\boldsymbol{\theta}}_d - \dot{\boldsymbol{\theta}}), \end{aligned} \tag{3.58}$$

where $\boldsymbol{\theta}_d$ is the desired joint trajectory which is computed from the desired end-effector Cartesian trajectory using the inverse kinematics of the 7-DOF Haptic Wand, and $\dot{\boldsymbol{\theta}}_d$ and $\ddot{\boldsymbol{\theta}}_d$ are the vector of the desired joint velocity and joint acceleration. $\boldsymbol{K}_p$ and $\boldsymbol{K}_v$ are the proportional and derivative matrix gains used to produce the PD feedback torque. As can be seen in Eq. (3.58), in order to construct the control law, the joint velocities should be available. But since they are not directly measurable, and also taking derivative of the joint angles results in extremely noisy outcome, a high-gain observer [95] was used to estimate the joint velocities. The end-effector trajectory tracking results are presented in Fig. 3.9. As can be seen, the end effector perfectly followed the desired trajectory in its reachable workspace. The error in position tracking in Cartesian space is also shown in Fig. 3.10. The resulting RMSE

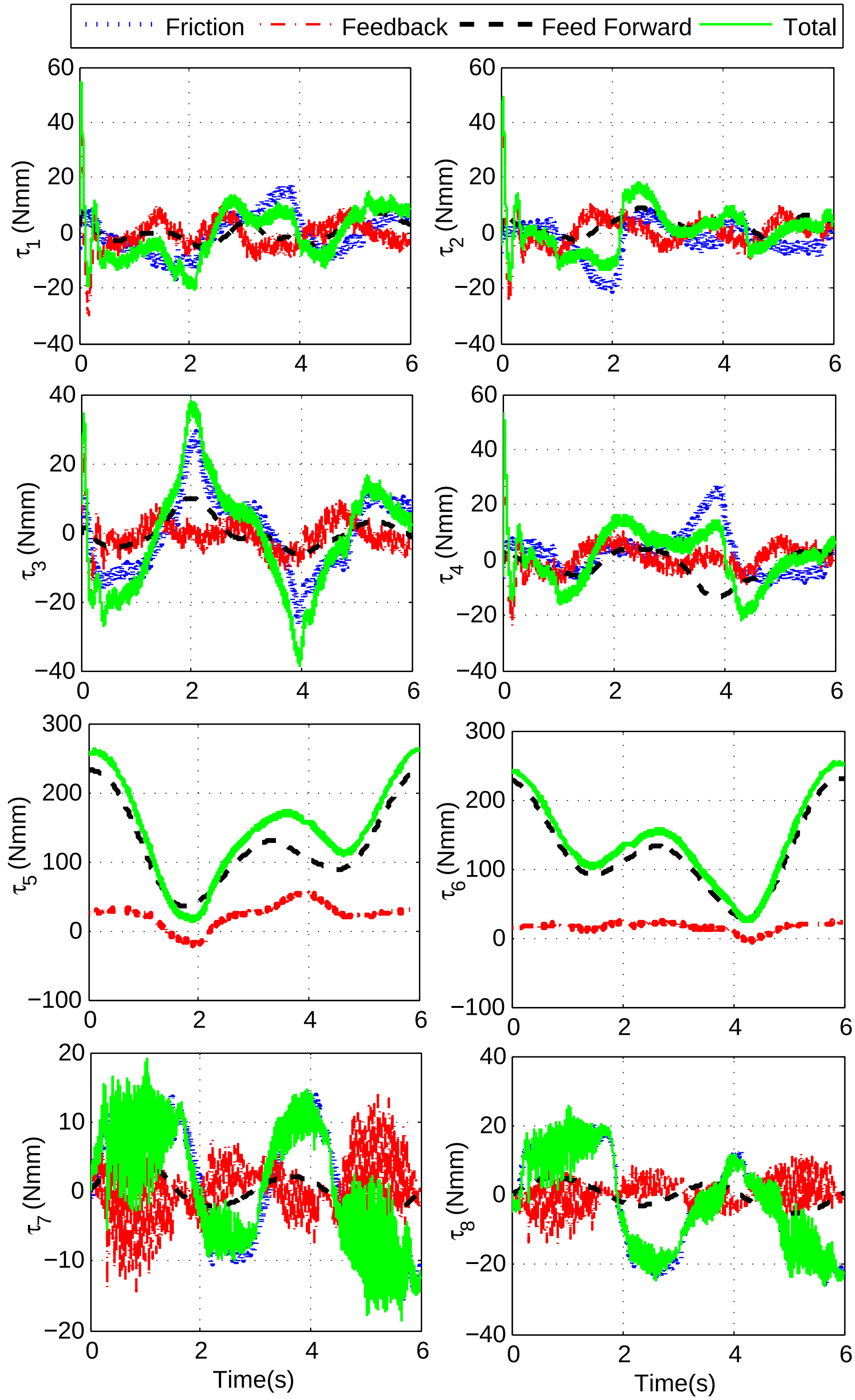

Figure 3.11: Individual joint torques during the tracking experiment using the model-based controller.

of the tracking error for the position of the 7-DOF Haptic Wand is 0.2703 mm for X, 0.1543 mm for Y, and 0.8165 mm for Z, and for its orientation is 0.2377° for ϕ, 0.1855° for θ, 0.4853° for ψ_l, and 0.3122° for ψ_u. Fig. 3.11 also shows the torque control command sent to the motors of the mechanism. Different parts of the control signal including friction, feedforward, feedback and the control signal in total are presented for each motor except for motors 5 and 6, where the friction was not discernible because of the uncertainty created by the wire connected to the motors and exertion of extra force when the mechanism moves in the Z direction. The results confirm that since the dynamics model of the 7-DOF Haptic Wand is accurate enough, the portion of the feedback torque is very low with respect to the total torque. In order to show the effectiveness of the model-based controller with higher tracking accuracy and lower PD control signal, the same experiment was repeated while using only a PD controller. The RMSEs of the tracking errors are 0.6498 mm for X, 0.3104 mm for Y, 11.5729 mm for Z for the position of the Haptic Wand and 0.6494° for ϕ, 0.2809° for θ, 0.5152° for ψ_l, and 0.3325° for ψ_u while higher torques required to compensate the model uncertainties.

The results show that using the model-based controller not only increases the accuracy of position tracking but also significantly decreases the feedback part of the torque control signal. The tracking is also greatly improved specially in the Z direction, where gravity has the most effect on the performance of the controller.

3.2 Controller Design

Fig. 3.12 shows the block diagram of two-channel position-force teleoperation architecture [96] for each arm. Here, X_m and X_s are the position of the master (the Haptic Wand) and the slave (the Mitsubishi PA10-7C robot), respectively. The workspace of the Haptic Wand was mapped to the workspace of the Mitsubishi PA10-7C robot using a position scaling factor C_1 (the scaled version of the operator's hand motion is the desired position command for the Mitsubishi PA10-7C robot). The interaction force between the da Vinci instrument and the tissue, F_e, was also scaled by the force C_2 and defined as the desired force command for the force-controlled Haptic Wand.

This section aims at describing different control approaches which have been used for the setup. First, the control architecture in which the master and slave communicate with each other is introduced. To reflect force feedback to the master side, the impedance control technique has been chosen for the Haptic Wand. In this method, the inherent impedance of the mechanism is first compensated using the dynamics model developed in this project, and then the desired impedance which is defined based on the required MIS application is given to the Haptic Wand. The other issue with the Haptic Wand control problem is the lack of force sensor at the master side to measure the interaction force between the operator's hand and the handle of

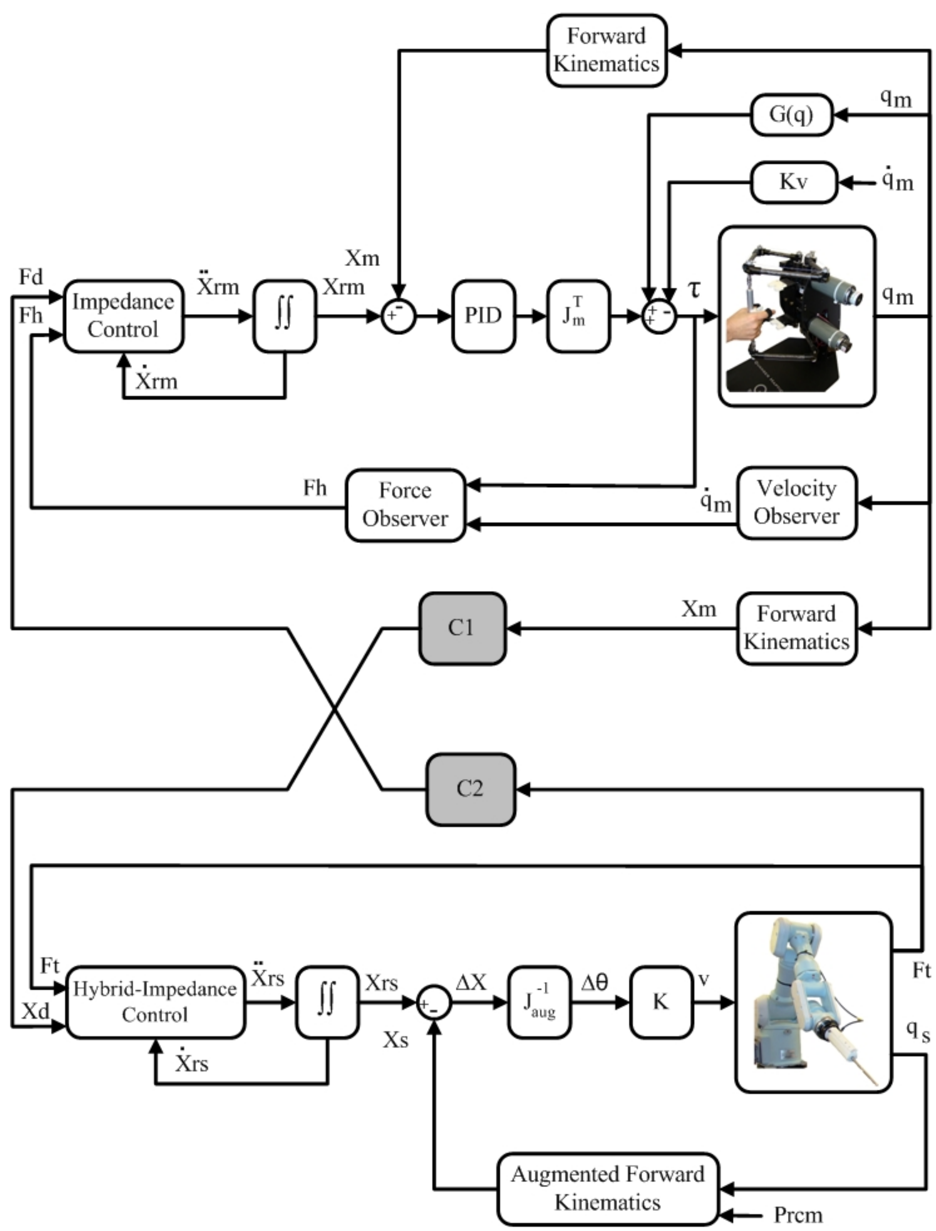

Figure 3.12: Control design block diagram for each single arm: Jacobian transpose impedance control at the master side and Jacobian inverse impedance control with software-based RCM at the slave side.

the Haptic Wand. To measure this interaction, a high gain force observer has been designed using the dynamics model developed for the Haptic Wand. On the other side, the slave manipulator should be able to switch between position and force control in different DOFs based on what is required for MIS task. Hybrid impedance control is the method which has been implemented on the slave side. This method attempts to generate a reference acceleration trajectory reflecting desired forces along the force-controlled subspace and the desired impedance along the position-controlled subspace. A software-based Remote Center of Motion (RCM) has also been generated at the slave side to enable the operator to pivot the instrument about the entry port in an MIS training box resembling patient's body. All control design algorithms were first implemented on a simulated slave manipulator in virtual reality in Simulink/Matlab.

3.2.1 Control Design Architecture

Two types of manipulations can be done in master-slave operations: unilateral teleoperation where the master unit only sends information to the slave robot and no information is sent back to the master, and bilateral teleoperation in which the master unit has the capability of force reflection and allows the surgeon to feel the interaction between the remote robot and its environment. Bilateral control architectures are also classified by the number of communication channels required for transmitting position and force. Three architectures have been used for bilateral teleoperation; two-channel, three-channel [97] and four-channel control architecture [96]. In all architectures, the objective is to control the position at the slave side to minimize the position and orientation errors in tool manipulation and the force control at the master side to allow the operator to feel the slave's contact with the environment. The most common architecture which has been used in the literature is the two channel architecture. This architecture has itself different configurations depending on the kind of signals that are being exchanged between the master and the slave. In the position exchange method (Position-Forward/Position-Feedback (PFPF)), the force feedback is provided without direct force sensing based on the position error between the master and slave manipulators. This indirect force measurement is proportional to the created position error. However, this architecture is very sensitive to feedback gain adjustments. If a low gain is chosen, high forces may not be detected and may damage the tissue. On the other hand, high gain force feedback causes a sticky feeling in free motion and even when the slave manipulator is in free space, the operator receives some force feedback. The other two channel architecture which has

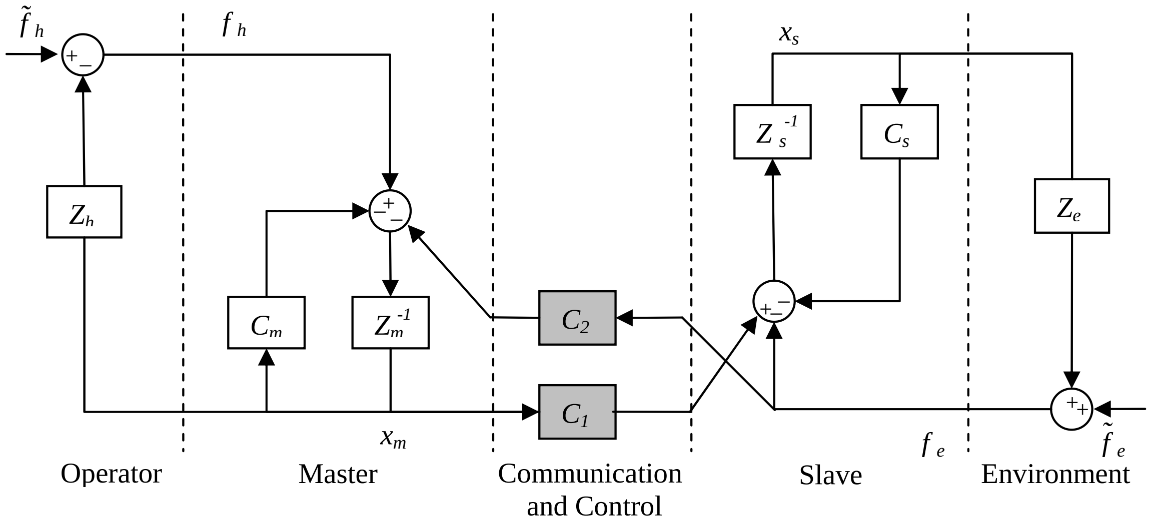

Figure 3.13: Block diagram of two-channel bilateral teleoperation used for the palpation setup.

been widely used is Position-Forward/Force-Feedback (PFFF) architecture. In this control structure, the command position imposed by the operator is fed forward from the master as input to the position-controlled slave, and the interaction force between the remote slave robot and its environment measured by a force sensor is fed back as input to the force-controlled master. This method requires a reliable force sensing system to measure tool-tissue interaction forces accurately.

Fig. 3.13 depicts the two channel PFFF bilateral teleoperation architecture where $\tilde{\boldsymbol{f}}_h$ and $\tilde{\boldsymbol{f}}_e$ represent the operator's and the environment's exogenous input forces, which are independent of the teleoperation system behavior. The hand/master and the slave/environment interactions (force or torque) are denoted by $\boldsymbol{f}_h$ and $\boldsymbol{f}_e$. The positions $\boldsymbol{x}_m$ and $\boldsymbol{x}_s$ denote the master and slave positions. The impedances $\boldsymbol{Z}_h$, $\boldsymbol{Z}_m$, $\boldsymbol{Z}_s$ and $\boldsymbol{Z}_e$ represent the dynamic characteristics of the operator's hand, the master robot, the slave robot and the remote environment. $\boldsymbol{C}_m$ and $\boldsymbol{C}_s$ denote the local position controllers and $\boldsymbol{C}_1$ and $\boldsymbol{C}_2$ are the two communication channels including coupling control for position forward and force backward, respectively.

3.2.2 Master Control Design

Impedance Control

The Jacobian Transpose Impedance Control (JTIC) scheme is chosen to control the force at the master side. In this approach, the dynamics of the robot's interaction are modeled in terms of a mass-spring-damper. The desired motion equation for the Haptic Wand is given by

$$\boldsymbol{M}_d\ddot{\boldsymbol{X}}_m + \boldsymbol{B}_d\dot{\boldsymbol{X}}_m + \boldsymbol{K}_d\boldsymbol{X}_m = \boldsymbol{F}_r + \boldsymbol{F}_h \tag{3.59}$$

where $\boldsymbol{M}_d$, $\boldsymbol{B}_d$ and $\boldsymbol{K}_d$ are the desired inertia, damping and stiffness, $\boldsymbol{F}_r$ is the desired force reflected from the slave and $\boldsymbol{F}_h$ is the interaction force applied by the operator to the Haptic Wand. $\boldsymbol{X}_m$, $\dot{\boldsymbol{X}}_m$, and $\ddot{\boldsymbol{X}}_m$ are the vector of position, velocity and acceleration of the Haptic Wand end effector in Cartesian space, respectively. In order to get precise force control, we can also set the stiffness of the desired impedance to zero. The dynamics model of the Haptic Wand in Cartesian space is given in Eq. (3.55) as

$$\boldsymbol{M}_m\ddot{\boldsymbol{X}}_m + \boldsymbol{B}_m\dot{\boldsymbol{X}}_m + \boldsymbol{G}_m + \boldsymbol{F}_f = \boldsymbol{u}_m + \boldsymbol{F}_h \tag{3.60}$$

where $\boldsymbol{M}_m$, $\boldsymbol{B}_m$, and $\boldsymbol{G}_m$ denote the inertia matrix, Coriolis and centrifugal terms, and gravity of the Haptic Wand, respectively and $\boldsymbol{F}_f$ is the friction present in the mechanism. By combining Eqs. (3.59) and (3.60), the impedance control law, $\boldsymbol{u}_m$ is derived as follows

$$\begin{aligned}\boldsymbol{u}_m = {} & (\boldsymbol{M}_m\boldsymbol{M}_d^{-1} - \boldsymbol{I})\boldsymbol{F}_h + (\boldsymbol{B}_m - \boldsymbol{M}_m\boldsymbol{M}_d^{-1}\boldsymbol{B}_d)\dot{\boldsymbol{X}}_m \\ & + \boldsymbol{M}_m\boldsymbol{M}_d^{-1}\boldsymbol{F}_r - \boldsymbol{M}_m\boldsymbol{M}_d^{-1}\boldsymbol{K}_d\boldsymbol{X}_m + \boldsymbol{G}_m + \boldsymbol{F}_f\end{aligned} \tag{3.61}$$

and the motor torques required are given by $\boldsymbol{\tau_m} = \boldsymbol{J}_m^T\boldsymbol{u_m}$.

Observer Design

To implement the bilateral control method on the master-slave system and to control the force precisely at the master side, the interaction force between the operator's hand and the handle of the haptic device should be measured accurately. Since there is no force sensor attached to the haptic wand end effector to measure this force directly, a disturbance force observer is required to measure the interaction force between the operator's hand and the handle of the Haptic Wand. Different types of estimators can be employed. Here, a high gain force observer [98] is utilized to estimate the interaction force between the Haptic Wand and its environment. This observer has the following form

$$\begin{aligned} \dot{\boldsymbol{\rho}} &= -\gamma\,\boldsymbol{\rho} + \gamma\,(\boldsymbol{u}_m - (\boldsymbol{B}_m - \dot{\boldsymbol{M}}_m)\,\dot{\boldsymbol{X}}_m - \boldsymbol{G}_m) + \gamma^2\,\boldsymbol{M}_m\,\dot{\boldsymbol{X}}_m \\ \boldsymbol{F}_h &= \gamma\,\boldsymbol{M}_m\,\dot{\boldsymbol{X}}_m - \boldsymbol{\rho} \end{aligned} \tag{3.62}$$

where γ is a positive observer gain and $\boldsymbol{\rho}$ is an auxiliary variable defined for the observer.

In order to calculate $\dot{\boldsymbol{X}}_m$ we need to have angular velocity $\dot{\boldsymbol{q}}_m$. But since the velocities and accelerations are not directly measurable, they are computed purely from joint angle measurements. Differentiating the joint angles gives extremely noisy results because of the slow motion of the Haptic Wand then, we use a high-gain observer [95] to estimate it. By assuming $\boldsymbol{x}_1 = \hat{\boldsymbol{q}}_m$, $\boldsymbol{x}_2 = \hat{\dot{\boldsymbol{q}}}_m$, and $\boldsymbol{u} = \boldsymbol{q}_m$, we can write the equations for the high-gain observer for estimating $\hat{\dot{\boldsymbol{q}}}_m$ as follows [95]:

$$\begin{aligned} \epsilon\dot{\boldsymbol{x}}_1 &= \epsilon\boldsymbol{x}_2 + \alpha_1(\boldsymbol{u} - \boldsymbol{x}_1) \\ \epsilon\dot{\boldsymbol{x}}_2 &= \alpha_2(\boldsymbol{u} - \boldsymbol{x}_1), \end{aligned} \tag{3.63}$$

where ϵ is a small positive constant, α_1 and α_2 are chosen so that the roots of $s^2 + \alpha_1 s + \alpha_2 = 0$ have negative real parts.

3.2.3 Slave Control Design

The control approach chosen for the slave manipulator is Jacobian Inverse Hybrid Impedance Control (JIHIC) with a software-based Remote Center of Motion (RCM). The software-based remote center of motion enables the operator to pivot the instrument about the entry port (trocar) in an MIS training box.

Hybrid Impedance Control

This method attempts to generate a reference acceleration trajectory reflecting desired forces along the force-controlled subspace and the desired impedance along the position-controlled subspace. This control method tries to regulate the tool-tissue interaction force while the robot is moving along a trajectory on the surface of the tissue. The reference acceleration trajectory for hybrid impedance control is as follows;

$$\ddot{\boldsymbol{X}}_r = \boldsymbol{M}_d^{-1}[-\boldsymbol{F}_e + (\boldsymbol{I}-\boldsymbol{S})\boldsymbol{F}_d - \boldsymbol{B}_d(\dot{\boldsymbol{X}}_r - \boldsymbol{S}\dot{\boldsymbol{X}}_d) - \boldsymbol{K}_d\boldsymbol{S}(\boldsymbol{X}_r - \boldsymbol{X}_d))] + \boldsymbol{S}\ddot{\boldsymbol{X}}_d \quad (3.64)$$

and

$$\boldsymbol{X}_r(0) = \boldsymbol{X}_s(0)\ ,\ \dot{\boldsymbol{X}}_r(0) = \dot{\boldsymbol{X}}_s(0), \quad (3.65)$$

where $\boldsymbol{M}_d$ and $\boldsymbol{B}_d$ denote the desired mass and damping parameters; $\boldsymbol{F}_d$ and $\boldsymbol{F}_e$ are the desired force and environment contact forces; The matrix $\boldsymbol{S}$ denotes the selection matrix that defines the force- and position-controlled subspaces ($\boldsymbol{S} = \boldsymbol{I}$ for entirely position-controlled and $\boldsymbol{S} = \boldsymbol{0}$ for entirely force-controlled); $\boldsymbol{X}_d$ is a 3×1 vector that represents the desired Cartesian position, $\dot{\boldsymbol{X}}_d$, and $\ddot{\boldsymbol{X}}_d$ are the corresponding velocity and acceleration.

For ease of analysis, we define the reference trajectory separately for the position and orientation subspaces. Eq. (3.64) results in

$$\begin{bmatrix} \ddot{\boldsymbol{x}}_r \\ \dot{\boldsymbol{\omega}}_r \end{bmatrix} = \boldsymbol{M}_d^{-1}[-\begin{bmatrix} \boldsymbol{f}_e \\ \boldsymbol{\tau}_e \end{bmatrix} + (\boldsymbol{I}-\boldsymbol{S})\begin{bmatrix} \boldsymbol{f}_d \\ \boldsymbol{\tau}_d \end{bmatrix} - \boldsymbol{B}_d(\begin{bmatrix} \dot{\boldsymbol{x}}_r \\ \boldsymbol{w}_r \end{bmatrix} - \boldsymbol{S}\begin{bmatrix} \dot{\boldsymbol{x}}_d \\ \boldsymbol{w}_d \end{bmatrix}) - \boldsymbol{K}_d\boldsymbol{S}\begin{bmatrix} \boldsymbol{e}_p \\ \boldsymbol{e}_o \end{bmatrix}] + \boldsymbol{S}\begin{bmatrix} \ddot{\boldsymbol{x}}_d \\ \dot{\boldsymbol{w}}_d \end{bmatrix} \quad (3.66)$$

and

$$\boldsymbol{x}_r(0) = \boldsymbol{x}_s(0)\ ,\ \dot{\boldsymbol{x}}_r(0) = 0,\ \boldsymbol{\omega}_r(0) = 0, \quad (3.67)$$

where $\boldsymbol{x}_r$ is the reference position and $\boldsymbol{\omega}_r$ is the reference angular velocity for the Mitsubishi PA10-7C robot. $\boldsymbol{e}_p$ and $\boldsymbol{e}_o$ are the position and orientation error between the desired trajectory (the command coming from the Haptic Wand) and the reference trajectory. In this form, we also separate force and torque for the position and orientation subspaces, respectively.

Remote Center of Motion

RCM can be implemented using a mechanically constrained kinematic structure or through software constraints, which is also called a virtual RCM [99]. Designing a mechanical structure for maintaining the RCM is usually more of interest in clinical applications because of the rigidity and safety that it brings by avoiding the effect of possible controller faults. But for research purposes, virtual RCM is more convenient

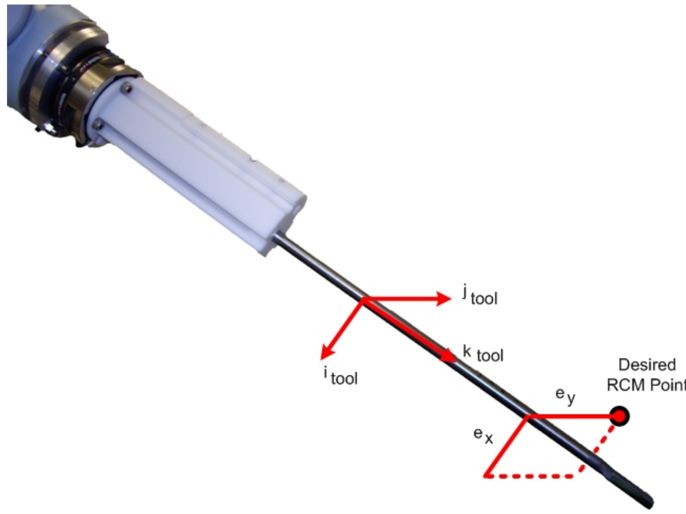

Figure 3.14: RCM error in the tool plane.

for implementation and can be easily generalized for different tasks.

There are different techniques for generating a software based RCM including a closed-form method which has been restricted to the cases where the end-point of the surgical tool is in line with the axis of the tool [99], and Configuration control [100] which incorporates the forward kinematics of the manipulator with two additional kinematic functions, one defined based on the RCM constraint and the other for objective functions, and arranged as augmented forward kinematics. There are two methods to calculate the RCM kinematic function: considering the error in the plane of the patient's skin (skin plane) or in the plane normal to the tool (tool plane). The approach chosen for this work is Configuration control with the error in the tool plane.

In this method, the displacement from the desired RCM to the tool shaft is computed as a two-dimensional vector in the tool plane (Fig. 3.14). The unit vectors of the tool plane, $(\boldsymbol{i}_{tool}, \boldsymbol{j}_{tool})$ can be extracted from the rotation matrix of the robot end effector as:

$$\boldsymbol{R} = \begin{bmatrix} \boldsymbol{i}_{tool} & \boldsymbol{j}_{tool} & \boldsymbol{k}_{tool} \end{bmatrix} \tag{3.68}$$

and $\boldsymbol{k}_{tool}$ is the unit vector of the tool axis (Fig. 3.14). The RCM error (e_x, e_y) is defined as the projection of the displacement between the desired RCM and the robot end effector onto the unit vectors $\boldsymbol{i}_{tool}$ and $\boldsymbol{j}_{tool}$:

$$\boldsymbol{d} = \boldsymbol{p}_t - \boldsymbol{p}_{rcm} \quad , \quad e_x = \boldsymbol{d}\,.\,\boldsymbol{i}_{tool} \quad , \quad e_y = \boldsymbol{d}\,.\,\boldsymbol{j}_{tool} \tag{3.69}$$

where $\boldsymbol{p}_t$ and $\boldsymbol{p}_{rcm}$ are the position of the tip of the laparoscopic instrument (the slave end effector is defined as the middle point of the sensor area) and the RCM point in the Mitsubishi PA10-7C robot world frame, respectively.

The kinematic function of the RCM is defined as

$$\boldsymbol{\mathcal{F}}_{rcm}(\boldsymbol{q}_s) = \begin{bmatrix} e_x \\ e_y \end{bmatrix} \tag{3.70}$$

where $\boldsymbol{q}_s$ is the joint angles of the Mitsubishi PA10-7C robot as the slave. Since a Jacobian-based method will be used for the position control of the Mitsubishi PA10-7C robot, let us compute the derivative of the RCM kinematic function with respect to the robot joint angles. Using the chain rule for calculating $\frac{\partial \boldsymbol{\mathcal{F}}_{rcm}}{\partial \boldsymbol{q}_s}$ and Eq. (3.69), the derivative of the RCM kinematic function can be calculated and is given by

$$\frac{\partial \boldsymbol{\mathcal{F}}_{rcm}}{\partial \boldsymbol{q}_s} = \begin{bmatrix} \boldsymbol{i}_{tool}^T \frac{\partial \boldsymbol{d}}{\partial \boldsymbol{q}_s} + \boldsymbol{d}^T \frac{\partial \boldsymbol{i}_{tool}}{\partial \boldsymbol{q}_s} \\ \boldsymbol{j}_{tool}^T \frac{\partial \boldsymbol{d}}{\partial \boldsymbol{q}_s} + \boldsymbol{d}^T \frac{\partial \boldsymbol{j}_{tool}}{\partial \boldsymbol{q}_s} \end{bmatrix} \tag{3.71}$$

Control Objective and Control Input Computation

The force and position controlled subspaces for the Mitsubishi PA10-7C robot are determined based on the required MIS application. For instance, for suturing application where the grasping mechanism is involved, we need to have a position-controlled subspace for translation and rotational motions of the Mitsubishi PA10-7C robot. However, for the grasping mechanism, we need the controller to switch between position and force control ($S_g^s = 1$ for position control and $S_g^s = 0$ for force control). In a real-life scenario, when a human tries to lift an object by his/her fingers, he or she grasps the object between his/her fingers and then, based on the mechanical properties of the object, decides how much force needs to be applied in order to hold that tight when moving around (force regulation). The same procedure needs to be carried out using master-slave teleoperation; position control for approaching to grasp the object and force control for holding that in motion without falling down.

For our dual-arm teleoperation setup, the controller at the slave side needs to use 7-DOFs of the motion to control the da Vinci end effector (three translations, three orientations, and grasping). Maintaining the RCM also requires 2-DOFs of the 10-DOFs available for controlling position. The last DOF is also used to hold the joint q_3 at zero (redundancy resolution). Therefore, the actual and desired control variables at the slave side are defined as

$$\begin{aligned} \boldsymbol{X}_s &= \begin{bmatrix} x_s & y_s & z_s & \alpha_s & \beta_s & \psi_{1s} & \psi_{2s} & e_x & e_y & q_3 \end{bmatrix}^T \\ \boldsymbol{X}_d &= \begin{bmatrix} x_m & y_m & z_m & \alpha_m & \beta_m & \psi_{1m} & \psi_{2m} & 0 & 0 & 0 \end{bmatrix}^T \end{aligned} \tag{3.72}$$

To implement hybrid impedance control for the slave system with the desired and actual control variables defined in Eq. (3.72), first of all we need to separate orientational variables from the rest. Using Eq. (3.66) and the initial conditions in Eq. (3.67), we can calculate the reference Cartesian position trajectory by double integrating $\ddot{\boldsymbol{x}}_r$. However, for the reference orientation trajectory, first of all we need to choose an appropriate orientation representation. In order to avoid singularities, a quaternion representation is chosen. A quaternion ε is defined as:

$$\varepsilon = \varepsilon_0 + \varepsilon_1 \boldsymbol{i} + \varepsilon_2 \boldsymbol{j} + \varepsilon_3 \boldsymbol{k}, \tag{3.73}$$

where the components ε_0, ε_1, ε_2, and ε_3 are scalars. Time derivative of the quaternion can be related to the angular velocity vector as:

$$\begin{bmatrix} \dot{\varepsilon}_0 \\ \dot{\varepsilon}_1 \\ \dot{\varepsilon}_2 \\ \dot{\varepsilon}_3 \end{bmatrix} = \frac{1}{2} \begin{bmatrix} -\varepsilon_1 & -\varepsilon_2 & -\varepsilon_3 \\ \varepsilon_0 & \varepsilon_3 & -\varepsilon_2 \\ -\varepsilon_3 & \varepsilon_0 & \varepsilon_1 \\ \varepsilon_2 & -\varepsilon_1 & \varepsilon_0 \end{bmatrix} \begin{bmatrix} \omega_x \\ \omega_y \\ \omega_z \end{bmatrix}, \tag{3.74}$$

Using the angular velocity obtained from Eq. (3.66) and assuming $\boldsymbol{\varepsilon}^r(0) = \boldsymbol{\varepsilon}(0)$, the reference quaternion trajectory can be achieved by integrating Eq. (3.74).

Now, with the reference trajectory for both position and orientation, the objective is to design the control input such that the robot end effector tracks precisely the reference position and orientation trajectory. First of all, the position and orientation error between the robot end effector and the reference trajectory needs to be calculated. The position error can be calculated as:

$$\boldsymbol{e}_p = \boldsymbol{x}_r - \boldsymbol{x}_s, \tag{3.75}$$

where $\boldsymbol{x}_s$ is the Cartesian position of the end effector with respect to the base frame. Special consideration should be given to account for orientation error calculation. To quantify the error between the actual end effector orientation ($\boldsymbol{\varepsilon}$) and the reference orientation ($\boldsymbol{\varepsilon}^r$), the rotation matrix from $\boldsymbol{\varepsilon}$ to $\boldsymbol{\varepsilon}^r$ is defined as $\boldsymbol{R}_e \triangleq \boldsymbol{R}_r\boldsymbol{R}^T$, where $\boldsymbol{R}$ is the rotation matrix of the robot end effector which can be obtained from the forward kinematics [101]. Given the reference quaternion, the matrix, $\boldsymbol{R}_r$, can be calculated as

$$\boldsymbol{R}_r = \begin{bmatrix} 1-2(\varepsilon_2^2+\varepsilon_3^2) & 2(\varepsilon_1\varepsilon_2-\varepsilon_0\varepsilon_3) & 2(\varepsilon_1\varepsilon_3+\varepsilon_0\varepsilon_2) \\ 2(\varepsilon_1\varepsilon_2+\varepsilon_0\varepsilon_3) & 1-2(\varepsilon_1^2+\varepsilon_3^2) & 2(\varepsilon_2\varepsilon_3-\varepsilon_0\varepsilon_1) \\ 2(\varepsilon_1\varepsilon_3-\varepsilon_0\varepsilon_2) & 2(\varepsilon_2\varepsilon_3+\varepsilon_0\varepsilon_1) & 1-2(\varepsilon_1^2+\varepsilon_2^2) \end{bmatrix} \tag{3.76}$$

The rotation matrix corresponding to the orientation error, $\boldsymbol{R}_e$, is assumed to be in the form

$$\boldsymbol{R}_e = \begin{bmatrix} \rho_{11} & \rho_{12} & \rho_{13} \\ \rho_{21} & \rho_{22} & \rho_{23} \\ \rho_{31} & \rho_{32} & \rho_{33} \end{bmatrix} \tag{3.77}$$

Now, we define the unit quaternion of the orientation error as

$$\boldsymbol{e}_q = \begin{bmatrix} \varepsilon_0^e & \varepsilon_1^e & \varepsilon_2^e & \varepsilon_3^e \end{bmatrix}^T \tag{3.78}$$

where

$$\begin{aligned} \varepsilon_0^e &= \cos\frac{\delta\theta}{2} & \varepsilon_1^e &= k_{e,x}\sin\frac{\delta\theta}{2} \\ \varepsilon_2^e &= k_{e,y}\sin\frac{\delta\theta}{2} & \varepsilon_3^e &= k_{e,z}\sin\frac{\delta\theta}{2} \end{aligned} \tag{3.79}$$

in which $\boldsymbol{k}_e$ is a 3×1 vector which represents the orientation error axis vector and $\delta\theta$ is the angle of rotation about the axis vector. In [102], it has been shown that the orientation error can be written as

$$\boldsymbol{e}_o = \boldsymbol{k_e}\sin\delta\theta \tag{3.80}$$

using Eq. (3.79), Eq. (3.80) results in

$$\boldsymbol{e}_o = 2\varepsilon_0^e \begin{bmatrix} \varepsilon_1^e & \varepsilon_2^e & \varepsilon_3^e \end{bmatrix}^T \tag{3.81}$$

On the other hand, for a given rotation matrix as in Eq. (3.77), the unit quaternion is computed as

$$
\begin{aligned}
\varepsilon_0^e &= \frac{1}{2}\sqrt{1+\rho_{11}+\rho_{22}+\rho_{33}} \\
\varepsilon_1^e &= \frac{\rho_{32}-\rho_{23}}{4\varepsilon_0^e} \\
\varepsilon_2^e &= \frac{\rho_{13}-\rho_{31}}{4\varepsilon_0^e} \\
\varepsilon_3^e &= \frac{\rho_{21}-\rho_{12}}{4\varepsilon_0^e}
\end{aligned} \tag{3.82}
$$

then, by combining Eqs. (3.81) and (3.82), the orientation error can be written as

$$
\boldsymbol{e}_o = \frac{1}{2}\begin{bmatrix} \rho_{32}-\rho_{23} \\ \rho_{13}-\rho_{31} \\ \rho_{21}-\rho_{12} \end{bmatrix}, \tag{3.83}
$$

To get full advantage of the well-tuned built-in controller for the Mitsubishi PA10-7C robot, we have used the Jacobian inverse method in velocity mode control of the Mitsubishi PA10-7C robot. By computing the position and orientation error, the control law in IJHIC method is given by

$$
\boldsymbol{v} = \boldsymbol{K}\,\boldsymbol{J}_{aug}^{-1}\,\boldsymbol{W}_x \begin{bmatrix} \boldsymbol{e}_p \\ \boldsymbol{e}_o \end{bmatrix} \tag{3.84}
$$

where $\boldsymbol{K}$ is the proportional gain to convert the joint-angle error to the reference velocity for the built-in PA10 velocity mode controller. $\boldsymbol{J}_{aug}$ is defined as follows:

$$
\boldsymbol{J}_{aug}(\boldsymbol{q}_s) = \frac{\partial \boldsymbol{\mathcal{F}}_{aug}(\boldsymbol{q}_s)}{\partial(q_{s_1},\ldots,q_{s_7})} \tag{3.85}
$$

and can be calculated as

$$
\boldsymbol{J}_{aug}(\boldsymbol{q}_s) = \begin{bmatrix} \boldsymbol{J}_p(\boldsymbol{q}_s) \\ \boldsymbol{J}_{rcm}(\boldsymbol{q}_s) \\ \boldsymbol{J}_{obj}(\boldsymbol{q}_s) \end{bmatrix} \tag{3.86}
$$

where $\boldsymbol{J}_p(\boldsymbol{q}_s)$ is the part of the Jacobian of the PA10 robot which is related to the position of the end effector, and

$$\boldsymbol{J}_{rcm} = \frac{\partial \boldsymbol{\mathcal{F}}_{rcm}}{\partial \boldsymbol{q}_s}$$

$$\boldsymbol{J}_{obj} = \begin{bmatrix} 0 & 0 & 1 & 0 & 0 & 0 & 0 \\ 0 & 0 & 0 & 0 & 0 & 0 & 1 \end{bmatrix} \tag{3.87}$$

In order to provide singularity robustness, $\boldsymbol{J}_{aug}^{-1}$ is typically calculated using a damped least-squares solution.

$$\boldsymbol{J}_{aug}^{-1} = [\boldsymbol{J}_{aug}^{T}\boldsymbol{W}_x\boldsymbol{J}_{aug} + \boldsymbol{W}_\theta]^{-1}\,\boldsymbol{J}_{aug}^{T} \tag{3.88}$$

where $\boldsymbol{W}_x$ and $\boldsymbol{W}_\theta$ are the weighting matrices for the task space and joint space velocities, respectively which are selected as follows:

$$\boldsymbol{W}_x = \boldsymbol{I} \qquad , \qquad \boldsymbol{W}_\theta = \lambda \boldsymbol{I} \tag{3.89}$$

where

$$\begin{aligned} \lambda &= \lambda_0 (1 - \frac{w}{w_o}^2), && \text{if} \quad w < w_0 \\ &= 0, && \text{if} \quad w \geq w_0 \end{aligned} \tag{3.90}$$

with $w = \sqrt{\boldsymbol{J}_{aug}\boldsymbol{J}_{aug}^{T}}$; λ_0 is a small positive value and w_0 is the threshold value [103].

3.2.4 Performance Evaluation of the Control System

Two challenging issues with a bilateral teleoperation system are to preserve the stability of the system and to maintain its transparency. Transparency is defined as a correspondence between the impedance perceived by the operator and that of the environment such that the remote environment is displayed in a natural way and the operator feels as if he or she is physically present at the remote environment. The issue of stability is normally addressed through an assumption of passivity of the master-slave interaction. However, this assumption is no longer valid for a dual-arm teleoperation system where the slave manipulators interact with each other and with tissue. Any interaction that injects energy may cause instability if it is not dissipated through an appropriate robust control strategy. One popular solution for dissipating the injected energy and ensuring the stability of the system is to add a damping element in the system. However, excessive damping can degrade transparency of the system. In general, there is a trade-off between transparency of the haptic interaction and stability of the system.

Two assumptions have been made in this project for designing the controller for the dual-arm teleoperation system: the operator moves the Haptic Wand slowly, and there is no hard contact between the remote instrument and its environment. These assumptions allow us to preserve the stability of the system by using an impedance matching technique and low-pass filtering of the reference signals for the master and the slave manipulators. In this method, the interaction impedance of the remote task was first estimated. Then, the inherent impedance of the Haptic Wand was compensated and the desired impedance that is chosen as the estimation of the remote task impedance was reflected to the operator. The reference signals were also passed through low-pass filters with cutoff frequency at 50 Hz in order to eliminate the high frequency content of the reference signals - the main source of the instability.

As mentioned earlier, any passivity-based method for providing closed-loop stability causes transparency deterioration for the haptic interaction, unless some considerations are taken into account: First of all, if the damping term of the desired impedance is set too high, it makes the system sluggish which requires the human operator to apply excessive force for manipulation. In order to meet both stability and transparency criteria for the dual-arm teleoperation system, this parameter needs to be tuned carefully: high enough to make the system stable but not to deteriorate its transparency. Low-pass filtering of the slave reference signal also makes the system less responsive to quick master movement. According to our first assumption, the operator moves the Haptic Wand slowly. Then, by filtering the high frequency part of the signal, the operator would not feel any latency in the motion mapping as long as he/she does not move the Haptic Wand quickly. On the other hand, low-pass filtering on the master reference signal can also lead to missing the high frequency content of the haptic information. Since the dual-arm teleoperation setup has been designed for the applications that deal with soft tissue without any hard contact, this would not affect the human perception from the remote environment.

Besides the conflicts between stability and transparency, force calibration error can also decrease the transparency of the system. Since the ATI force sensors which are used in our setup, are mounted between the wrist of the Mitsubishi PA10-7C robot

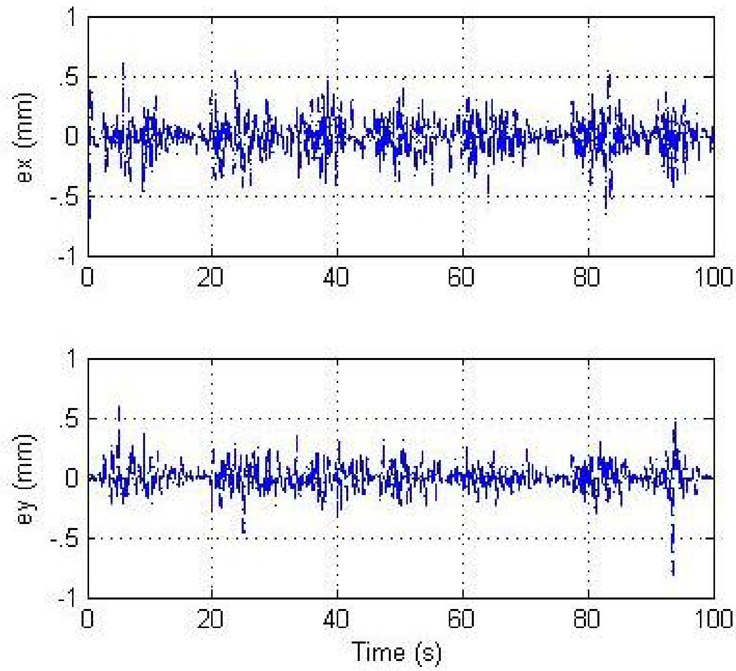

Figure 3.15: RCM error.

and the instrument, they measure not only the forces acting at the tip, but also the weight of the instrument. In order to compensate for the gravity effect of the instrument, which varies for different configurations of the Mitsubishi PA10-7C robot, a calibration software was developed that can estimate the location of the center of mass and the mass of the instrument regardless of the type of the instrument mounted on the force sensor. However, the dynamic effect of the instrument was not considered in this software resulting in some measurement error if the acceleration of the robot is not negligible. This error would then be reflected to the operator's hand resulting in transparency deterioration. The other source of error is the friction of the cables on which the strain gauges were mounted on. Although a mathematical model was fitted on the friction data obtained from the strain gauges while the instrument was moved in its workspace, there still exist some modeling errors that affect on the transparency of the system.

The RCM error is shown in Fig. 3.15 which shows that the error for maintaining the RCM is less than 1 mm. Fig. 3.16 also shows the transparency of the designed controller in the form of position and force tracking errors. As the results show, both reference trajectories were followed with satisfactory accuracy. The performance of the control system designed for the master-slave teleoperation was founded to be as

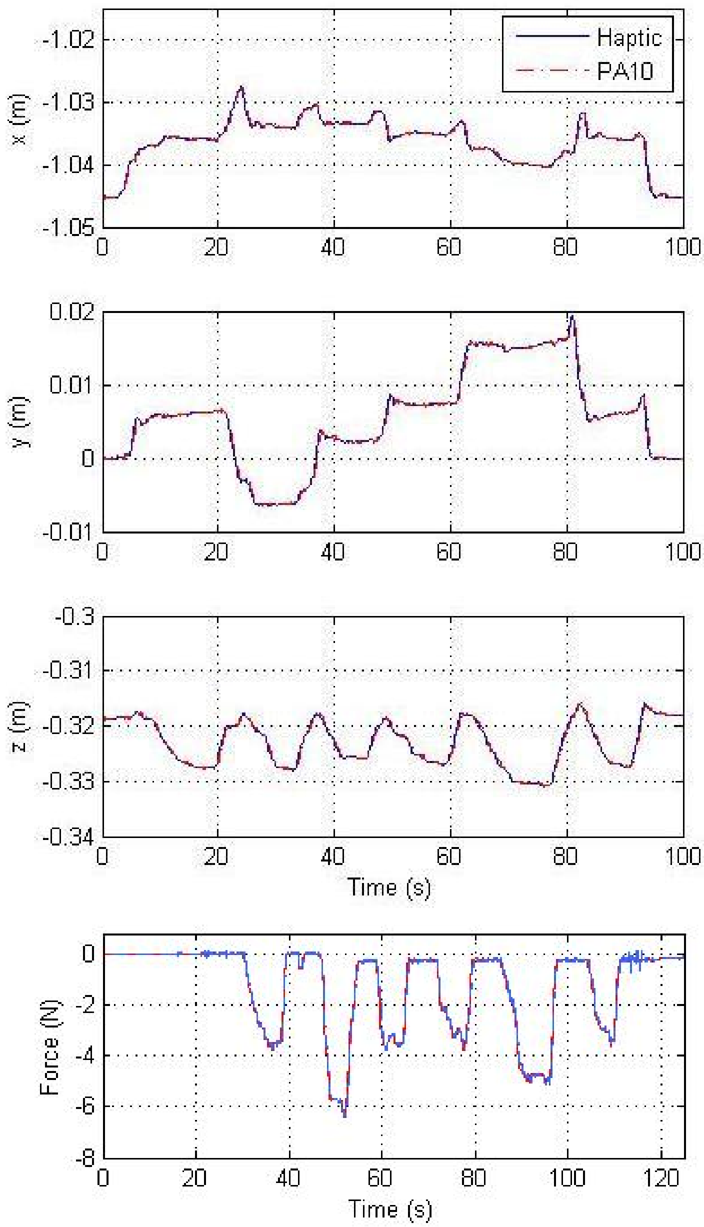

Figure 3.16: Position and force tracking for transparency evaluation.

follows: position accuracy= $0.1mm$, deadband= $0.2mm$, position bandwidth= $13Hz$, and time delay= $46ms$. The response to a step command from the master to the slave has $79ms$ of rise time, $261ms$ of settling time, zero overshoot and $0.1mm$ steady-state error.

Chapter 4

Application: Soft-Tissue Palpation

This chapter describes an application of the haptics-enabled teleoperation system described in the preceding chapters for tumor localization in soft-tissue palpation. Since the stiffness of a tumor is higher than that of healthy tissue, it can be distinguished as a hard nodule during palpation. Tactile sensing is a method that can be used in RAMIS to localize cancerous tumors prior performing ablative therapies. However, the performance of this method is highly dependent on the consistency of the exploration force applied to tissue. This chapter focuses on the application of haptics and tactile sensing for tumor localization. Force feedback in different modalities has been integrated with visual tactile feedback to improve the performance of the latter for tumor localization in RAMIS. In the first part of this chapter, the performance of each method is investigated. The methods include using visual tactile feedback, using direct reflection of force feedback, and using visual force feedback for detecting cancerous tumors in liver. Next, the results of tactile-force feedback are presented to explore how effectively force feedback can be incorporated with tactile sensing for tumor localization in liver cancer. In order to simulate the tumor localization procedure in a patient's body, some experiments have been designed to palpate liver tissue inside an MIS training box. The second application presented in this chapter is tumor localization for lung cancer. A new force-tactile method has been proposed for this application in which a hybrid impedance control approach has been used to automatically control the force in the palpation direction and thereby resolve the consistency problem concerning the exploration force.

The experimental setup developed for this application is shown in Fig. 4.1 which demonstrates the single-arm teleoperation setup for palpating liver tissue inside an

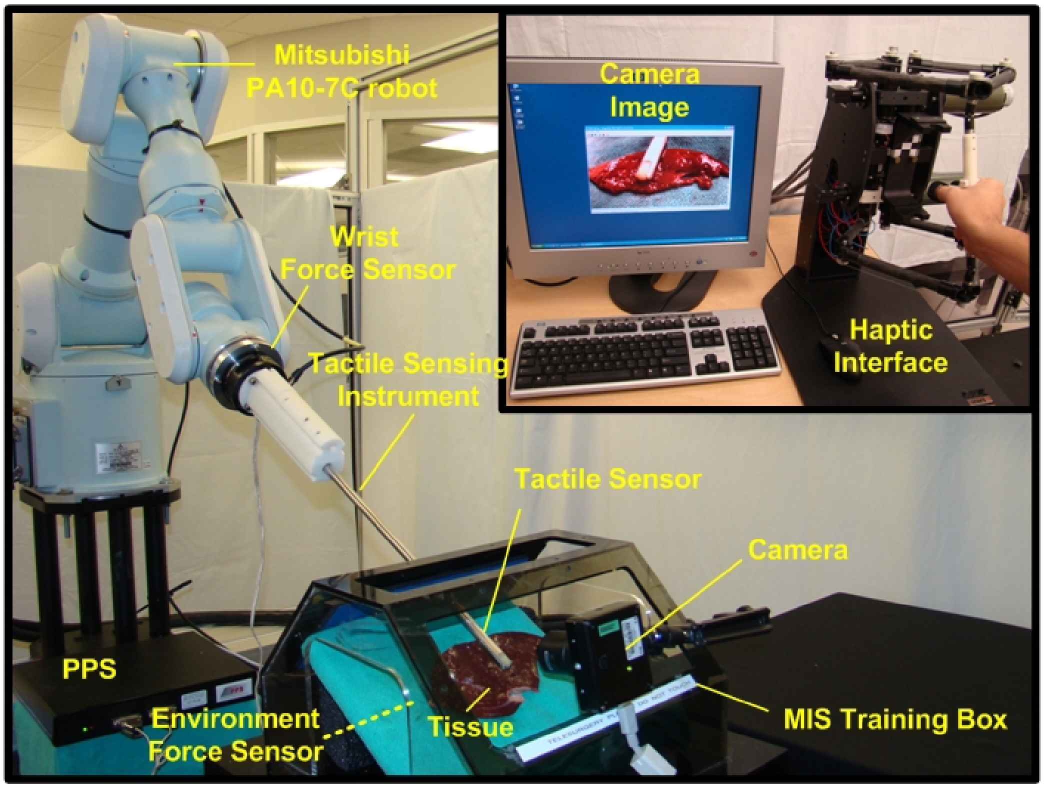

Figure 4.1: Master-slave robotic setup for palpating a bovine liver.

MIS training box representing a patient's body.

4.1 Tactile Sensing Tumor Localization

The tactile sensor used in this research is a two-dimensional array (15×4) of pressure sensing capacitive elements in a thin and continuous sheet (Pressure Profile Systems (PPS) Inc. [87]) developed for measuring the tactile pressure distribution between objects in direct physical contact. Each element is 2 mm $\times$2 mm and the total size of the sensor is 30 mm $\times$8 mm. This sensor is attached to a probe, with the shaft length of 385 mm and the shaft diameter of 10 mm, that is suitable for use in MIS. In order to address biocompatibility issues, a disposable laparoscopic latex sleeve is placed over the sensor and shaft of the probe. The tactile data obtained from the sensor contains information about the magnitudes, distributions and locations of forces. It also provides information about the contact area and the pressure distribution over it. The data obtained needs to be presented to the operator in a convenient and useful manner. The real-time Sapphire® acquisition and visualization software from

PPS were used to visualize the pressure distribution. The software converts the measured voltage values from the capacitive elements to pressure measurements, and displays the results in a color contour map of pressure distributions. Fig. 4.2 shows a screenshot of the pressure distribution produced by the software when a tumor is detected (- a second-order interpolation method has been used for visualization). As can be seen, this software utilizes the visual color spectrum to indicate the levels of localized pressure intensity experienced by the probe, with pink indicating the highest pressure intensity and blue indicating the lowest pressure intensity. Since the tumor is stiffer than the surrounding tissue, a tumor may be distinguished from the surrounding tissue by the highest pressure area indicated by the pink color in the contour map. This software also has a special feature to adjust the sensitivity of the color contour pressure map for an active display window.

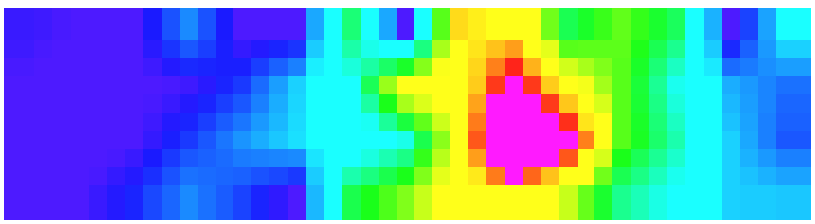

Figure 4.2: Pressure distribution diagram obtained from PPS visualization software showing the tumor in pink.

4.2 Force Feedback for Tumor Localization

As stated earlier, the main issue with the tactile sensing instrument (TSI) is how consistently it palpates tissue. Fig. 4.3 shows a phantom tissue being palpated by the TSI. For consistent palpation, the force applied by the operator on the tissue should be perpendicular to the tissue plane (f_p), otherwise it may lead to lateral forces on the tissue (f_{lx} and f_{ly}). On the other hand, the palpation plane which is defined as the plane parallel to the surface of the tactile sensor may cross the tissue surface at angles θ_1 and θ_2 because of an improper approach angle. This results in extra lateral forces applied on the tissue. As a consequence, some elements of the TSI would be under higher pressure while some of them may not be in contact with the tissue. Higher pressure applied on those elements may be interpreted as a tumor and lead to false positives. In order to keep the consistency of the applied force on the TSI during palpation, the lateral force in the tissue plane should be minimal. Since

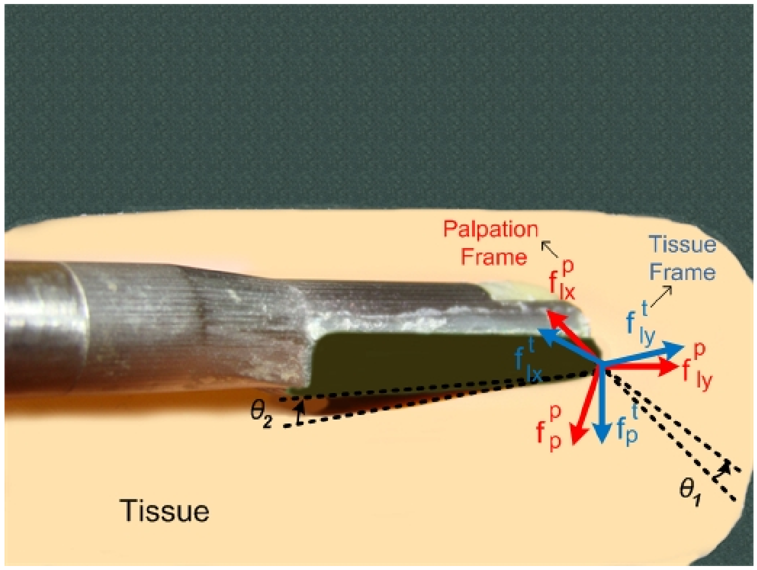

Figure 4.3: The force applied on the tissue during palpation on the tissue plane and the palpation plane.

the force measurements are known in the palpation plane, the force applied on the tissue plane can be obtained as

$$\begin{bmatrix} f^t_{lx} \\ f^t_{ly} \\ f^t_{lp} \end{bmatrix} = \boldsymbol{R}_y(\theta_2)\, \boldsymbol{R}_x(\theta_1) \begin{bmatrix} f^p_{lx} \\ f^p_{ly} \\ f^p_{p} \end{bmatrix} \tag{4.1}$$

where f^p and f^t are the forces in the palpation and tissue planes, respectively. On the other hand, since the operator has some visual cues during palpation from a camera overlooking the tissue (or, in the case of MIS, through an endoscopic camera), the angles θ_1 and θ_2 are always close to zero and the force measured in the palpation plane could be a measure of the force applied on the tissue in the tissue plane. Based on the characteristics of the palpation task, such as the stiffness of the tissue and the size and the depth of tumor, we require the exploration force being applied by the TSI to be in a specific range: high enough to deform the tissue and to identify pressure differences and below a threshold to avoid artifacts appearing in the tactile image and to prevent any damage to the tissue. Therefore, if we are able to reflect the lateral forces along with the palpation force to the operator's hand or monitor them on a screen, we would be able to get a consistent palpation by adjusting the motion of the slave robot through the Haptic Wand such that the operator feels minimum

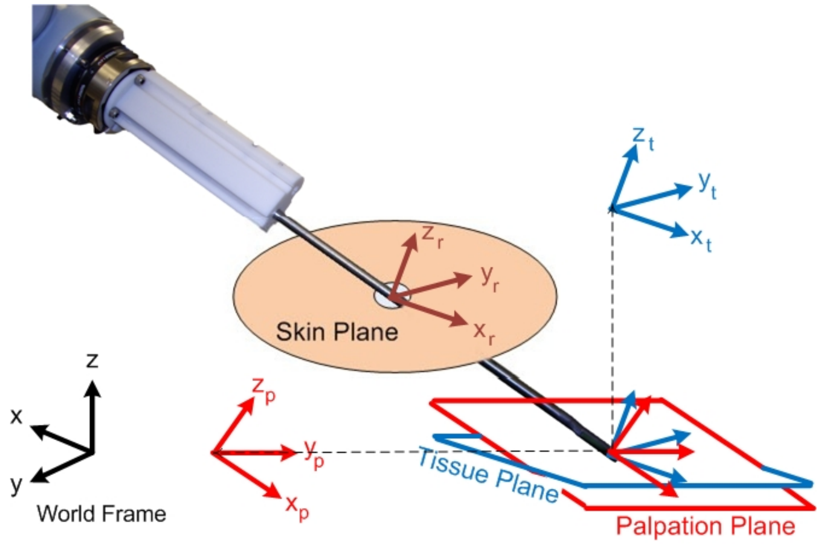

Figure 4.4: Position and force frames in a palpation task along with the slave world frame.

lateral force and a certain amount of palpation force reflected on his/her hand; or keeps the forces within a minimum range for the lateral forces and within a specific range for the palpation force.

Fig. 4.4 shows the position frame and force frame defined for the palpation task along with the world frame of the Mitsubishi PA10-7C robot. The control objective here is to change the orientation of the TSI such that the palpation plane fits over the tissue plane, and then to palpate the tissue in x_t-y_t plane. The palpation force along with the lateral forces measured in the force frame shown in Fig. 4.4 would also be reflected to the operator. The position of the TSI in the palpation frame can be calculated using the transformation matrix of the Mitsubishi PA10-7C robot.

4.3 Experimental Design

To evaluate the effect of force feedback in robot-assisted tactile sensing for tumor localization, the haptics-enabled master-slave teleoperation setup was used to perform soft-tissue palpation. The first objective was to compare the performance of tactile feedback with force feedback for tumor localization when the tissue was palpated remotely through a master-slave teleoperated system. Tactile feedback was provided in the form of pressure maps and force feedback was given either by direct reflection or visual presentation. The second and the main objective of this work was to see how effectively force feedback, in both forms - visual presentation and direct reflection, could be incorporated with tactile feedback to improve the overall performance of tumor localization. Five scenarios were considered for tumor localization:

1. Visual Presentation of Tactile Feedback (VPTF) through PPS software.
2. Direct Reflection of Force Feedback (DRFF) measured by the wrist force sensor.
3. Visual Presentation of Force Feedback (VPFF) measured by the wrist force sensor.
4. Visual Presentation of both Force Feedback and Tactile Feedback (VPTF+VPFF).
5. Visual Presentation of Tactile Feedback along with Direct Reflection of Force Feedback to the operator's hand (VPTF+DRFF).

In this work, we address the following problems: Can tactile feedback or force feedback alone be successfully used for tumor localization? In which case will they fail and lead to false positives or false negatives? Can force feedback be integrated with tactile feedback to improve its performance in tumor localization? Which presentation of force feedback is most effective for tumor localization and easier to use for the operator? In this section, we first run a preliminary study on the performance of tumor localization in different methods using a single operator with multiple attempts (the results presented are the samples of the repeatable trials), then three scenarios are chosen for further experimental consideration with the participation of several subjects in order to quantitatively assess the effectiveness of force feedback in tumor localization based on tactile sensing.

4.3.1 Tissue Models

The tissue used for the experiments was ex vivo bovine liver obtained from a local store. Tumors embedded in the tissue were artificial hemispheres made from thermoplastic adhesive (hot-melt glue) in two sizes: the large size with 8 mm diameter (chosen to be the same as the width of the TSI) and the smaller one with 5 mm diameter. These tumors were embedded in the underside of the liver. For ease of use and to provide a wider range of motion during the experiments, the tissue samples were

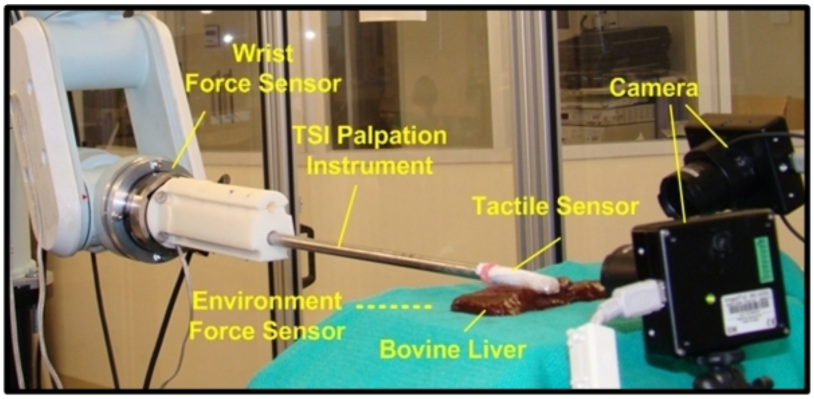

(a) Palpating the tissue placed on a table.

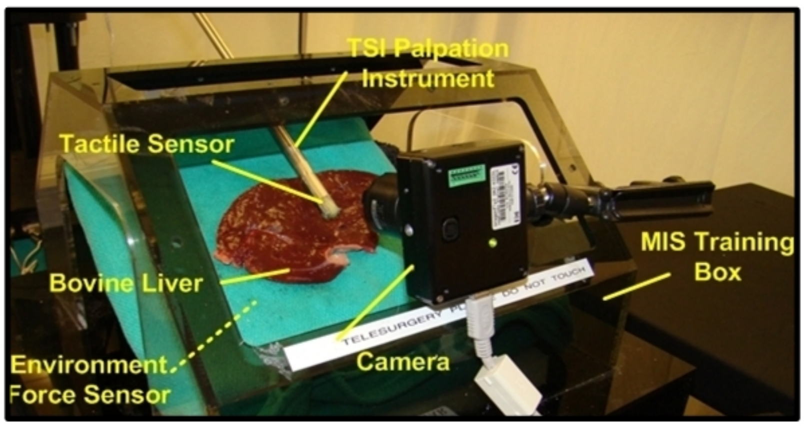

(b) Palpating the tissue in the MIS training box.

Figure 4.5: Test-bed for tumor localization

placed on a table and palpated in left to right direction (Fig. 4.5(a)). For simulating the palpation procedure in a patient's body, some experiments were also performed inside an MIS training box as shown in Fig. 4.5(b). Fig. 4.6 shows the locations of the tumors and the starting position of the TSI when the tissue was palpated on the table (Fig. 4.6(a)-(b)) and when it was palpated in the MIS training box (Fig. 4.6(c)). The margin on the tissue also shows the palpation area (the width of the area was chosen equal to the the length of the tactile sensor to only explore tissue in one dimension, along the y-axis of the slave world frame). It should be mentioned that the operator could palpate the tissue in 2D, however, since the task completion time was a criterion to compare the performance of tumor localization in different methods, the operator was asked to palpate the tissue only in one dimension. In order to minimize damage to the liver samples during the experiments, the operators were asked to palpate the tissue in a discontinuous mode in different steps; palpating the first area, raising the TSI off the tissue, moving to the next area and repeating this

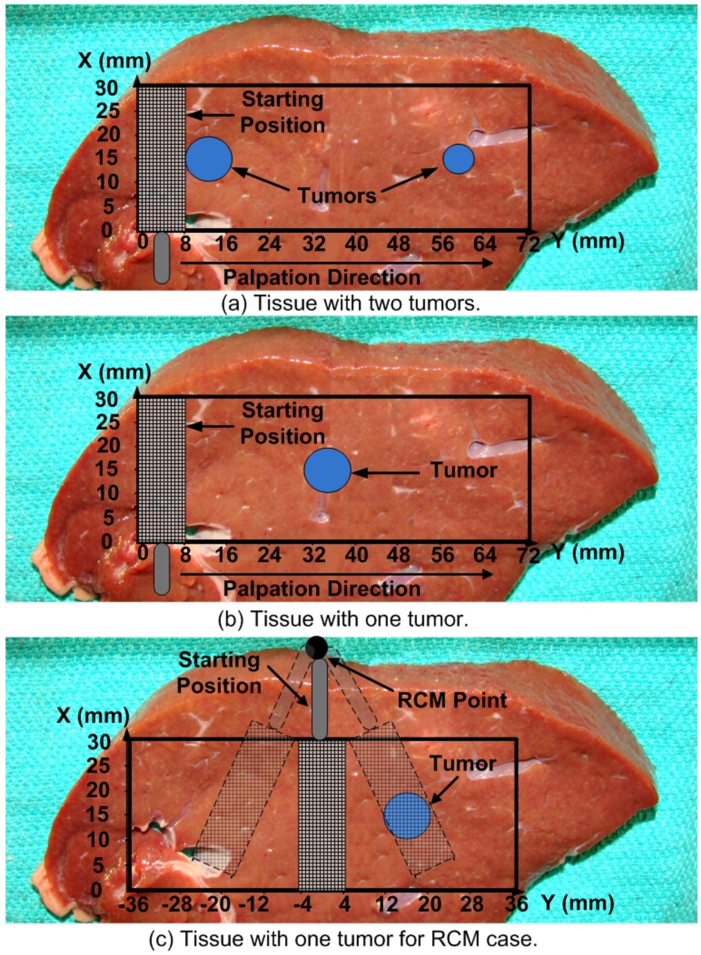

Figure 4.6: Exact locations of tumors embedded in the bovine liver used for the experiments.

approach. Fig. 4.6(a) shows the tissue with two tumors embedded, one large centered at $y = 12mm$, and one small centered at $y = 60mm$. Fig. 4.6(b) shows the tissue with one small tumor centered at $y = 36mm$. For palpation inside the MIS training box, the starting position was located at the middle of the tissue and one tumor was located at $y = 16mm$.

4.3.2 Performance Assessment Criteria

Four possible results may occur during palpating tissue for tumor localization: (1) a true positive occurs when the tumor is correctly identified and found in the tissue; (2) a false positive occurs when the user indicates that a tumor is found where none is located in that area; (3) a false negative occurs when the user does not find the tumor located in the tissue; and (4) a true negative occurs when the user correctly identifies that there is no tumor located in the tissue. A successful method for tumor localization is the one with zero false positive and negative. To measure the accuracy of tumor localization for the tumors found by the operator, the position profile of the TSI was recorded during the experiment. Once the operator located a tumor, a switch was pressed and the position data along with the force and tactile profiles were saved. This information was used later to assess the accuracy of tumor localization which is defined as the center-to-center distance between the exact location of the tumor embedded in the tissue (Fig. 4.6) and the measured location of the tumor found by the operator. The latter can be obtained either from the mapped pressure data on the tissue plane, the pink area, or from the position data at the time that the switch was pressed. Since the palpation was done in one direction, position data in y-direction would be enough to calculate the accuracy in tumor localization. The force exerted on the tissue during the experiment was also measured by the environment force sensor to see how much damage occurred during tumor localization in different methods.

4.3.3 Methods for Tumor Localization by a Single Operator

Tumor Localization using VPTF

The first scenario was to evaluate the performance of tactile sensing for lump detection using the tactile sensor at the tip of the TSI. In this scenario, the operator was asked to palpate the tissue through the master-slave teleoperation system and localize tumors using tactile pressure maps only which are provided on a monitor screen. A bovine liver with two tumors embedded in its underside was chosen to be palpated by the operator. The pressure distribution profile obtained from the PPS software and the force measured by the environment force sensor, indicating the force applied on the tissue during palpation, are shown in Fig. 4.7. The pressure distribution results were those presented to the operator during the experiment but the force diagram was plotted after finishing the experiment using MATLAB®. The average of the forces applied on the tissue is also shown in the bar graph in Fig. 4.7(b). As can be seen in Fig. 4.7(a), three areas with the highest pressure were distinguished by the color pink representing possible tumors in these locations. Using this method, two tumors were correctly detected with an accuracy of $0.03mm$ and $0.97mm$ at $y = 12.03mm$ and $y = 59.03mm$, respectively. one false positive also occurred at the location

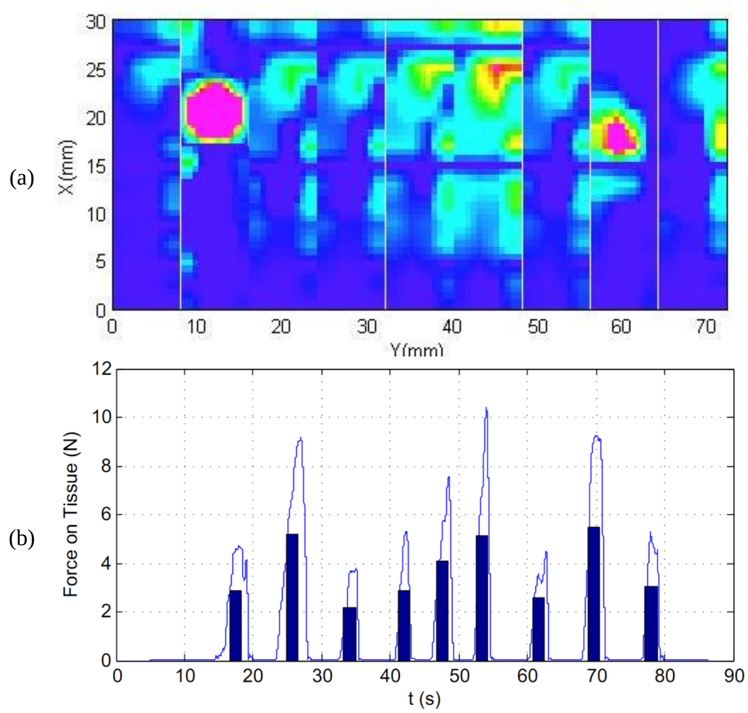

Figure 4.7: Results for the case using tactile feedback only: a) Pressure distribution map; b) Force applied on the tissue during palpation with the average force shown in the bar graph.

$y = 45.04mm$.

Tumor Localization using DRFF

In this scenario, the operator palpated a tissue sample with two embedded tumors while force feedback was reflected on his hand and the tumors detected based on higher force felt by the operator. The results presented in Fig. 4.8 were plotted after finishing the experiment in MATLAB® using 2D and 3D plot commands. Fig. 4.8(a) shows the average force felt by the operator when performing palpation. This force was measured by the force observer. The flag also shows the position where the operator found the tumor and pressed the switch ($y = 10.85mm$). The lateral forces measured during palpation are shown in 4.8(b) (the red lines show the minimum and maximum lateral forces during performing the task) and the force applied on the tissue is shown in Fig. 4.8(c). The results show that the operator could only find one tumor at the location $y = 10.85mm$. Using this method, the large tumor was correctly detected but one false negative occurred because of non-detection of the small tumor.

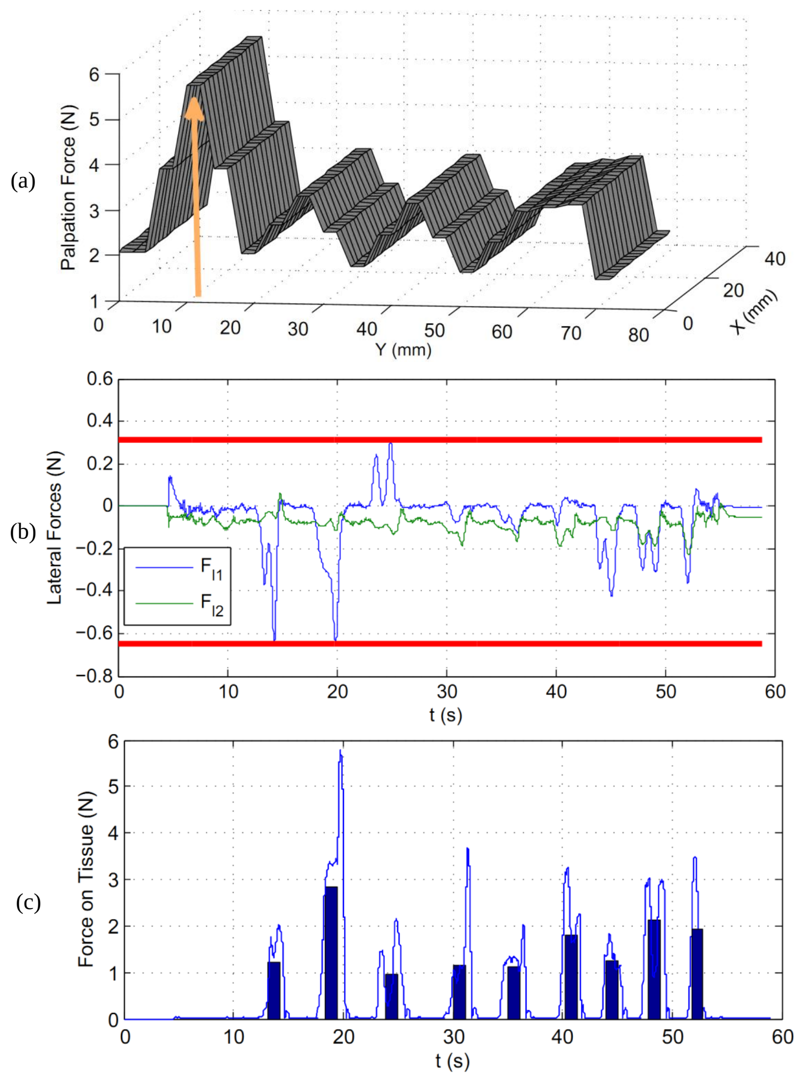

Figure 4.8: Results for the case using force feedback only, directly reflected to the operator's hand: a) Palpation force measured by the ATI force sensor; b) Lateral forces measured by the ATI force sensor; c) Force applied on the tissue during palpation with the average force shown in the bar graph.

Tumor Localization using VPFF

Visual force feedback was used to localize two tumors embedded in the bovine liver in this scenario. The operator was asked to keep the lateral forces within the range $\pm 0.5N$, and the force in the palpation direction close to 4N. He was also asked to palpate the tissue consistently by controlling the deformation of the tissue visually, and then decide about the location of possible tumors using the difference seen in the force profile in the palpation direction. Fig. 4.9(a) shows the force in the palpation direction. The lateral forces, with the desired range shown in red, and the force

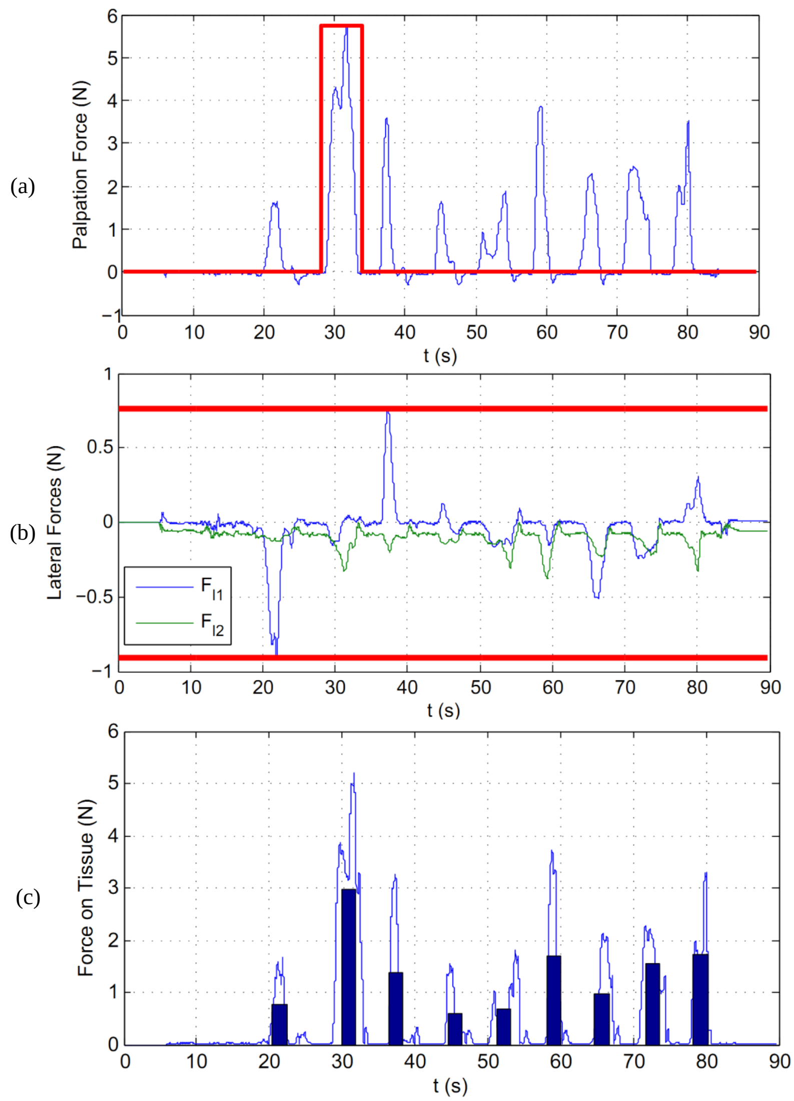

Figure 4.9: Results for the case using force feedback only, visually presented to the operator: a) Palpation force measured by the ATI force sensor; b) Lateral forces measured by the ATI force sensor; c) Force applied on the tissue during palpation with the average force shown in the bar graph.

applied on the tissue are also presented in Figs. 4.9(b) and 4.9(c) respectively. Both palpation and lateral forces were presented to the operator during the experiment but the force applied on the tissue was plotted after finishing the experiment in MATLAB®. The results achieved from this method show the possibility of one tumor at the location $y = 12.18mm$ according to the maximum force seen in Fig. 4.9(a). As can be seen from the results, both VPFF and DRFF methods ended up with detecting the large tumor at $y = 12mm$ with accuracies of $1.15mm$ and $0.18mm$, respectively.

Tumor Localization using VPFF+VPTF

This scenario was aimed at exploring the effect of visual force feedback during tactile sensing for tumor localization. For consistent palpation, the operator was asked to keep the lateral forces within the range $\pm 0.5N$. The ideal exploration force in the palpation direction was found to be 4N to locate tumors of the size 5-10 mm [78]. If the force exceeded 6N, it could cause damage to the tissue. For this reason in the scenario, the operator was asked to keep the exploration force within the range of 4N-5N. In this scenario, the operator decided the location of tumors using the pressure map presented to him. Fig. 4.10 show the results of palpation on tissue placed on a table when both force and tactile feedback were visually presented to the operator. Here, the same tissue with two embedded tumors was chosen. Figs. 4.10(a)-4.10(b) show the palpation force and lateral forces presented to the operator during the experiment respectively. The pressure distribution profile obtained from the PPS software during palpation is also shown in Fig. 4.10(c). Fig. 4.10(d) shows the flags placed at the positions where the operator found the tumors with the pressure profile mapped on it. This is an off-line fusion obtained after finishing the experiment using the 3D surface plot command in MATLAB®. The force profile measured by the environment force sensor is shown in Fig. 4.10(e). As can be seen, two tumors were detected by the operator at $y = 14.90mm$ and $y = 63.46mm$ with accuracy of $2.90mm$ and $3.46mm$ respectively.

Tumor Localization using DRFF+VPTF

To ensure consistency of the force applied during palpation in this scenario, both lateral forces and the force in the palpation direction were reflected to the operator's hand. In this scenario, the pressure distribution map was shown to the operator and the forces were reflected to his hand. In this way, the operator could control the palpation force to a level that was sufficient to deform the tissue while it was safe for the tissue. Meanwhile if a tumor was palpated, an extra force was applied to the operator's hand because of the higher stiffness of the tumor. Therefore, in this method, the tumor was detected either from the observation of the pink area in the pressure distribution map or from the higher force felt on the operator's hand. Lateral forces reflected to the operator's hand also prevented improper contact between the TSI and the tissue.

Fig. 4.11 shows the results of tumor localization using the DRFF+VPTF method.

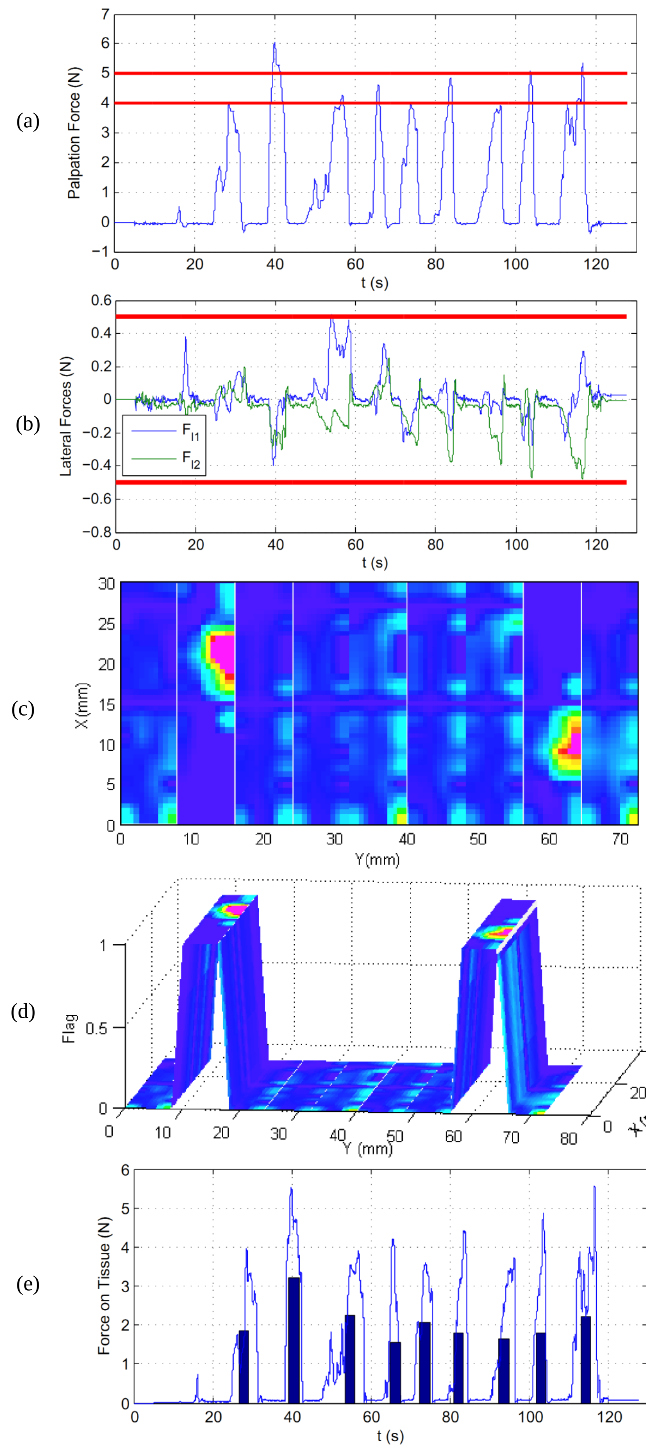

Figure 4.10: Results of force-tactile feedback fusion where force feedback presented visually to the operator: a) Palpation force measured by the ATI force sensor; b) Lateral forces measured by the ATI force sensor; c) Pressure distribution map; d) Pressure profile mapped on the flag sent by the operator; e) Force applied on the tissue during palpation with the average force shown in the bar graph.

(a)
(b)
(c)
(d)

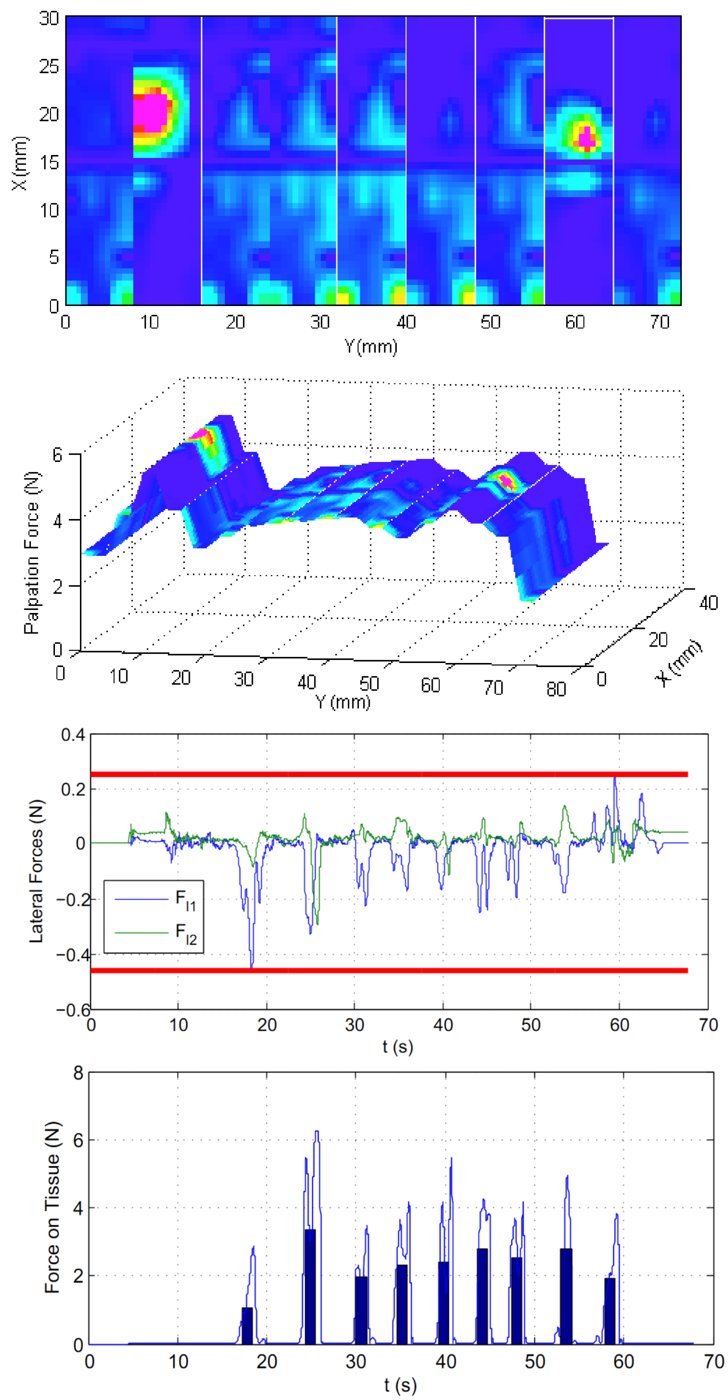

Figure 4.11: Results of force-tactile feedback fusion where force feedback is directly reflected to the operator's hand: a) Pressure distribution map; b) pressure profile mapped on the average force felt by the operator during palpation measured by the force observer; c) lateral forces felt by the operator and estimated by the force observer; d)force applied on the tissue during palpation with the average force shown in the bar graph.

Figs. 4.11(a) and 4.11(d) show the pressure map obtained from the PPS and the force applied on the tissue measured by the environment force sensor during palpation. The pressure profile is also mapped on the average palpation force reflected to the operator's hand and measured by the force observer in Fig. 4.11(b). Fig. 4.11(c) also shows the lateral forces applied by the TSI on the tissue and felt by the operator (the red lines show the minimum and maximum lateral forces applied during performing the task). The lateral forces shown here were estimated by the force observer. In this method, only pressure distribution map was the one that was presented to the operator during the experiment; other results were plotted after finishing the experiment using the 2D and 3D plot commands in MATLAB®. Fig. 4.11(b) is an off-line fusion of data which has been done in MATLAB® using the 3D surface plot command to map the pressure profile map onto the average force felt by the operator. Here, for the large tumor, the operator felt more force on his hand but for the small tumor, tactile feedback (not force feedback) confirmed the presence of the tumor in the tissue. These tumors were detected at $y = 10.71mm$ and $y = 60.80mm$ with accuracy of $1.29mm$ and $0.80mm$.

For simulating the palpation procedure in the patient's body, the last two scenarios were repeated but inside the MIS training box. The tissue here had just one tumor centered at $y = 16mm$ as shown in Fig. 4.6. Fig. 4.12 shows the results for the VPTF+VPFF method, and Fig. 4.13 shows the results of the VPTF+DRFF scenario. Here, palpation was done for different regions numbered from I to X. Since the slave end effector was defined at the middle of the TSI sensor area, and the tumor was almost found in the middle of the sensor area, the y-position of the slave end effector gave the position of the center of the tumor in that direction. Using the VPFF+VPTF method, the tumor was found at $y = 15.49mm$ with accuracy of $0.51mm$, and using the DRFF+VPTF method, it was detected at $y = 15.65mm$ with an accuracy of $0.65mm$. Both methods were successful in detecting the only tumor embedded in the tissue but direct force reflection showed better control on the lateral forces.

4.3.4 Performance Evaluation

This section deals with evaluating and analyzing the preliminary results of tumor localization achieved from different methods used by a single operator. The scenarios (1)-(3) explored the idea of using tactile feedback or force feedback individually. The

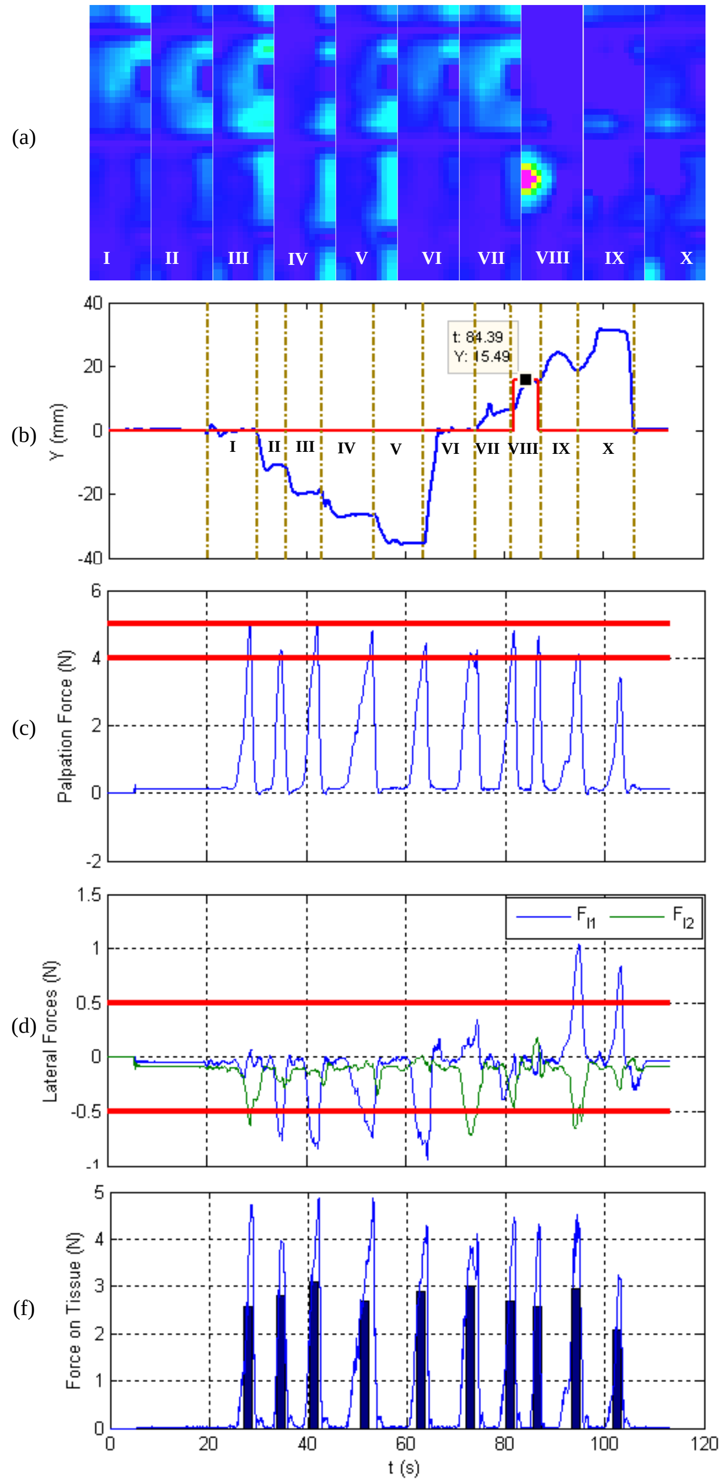

Figure 4.12: Results of force-tactile feedback when palpating in the MIS training box for the case where both force and tactile feedbacks visually presented to the operator: a) Pressure map; b) position of the tip of the tool in y-direction; c) palpation force; d) lateral forces; e) applied force on the tissue.

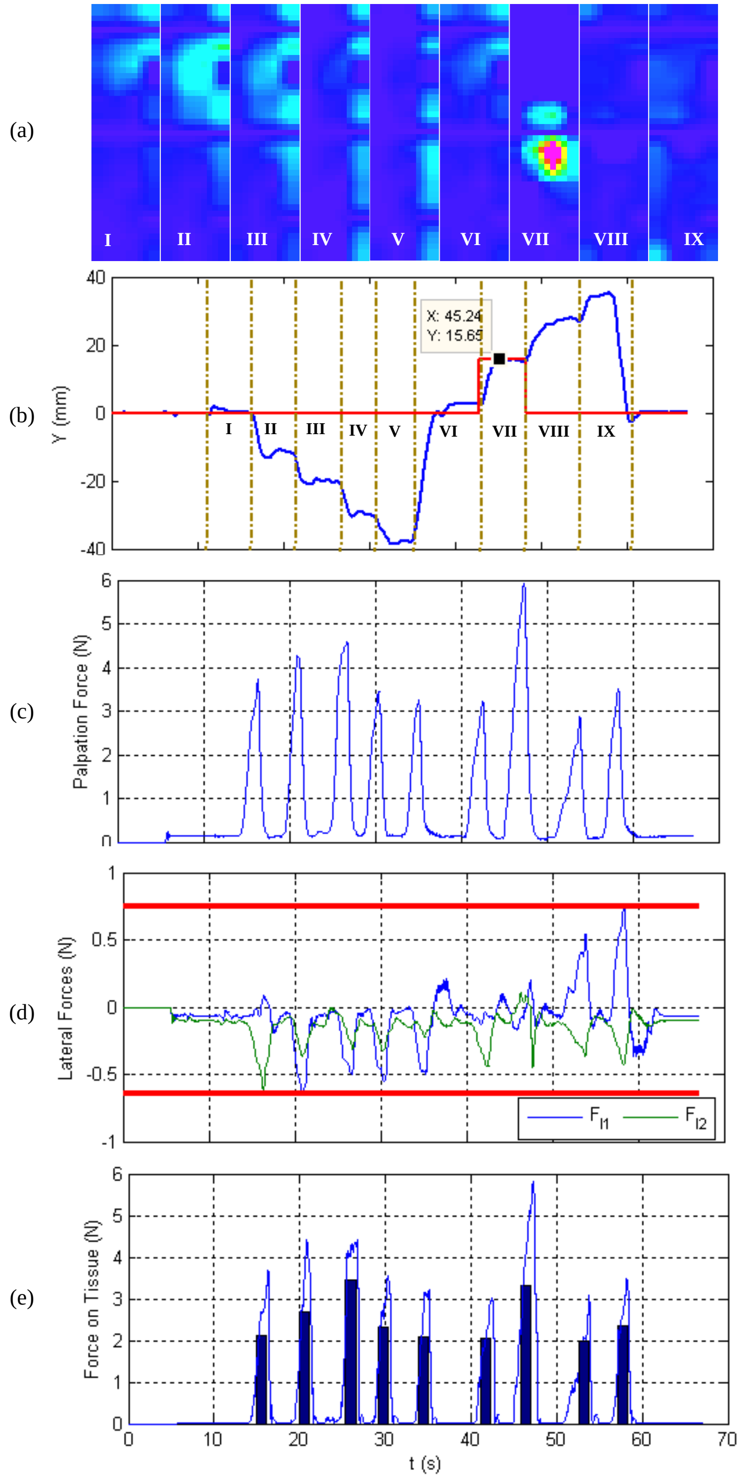

Figure 4.13: Results of force-tactile feedback when palpating in the MIS training box for the case of force feedback directly reflected to the operator's hand and tactile feedback visually presented: a) Pressure map; b) position of the tip of the tool in y-direction; c) palpation force; d) lateral forces; e) applied force on the tissue.

first scenario was tumor localization using tactile information only where the pressure distribution maps were presented to the operator through PPS software. Here one large and one small tumor were embedded in the bovine liver. The results showed that the operator was successful in detecting both tumors but the palpation done by the operator resulted in a false positive as well. The force diagram confirms that the operator applied too much force on the tissue which means the tissue palpated might be damaged. This diagram also confirms that quite a large force was applied by the operator over the area of $y = [40 - 48]mm$. The false positive for this area could be because of an improper contact of the TSI with the tissue and the large exploration force. As a result, some elements of the TSI were under more pressure that caused the PPS to detect that as a tumor.

Applying excessive exploration force during palpation, as perceived in this scenario, has a negative effect on the results obtained thereafter. The excessive force applied on the tissue creates a drift for some capacitive elements (depending on which elements are under high pressure) and makes the results unreliable. On the other hand, if too little force is applied, as perceived in some trials, the tactile sensor may not make proper contact with the tissue or may not deform the tissue sufficiently to be sensitive to an underlying tumor. As a result, a false negative occurs in tumor localization process. All these results show that the operator needs to control the force being applied on the tissue during tactile sensing tumor localization.

The next scenario was to explore the impact of using force feedback only in tumor localization. The force measurements were presented in two different ways; direct force reflection on the operator's hand and visual presentation of the force readings. In general, the results of using force feedback show that the idea of using force feedback for lump localization only works for large tumors where the difference in force feedback is significant and distinguishable and this method is unable to detect small tumors. The other important point achieved from the results is the necessity of getting feedback from lateral forces applied on the tissue which can avoid having false positives.

Between direct force reflection on the operator's hand and visual presentation of force reading on a screen, the results showed that since the operator felt the force on his hand in the first method, it was much easier for him to adjust the motion of the Haptic Wand to minimize lateral forces; Using the second method, on the other hand, needed more training for the operator to get used to it in order to not exceed the specified ranges. However, as stated earlier, the force feedback method is unable to detect small tumors and may lead to false negatives. All results from the first three scenarios show that force feedback or tactile feedback alone might not be enough to have successful tumor localization. Among these three individual methods, tactile feedback from the palpated area can provide more detailed information about the location of the tumor. However, the palpation task needs to be done in a force-controlled environment to ensure the consistency of the forces applied on tissue, to increase the accuracy of tumor localization and to guarantee the health of tissue.

Scenarios (4) and (5) aimed at using force feedback to ensure the consistency of the applied force on the tissue during palpation and to see the impact of force controlled environment in tactile-sensing tumor localization. Two scenarios were considered for incorporating force feedback with tactile feedback: the first scenario was to use visual force feedback to apply a certain amount of force in the palpation direction and to keep the lateral forces in the vicinity of zero. The results showed that the operator was absolutely successful in detecting the tumors embedded in the tissue. No false positives occurred in this scenario since the TSI palpated the tissue very smoothly. The force applied on the tissue never went beyond the safe range. In the second scenario, the palpation and lateral forces were reflected to the operator's hand while pressure maps were presented to him on a screen. The results obtained from this scenario also showed clear success in tumor localization both from the point of view of accuracy and from the point of view of the maximum force being applied on the tissue during palpation. The interesting point about this approach is the capability of auto force correction for the lateral forces which prevents improper contact between the TSI and the tissue by pushing the hand in a direction where the lateral forces become zero. Besides, direct force reflection can prevent applying too much force on tissue. In this scenario, the operator decided about the location of the tumor based on the force reflected to his/her hand and the pressure distribution obtained from the PPS software. As the results showed, the operator felt extra forces at the locations of the tumors. However, this method suffers from a side effect that there is no way to control the depth of palpation during experiment and if the operator pushed the TSI harder on a healthy area on the tissue, he/she would feel higher force and could not distinguish whether it was a tumor or not. However, for the visual presentation of the force feedback, there is more control on the force and the operator would apply force on the tissue until reaching the desired ranges specified on the monitor. The results of palpation inside the MIS training box also confirm that incorporating force feedback in either form with tactile feedback can result in successful tumor localization.

4.4 Experiments

To quantitatively assess the effectiveness of force feedback in robot-assisted tactile sensing, three scenarios were chosen for further considerations including visually presented tactile feedback only (VPTF), tactile feedback with visual force feedback (VPFF+VPTF), and tactile feedback with directly reflected force feedback (DRFF+VPTF). The main objective of this study was to evaluate quantitatively how force feedback could enhance the performance of tactile sensing for MIS tumor localization and determine which way of presenting force readings could be more effective in terms of accuracy and ease of use.

4.4.1 Experimental Conditions

Eight subjects were chosen for our study: one medical professional with previous experience with haptics, three subjects with some experience with haptics and four subjects with no experience with haptic feedback in teleoperated environments. These subjects were asked to palpate four ex vivo livers each (thirty two ex vivo livers were prepared in total). The livers had the possibility of containing from zero to two tumors (eight livers with no tumor, eight with one small tumor, eight livers with one large tumor, and eight livers with two tumors, one small and one large, but they were given to the subjects randomly). Presenting a liver with no embedded tumor allows the statistical results of specificity and negative predicted value to be determined. The subjects received some visual clues on a monitor from a camera overlooking the tissue but it was not possible to discern the location of the lump in the tissue from the camera image. Figs. 4.6(a) and (b) show the tissues with the location of the tumors embedded. Each subject palpated each of the livers three times for three different scenarios. Before the experiment, the subjects were trained to use the master-slave teleoperation system for tumor localization and they were allowed practice trials until they became comfortable with use of the setup for palpation. In this experiment, the livers were placed on the table and the subjects were asked to use the master to palpate the tissue using the TSI through the slave in left-right direction in one dimension (Fig. 4.5(a)).

4.4.2 Experimental Procedure

In the first trial, the only information provided to the subjects was the color contour map produced by the PPS software and the subjects were asked to find the tumor by looking at the pressure distribution profile when they palpated the tissue using the TSI. In the second trial, force was also reflected to the subjects' hands. The subjects were asked to decide about the location of the tumor based on the pressure map and the force reflected on their hands. In the third trial, force feedback was presented to the subjects on a screen including the palpation force and the lateral forces they applied during palpation. The subjects were told to keep the lateral forces in the range of $\pm 0.5N$ and the palpation force within the range of 4N-5N and then decide about the location of tumors based on what they observed on the pressure maps.

4.4.3 Performance Assessment Criteria

Various criteria were employed to evaluate the performance of the subjects for tumor localization in different methods. Statistical measures are the most common metrics used to asses the effectiveness of a diagnostic test: accuracy which represents the proportion of the tests that were successful in identifying the presence or absence of a tumor; sensitivity which shows the proportion of the samples with tumors present and tested positive; specificity which indicates the proportion of the samples with no tumors and which tested negative; Positive Predictive Values (PPV) which denotes the proportion of the samples that tested positive and had a tumor; and Negative Predictive Values (NPV) which denotes the proportion of the samples that tested negative and had no tumor.

The average and maximum force applied on the tissue were also recorded for each trial to see how much damage occurred during tumor localization in different trials. These forces were measured by the environment force sensor.

The task completion time is the other criterion which is defined as the time required to locate the tumors in the tissue for each trial. The recorded time begins once the probe has touched the surface of the tissue and ended when the subject stops palpating the tissue.

Table 4.1: Accuracy measures of tumor localization using different methods

Method	Accuracy	Sensitivity	Specificity	PPV	NPV
VPTF	55%	81%	6%	62%	14%
VPTF+DRFF	74%	84%	45%	82%	50%
VPTF+VPFF	83%	88%	63%	90%	56%

Table 4.2: Forces applied and task completion time for the various tests

Method	Favg (N)	Fmax (N)	Tct (s)
VPTF	7.10±2.64	15.09±4.37	131±51
VPTF+DRFF	2.80±0.84	7.81±2.20	119±40
VPTF+VPFF	3.21±0.45	6.43±0.78	160±56

4.4.4 Results and Discussion

Table 4.1 shows the statistical measures obtained from tumor localization in different methods. These statistical measures are also displayed in the bar graph in Fig. 4.14(a). Fig. 4.14(b) shows the accuracy results for the cases that the tissue contained only small or large tumors. Table 4.2 shows these forces along with the average task completion time for each method. The scaled results are also presented in Fig. 4.14(c) (force scale=5, time scale=0.4).

Among these three methods, the results show the best performance for the VPTF+VPFF method: 50% increase in tumor localization accuracy, 8% increase in sensitivity, huge improvement in specificity (close to 10 times), 46% increase in PPV and more than 280% improvement in NPV when compared with the results obtained from the method using tactile feedback only. These improvements were achieved while the average and maximum force applied to the tissue were decreased by more than 55% and 57%, respectively when compared to those of using tactile information alone. However, the task completion time for this method, on average, was 22% longer than that for the tactile feedback method which was due to the time the subjects needed to keep the forces in the desired ranges. The following success rates were achieved for the case of

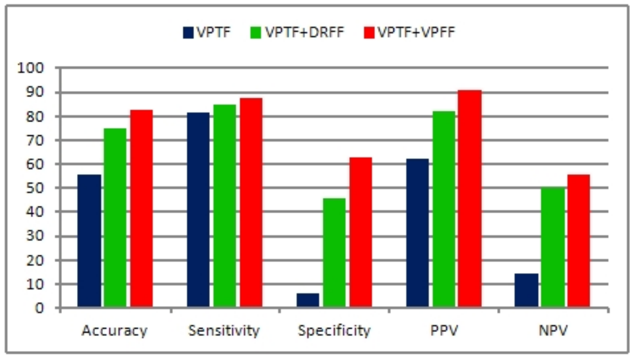

(a) Statistical measures.

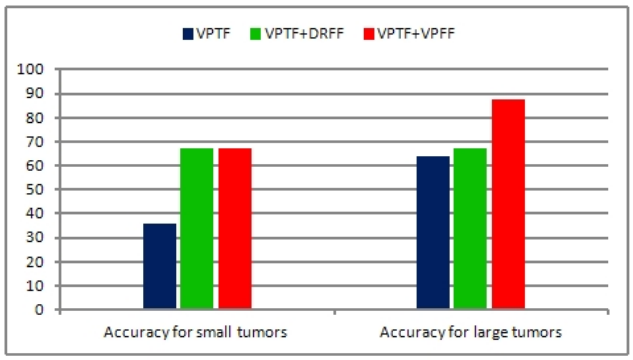

(b) Accuracy measure for the small and large tumors.

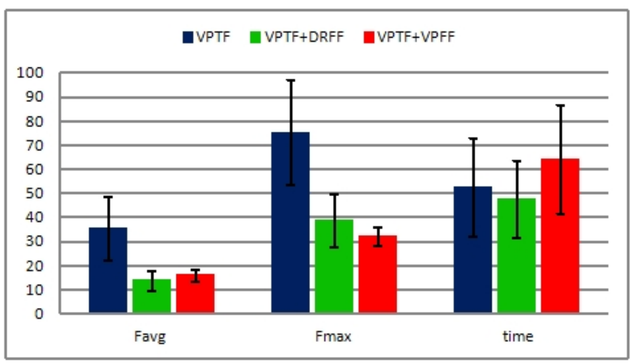

(c) Force applied on the tissue and the task completion time.

Figure 4.14: A bar graph comparison among the methods using tactile feedback only, force-tactile feedback fusion with visual presentation, and force-tactile feedback fusion with direct reflection.

using directly reflected force feedback incorporated with tactile feedback compared to the case using tactile feedback alone: 35% improvement in accuracy, 4% improvement in sensitivity, more than 670% improvement in specificity, 32% improvement in PPV and 250% improvement in NPV while decreasing the average and maximum force applied to the tissue 61%, and 48%, respectively. Using force feedback reflected to the participants' hands not only significantly decreased the amount of force applied on the tissue during palpation but also reduced the task completion time by 9%. Fig. 4.14(b) shows the performance of each method in tumor localization when there is only one small or one large tumor embedded in the tissue. The results show that the VPTF+VPFF method is more accurate for large tumors which indicates that the exploration force applied on the tissue containing one small tumor might not be enough to detect the tumor in all cases. The worst performance was also observed for the VPTF method for small tumors which was caused by numerous false positives detected during experiments because of too much exploration force applied on the tissue. Compared to the VPTF method for small tumors, both fusion methods showed better performance because of limiting the force applied on the tissue which resulted in significant decrease in the false positives. After finishing the experiments, each participant was asked to choose the method he/she was more comfortable with. Novice participants preferred to have visual feedback from the interaction forces since they could then better know how much force they were applying on the tissue, but they found it difficult to distinguish between forces when they felt them in 3DOF at the same time on their hands. Those who had some experience with haptics preferred direct force reflection on their hands; however, they pointed out that when they palpated a thicker part of the liver they felt higher force and they could not decide if there was any tumor in that region (they were asked to locate tumors based on either the pressure map or the force reflected to their hands). In the visual presentation of force feedback, they had this opportunity to push the TSI on the tissue until reaching the desired forces regardless of the thickness of the liver palpated and they decided only based on the pressure map. The main reason that the VPTF+DRFF method showed some success for tumor localization is because of preventing excessive forces on the tissue and thereby reducing the false positives that resulted in accuracy enhancement. However, the VPTF+VPFF method was much more successful in controlling the forces applied on the tissue and showed better achievements in accuracy measures. In conclusion, visual force feedback incorporated with tactile feedback was chosen as the method with the best performance for tumor localization in robotics-assisted master-slave soft-tissue palpation.

4.5 Tumor localization for Lung Cancer

In this application, we tried to implement palpation in a similar manner to that used by a surgeon during open surgery to detect a tumor. Assuming that the diseased tissue is accessible for a surgeon to directly palpate, the surgeon would detect a tumor by putting his/her finger on the tissue and sliding it over the tissue and using his/her sense of touch. In this way, the surgeon tries to apply a certain amount of force on the tissue during palpation. If during this process the tumor is felt, an extra force will be applied on the surgeon's finger because of the higher stiffness of the lump. The amount of force the surgeon needs to apply on the tissue depends on the stiffness of the tissue being palpated. It should be high enough to deform the tissue sufficiently to be sensitive to an underlying tumor and below a threshold to prevent any damage to the tissue.

In this work, we attempt to implement the same idea through our single-arm master-slave teleoperation system for use in the patient's body where direct palpation is not possible. The capacitive sensor at the tip of the TSI is treated as the surgeon's finger. The objective here is to slide the sensor over the tissue while maintaining a certain amount of exploration force during palpation. If the force applied in the palpation direction is sufficient, then by using the color contour map of the pressure distribution measured by the capacitive elements, we would be able to detect possible tumors in the tissue shown in dark red on the screen - since we needed to read the capacitive element outputs in MATLAB®, we have developed a visualization software for this application in MATLAB®.

By reflecting the force measured by the middle sensor on the operator's fingers through the Haptic Wand, the operator can obtain further confirmation of the location of the tumor found by the visualization software. To reach these objectives we define two control subspaces at the slave side: one in the palpation direction and the other in the tissue plane (the surface of tissue). For the first subspace we need to control the position of the instrument until reaching on top of the tissue. Then, we need a force control algorithm to apply a certain amount of force on the tissue to deform it sufficiently to capture the distribution of the pressure for that area. To explore the tissue for possible tumors, we need a position control approach over the tissue plane.

On the other side of teleoperation system, the Haptic Wand, we need a force control approach to reflect the measured forces (via the middle sensor of the TSI) to the grippers of the Haptic Wand. As stated in Chapter 3, impedance control is the method chosen to control the behavior of the Haptic Wand in our setup while interacting with the operator's hand. Since both force and position need to be controlled to achieve the control objectives at the slave side, hybrid impedance control [104] is used for the Mitsubishi PA10-7C manipulator while maintaining an RCM to pivot the palpator at the trocar (entry port in the body cavity).

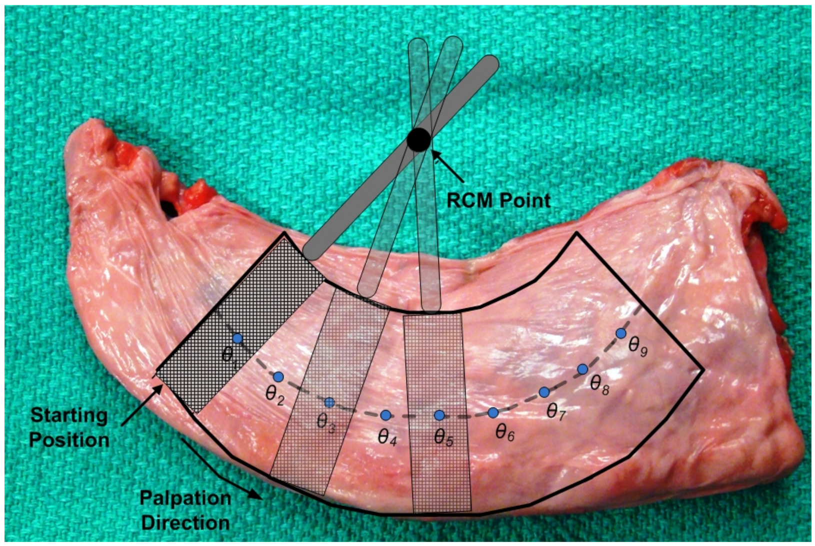

Figure 4.15: The lung tissue used for the experiment.

The control problem at the slave side is to change the orientation of the TSI, α_s and β_s, and its position along z_p direction such that the palpation plane fully fits over the tissue plane, and then to palpate the tissue in x_t-y_t plane (position-controlled subspace). Moreover, the force applied on the palpation direction (z_t-axis) should be kept at a certain magnitude to ensure that palpation is consistent (force-controlled subspace).

Seven participants were chosen to palpate six ex vivo lungs each (forty-two ex vivo lungs were prepared in total). The lungs had the possibility of containing from zero to two tumors. Fig. 4.15 shows the tissue with the starting position for the palpation. The tumors that we used for the experiments were artificial hemispherical nodules made from thermoplastic adhesive (hot-melt glue) of 8 mm diameter. They were embedded in the underside of the lung with their centers located at θ_3 and θ_8 for the case of tissue with two tumors and at θ_5 for the tissue with one tumor. The participants received some visual clues on a monitor connected to a camera overlooking the tissue but it was not possible to discern the location of the lump in the tissue from the camera image. They were asked to use the master to palpate the

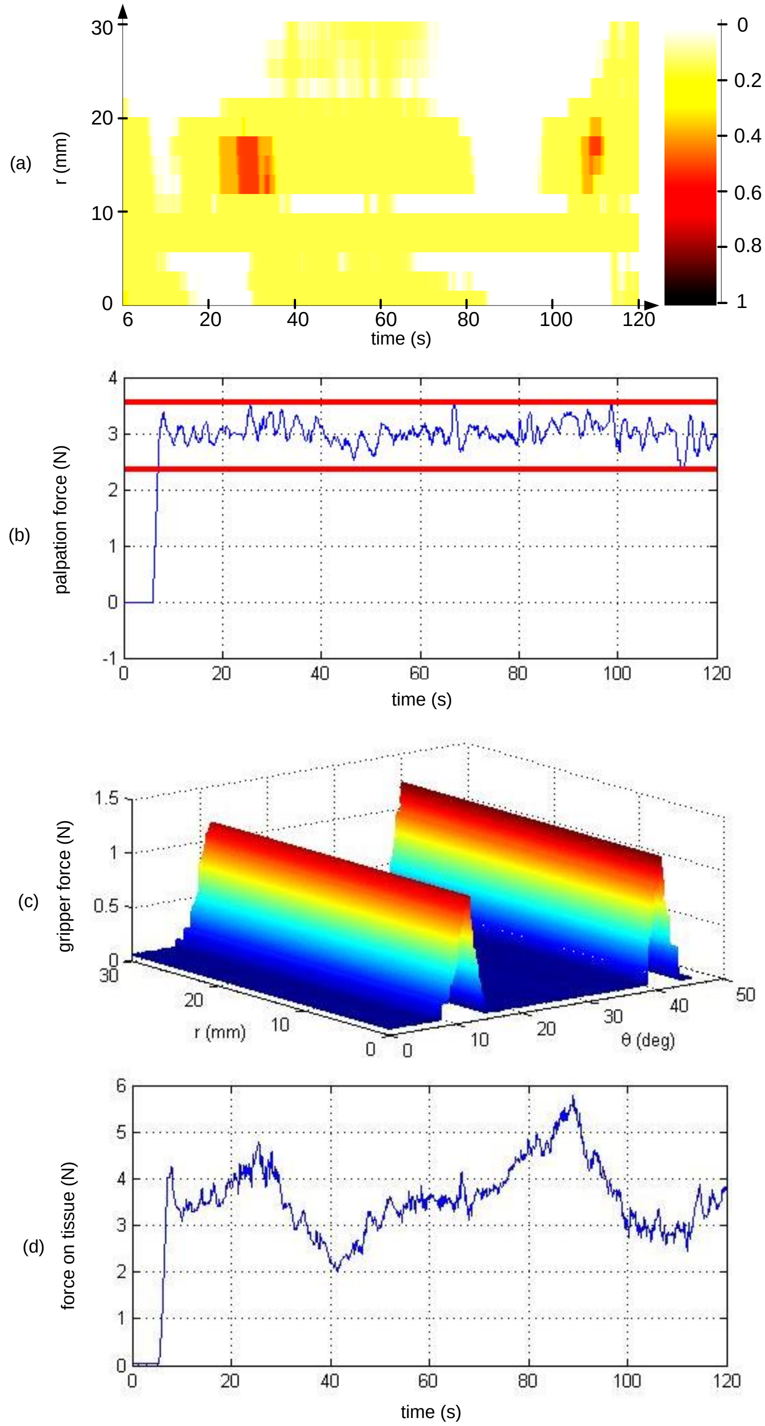

Figure 4.16: Sample graphs for the experimental results: (a) pressure distribution map; (b) exploration force applied on the tissue to localize tumors; (c) the force felt by the participant during the experiment measured via a high-gain observer and mapped on the palpation area; (d) the force applied on the tissue measured by an ATI force sensor underneath the tissue.

tissue using the TSI through the slave. A switch was provided to the participants enabling them to choose between position and force control subspaces for the palpation direction. For the other directions, the Mitsubishi PA10-7C robot was set to be in position controlled subspace commanded by the participant through the Haptic Wand. The participants were asked to turn the switch ON ($S_z = 1$) and bring the TSI on top of the starting position shown in Fig. 4.15 under position control then turn it OFF ($S_z = 0$) enabling the robot to approach the surface of tissue under force control while applying 3N on the tissue in the palpation direction (this is the amount of force tested to be successful for detecting the hidden tumors). Then, they were asked to palpate the tissue inside the margin shown in Fig. 4.15 while looking at the color counter map of the pressure distribution and move the TSI slowly over the tissue. The slow motion of the TSI gives the force control loop sufficient time to adjust the force applied on the tissue to 3N. The force measured by the middle sensor was also reflected to the participant's fingers through the Haptic Wand. If a tumor is found in the middle of the TSI, the operator would not only be able to see it in the pressure map but he/she would also could feel an extra force reflected on his/her fingers. During the experiments the position profile of the TSI was recorded to see how accurately the operator could localize the tumor. Once the operator located a tumor, a flag was set and the results were saved to be used later to assess the exact location of the tumor found by the operator and to calculate the accuracy of tumor localization. The total force applied on the tissue was also recorded using an ATI Gamma force sensor located underneath the tissue.

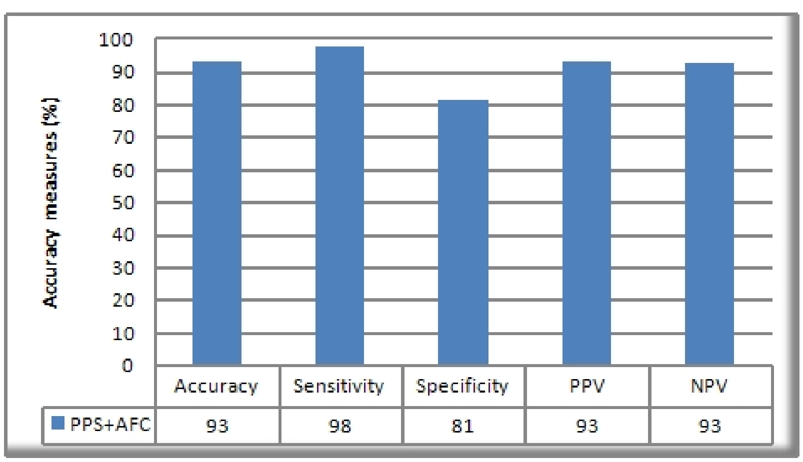

Figure 4.17: Accuracy measures on the results obtained from the experiments.

Some sample graphs have been chosen to show the results of tumor localization using the proposed method (Fig. 4.16). For this experiment, a lung with two tumors was palpated by one of the participants. Fig. 4.16(a) shows the color contour map of the pressure distribution. Two red-colored areas can be seen which show two tumors located in those regions. Fig. 4.16(b) shows the exploration force applied by the participant on the tissue during the experiment. This graph shows that the automatic force control loop successfully regulated the force in palpation direction around 3N. The force applied on the participant's fingers is also shown in Fig. 4.16(c) which is mapped on the palpated area, in r-θ coordinate. Since the tumors were located in the middle of the margin shown in Fig. 4.15, the participant felt them both when they were palpated. The results show that the maximum force was felt in the ranges $10.97° < \theta < 12.08°$ and $40.03° < \theta < 40.73°$. The total range of motion for this experiment was 45° and since the tumors were located at θ_3 and θ_8, the exact locations of the center of the tumors embedded in the tissue were at $\theta = 12°$ and $\theta = 40°$. Finally, the force applied on the tissue during palpation is shown in Fig. 4.16(d) which confirms that the force on the tissue did not exceed $6N$ (the threshold of the force that would cause damage to the tissue).

Fig. 4.17 shows a bar graph presenting performance measures obtained from the data collected in forty-two trials of the experiments performed by the participants. The results show that the proposed method was absolutely successful in detecting tumors embedded in the tissue while controlling the exploration forces applied on the tissue so as not to exceed the specific range determined by the operator.

Chapter 5

Application: Suturing

The second MIS application chosen for this project is endoscopic suturing in which two robot arms are needed to cooperate in accomplishing the task. Suturing is a task commonly used in surgical interventions and is one of the most complex tasks that requires precision and dexterity in movements, puncturing and knot tightening. The control of forces applied in suturing is critical in that the forces should be high enough to obtain a firm knot but should not damage tissue or break sutures. The hypothesis here is that haptic feedback can significantly help to decrease the number of broken sutures and avoid any damage to vessels and delicate tissue caused by over tightening the suture knot. The force/tension reflected to the surgeon's hand can not only be used to limit the force applied on the knot and thereby secure the health of tissue but also can ensure the surgeon that sufficient force is being applied to grasp tissue or suture without any slippage and loss of control.

Fig. 5.1 shows the master-slave teleoperation system with a cardiac surgeon performing a suturing task on a mitral valve. For a closer look at the whole procedure of suturing, the sequences of performing suturing on a phantom tissue using our dual arm teleoperation setup is illustrated in Fig. 5.2. The suturing task can be divided into two phases; stitching and knot tying. In order to assess the performance of suturing in the absence and presence of force feedback, each phase can also be broken down to different subtasks. The stitching phase includes three main subtasks; grabbing the needle and adjusting it to an appropriate position and orientation for insertion, inserting the needle with penetration of the tissue, and pulling the needle and the thread through the tissue. The knot tying phase can also be divided into three main subtasks: looping the thread around one of the instruments, grabbing the

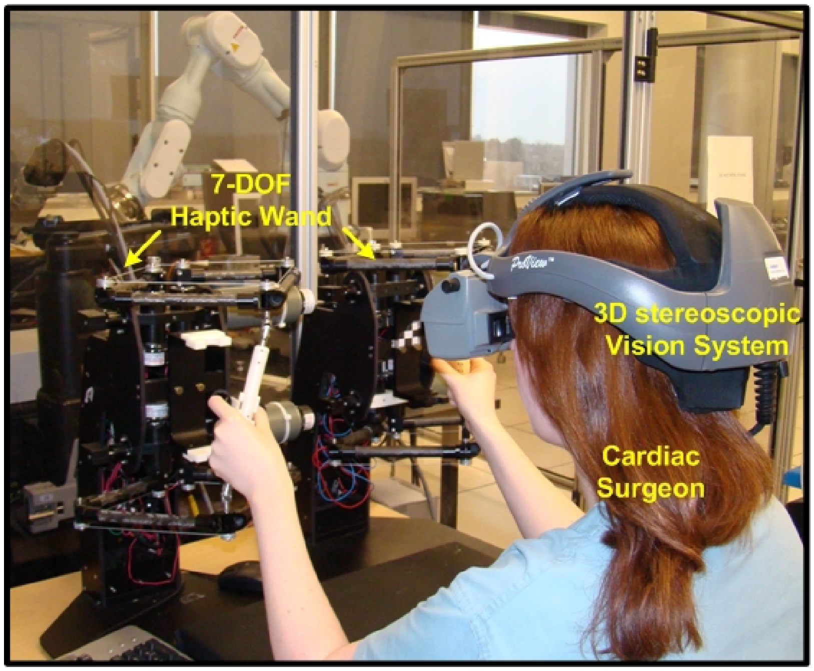

a) Haptic interfaces at the master side

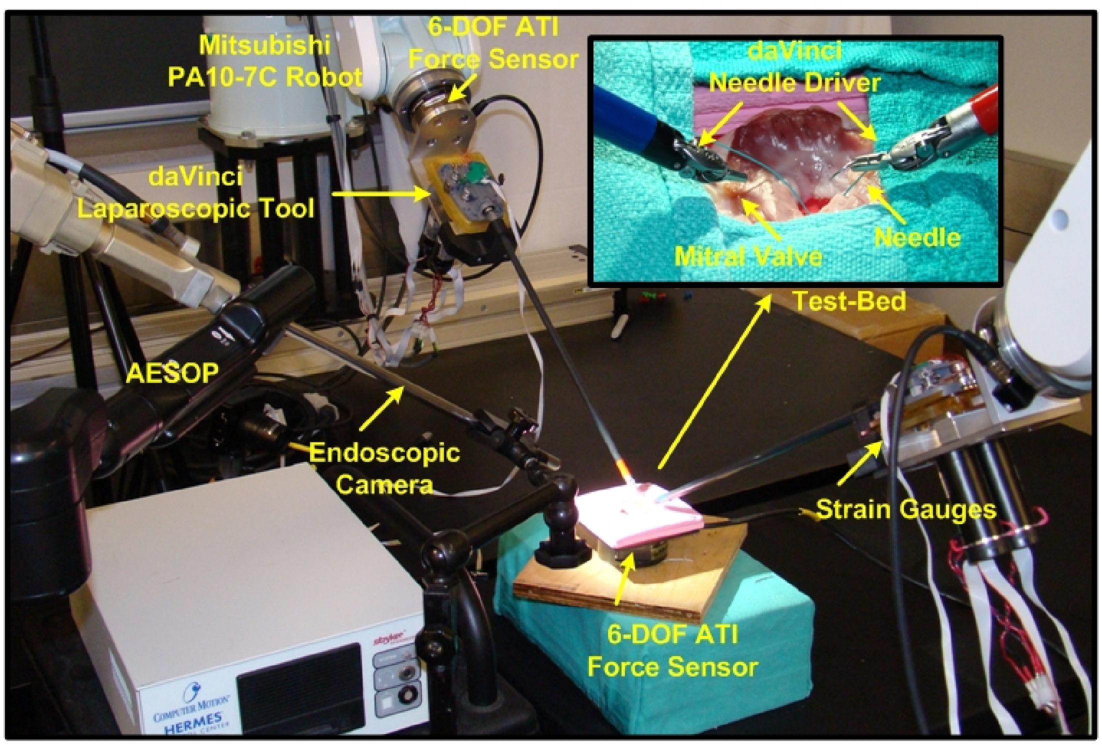

b) Surgical robots at the slave side

Figure 5.1: Experimental test-bed for suturing.

thread directly after looping, and tightening the knot. Details of the actions required for suturing are given in Table 5.1.

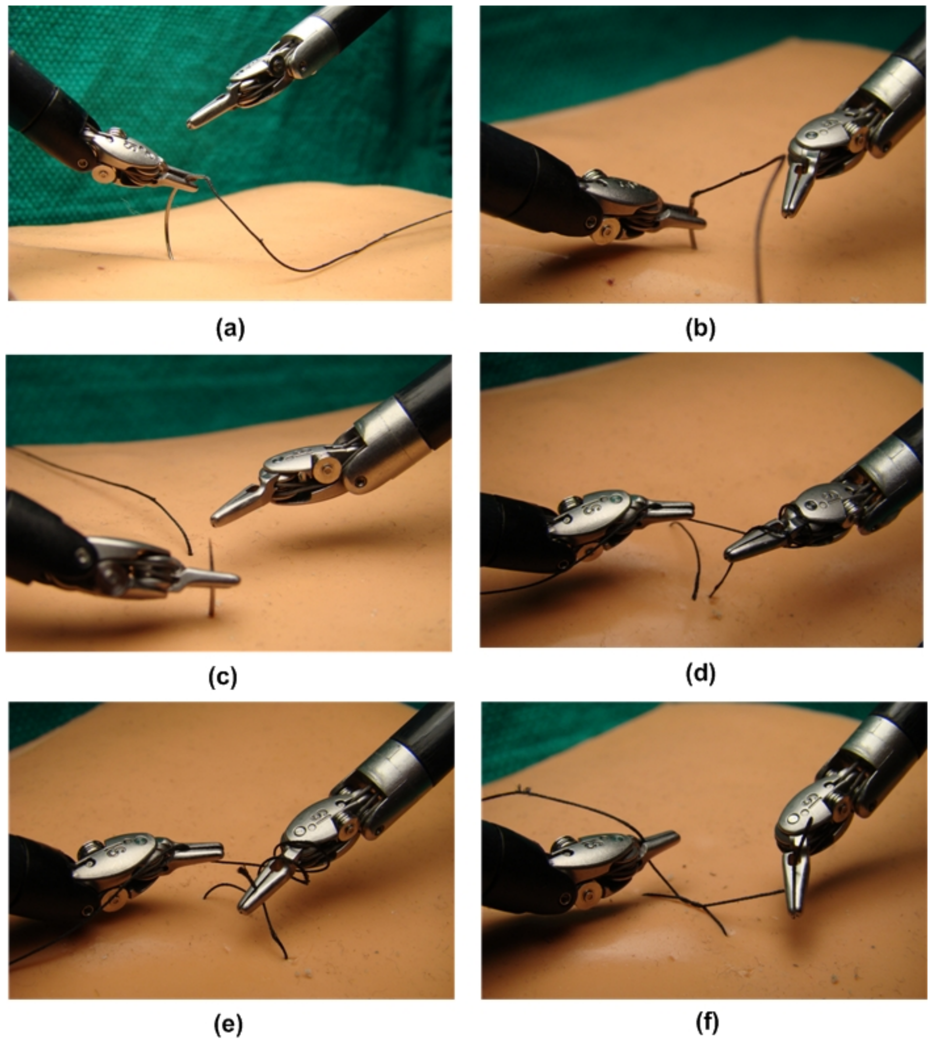

Figure 5.2: Sequences for performing a suturing task: (a) Grasping the needle and positioning it; (b) inserting the needle with penetration of the tissue; (c) pulling the needle through the tissue and passing it over; (d) looping the thread around one of the instruments; (e) grasping the thread directly after looping; (f) tightening the knot.

Fig. 5.3 also shows the sequences of a precise needle insertion into the tissue where point A is defined as the insertion point and point B is the desired exit point. First of all, the surgeon needs to bring the tip of the needle to point A and adjust the orientation of the needle such that the plane formed by points A, B, and C is perpendicular to the tissue plane. The next step is to move the needle in a circular arc such that it rotates in the direction shown in the picture.

Table 5.1: Description of the scored actions in the suturing task

Action	Definition
Stitching phase	
1- Grasping the needle	Grasping the needle before inserting it in the tissue.
2- Grasping the tissue	Grasping the tissue in order to position the needle before inserting it.
3- Positioning the needle	Moving the needle to insertion point A and adjusting the orientation of the needle such that the plane formed by the points A, B, and C is perpendicular to the tissue plane.
4- Inserting the needle	Inserting the needle with penetration into the tissue.
5- Grasping the needle tip	Grasping the tip of the needle in order to take it out of the tissue.
6- Pulling out the needle	Taking the needle out of the tissue.
7- Pulling through	Pulling the thread through the tissue.
Knot tying phase	
1- Grasping the thread	Grasping the thread by instrument 1 in order to loop it around instrument 2.
2- Looping the thread	Looping the thread around instrument 2.
3- Grasping the thread	Grasping the free end of the thread by instrument 2.
4- Pulling through	Pulling the loop over instrument 2 by instrument 1 and pulling the other end of the thread by instrument 2.
5- Tightening the knot	Tightening the knot by applying enough force to the two ends of the thread

In order for the needle to exit at point B, the needle position and orientation for the other DOFs should be kept unchanged. Once the tip of the needle comes out at point B, the same rotation is required to get the needle out of the tissue.

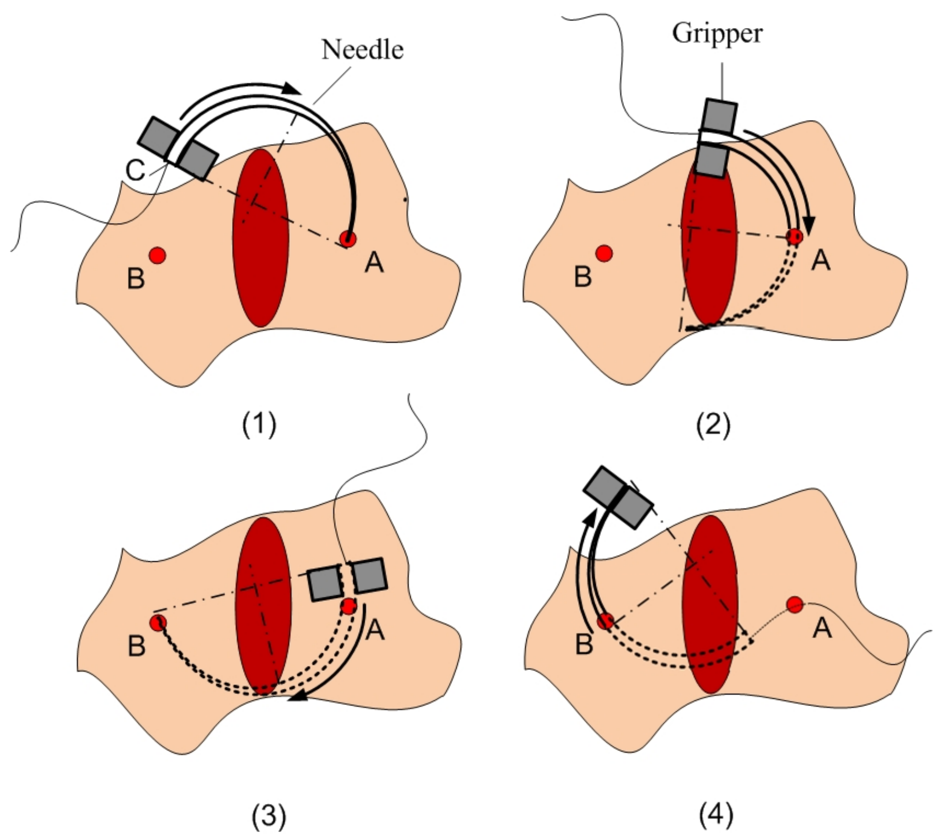

Figure 5.3: The required steps for a precise stitching, entering point A and exiting point B

Preliminary experiments show that incorporating force feedback in the last subtask in the knot tying phase can significantly improve its performance. Therefore, in this chapter, we focused on the effect of force feedback in both forms (haptics and sensory substitution) in the performance of knot tightening in RAMIS endoscopic suturing. Seven participants (4 males and 3 females) were asked to secure the second throw of surgical knots using our dual-arm teleoperation system (Fig. 5.4): one medical professional with previous experience with haptics, three subjects with some experience and three subjects with no experience with haptic feedback in teleoperated environments. Each subject was asked to tighten five knots with three different scenarios of sensory feedback on the interaction between the instrument and the tissue:

- No Force Feedback (NFF) where the subject only uses the camera vision to tighten the knots and does not receive any feedback of the contact between the instrument and its environment.
- Visual Force Feedback (VFF) in which the subject is given visual feedback about the level of interaction between the instrument and the environment in addition to the camera vision.
- Direct Force Feedback (DFF) where the force feedback of the interaction between the instrument and the environment is directly reflected to his/her hand in addition to the camera vision.

Three levels were considered for the visual feedback presented to the user. The main objective of showing force in different levels was to assure the user that the force being applied on the suture was sufficient to end up with a secure knot. The first level colored in green was the range of force/tension which is below the threshold required for a tight knot, the second level shown in yellow is the range sufficient for a tight knot and the last level (red) denotes the danger zone for force which may damage the tissue or break the suture if the applied force is within or beyond that range. Preliminary experiments showed that if the visualization of the force feedback is provided for each of the 7 DOFs individually, the subject would not be able to correlate the given visual feedback of the force with the motion of the haptic wand. However, the magnitude of the force feedback for each instrument informed the subject about the pulling force applied by each instrument on the suture.

The subjects were allowed to practice securing the knots using the dual-arm teleoperation system with the different control modes until they felt comfortable using the setup. Since the setup was sensorized in all 7-DOFs, they were able to approach the two ends of the knots from any desired position and with any desired orientation, grasp them tightly and pull on the suture. However, they were asked to apply forces symmetrically to ensure that the knot was secured and tightened. In the experiments, each subject performed 15 knot-tightening trials using three different modes; NFF, VFF, and DFF. The first trial for each mode was considered as a practice trial and was not included in the analysis. Therefore, 12 trials for each participant were considered for performance analysis (96 trials in total). Since the tightening force varies depending on the material of the suture, some preliminary experiments were

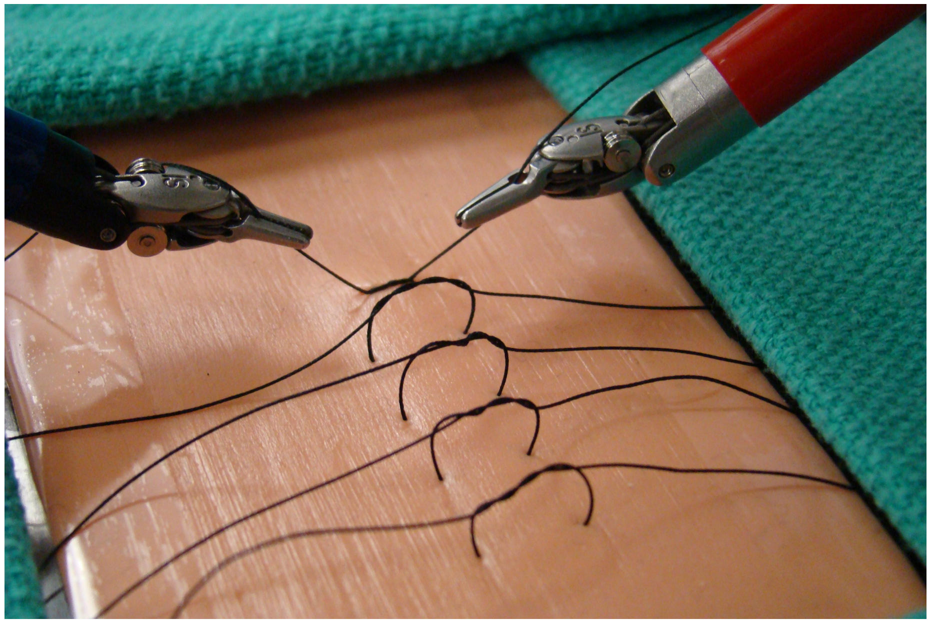

Figure 5.4: Experimental test-bed for tightening knots.

performed to determine the level of the forces that would be sufficient to have a secure knot. The sutures used in the experiments were Ethicon 3-0 silk. Artificial skins made from silicone rubber were selected as the tissues in our experiments. For the suture used, 4 N is sufficient to have a secure knot. If a subject applies forces greater than 6 N, he/she could damage the tissue or break the suture - this was set as the threshold of the red zone. In order to prevent sliding between the grippers and the suture when the subject tightens the suture knot, the grippers are commanded to maintain a 2 N grasping force with the grippers closed.

This study is aimed at addressing the following challenges: What method of presenting force feedback is more effective when securing suture knots and is more comfortable for the operator? Which method is better at improving the consistency of applied forces in a RAMIS endoscopic knot-tightening task? Is haptic feedback or visual sensory substitution better at improving the task completion time? Which method causes the least damage to the tissue? Does haptic feedback help the operator better control the laparoscopic instrument when performing the task? To answer to these questions, the performance of the participants was assessed for each mode of control according to the following criteria:

- The quality of the suture: Three situations may occur when performing a knot-tightening task: a loose knot, a broken knot or a tight knot. The tightened sutures were collected for assessment later by a medical professional.

- The amount of force applied on the suture when the knot is tightened: The force measurements along with the position profile of the instrument end effector were recorded to be used later for measuring the pulling force applied by each participant in the different control modes.

- The consistency of pulling forces: The subjects were asked to apply forces on the sutures consistently in each feedback mode. The consistency of the force applied by the participants for different scenarios was compared later using a one-way ANOVA test.

- The collision factor: This is a useful parameter to determine how much pressure the tissue was under when the laparoscopic instrument made contact with the tissue during the performance of the knot-tightening task. The collisions can be measured by integrating the negative force applied to the tissue in a direction perpendicular to the tissue surface - this force should always be upward if the instrument never touches the tissue. This force was measured by the ATI force sensor which was placed underneath the tissue.

- The number of hits between the instrument and the tissue: This parameter and the collision factor are the ones that evaluate the performance of the participants in controlling the instrument when performing a knot-tightening task. A contact force more than 1 N, acting perpendicularly to the tissue, was considered as a hit.

- Task completion time: The time required for completing the task by each participant was also recorded for each method.

- User friendliness: A written qualitative survey was completed by each participant to determine which method they felt more comfortable using.

For further analysis, a one-way ANOVA test with the Tukey test was conducted to determine if there is a significant difference for the assessment criteria among the trials performed with NFF, VFF, and DFF. A significance level of 0.05 was used for the one-way ANOVA analysis.

Table 5.2: Performance evaluation of tightening knots for each individual using different control modes.

Subject	No force feedback					Visual force feedback					Directly reflected force feedback				
	Time(s)	collision(Ns)	Quality			Time(s)	collision(Ns)	Quality			Time(s)	collision(Ns)	Quality		
			T	L	B			T	L	B			T	L	B
S1	127	6.72	3	1	0	110	4.83	4	0	0	107	5.60	4	0	0
S2	93	22.90	4	0	0	79	29.82	4	0	0	98	13.29	3	1	0
S3	87	46.22	3	0	1	137	39.98	4	0	0	96	6.65	4	0	0
S4	95	41.86	3	1	0	95	5.72	4	0	0	134	6.35	4	0	0
S5	137	18.48	4	0	0	134	6.57	4	0	0	120	10.52	3	1	0
S6	95	5.25	0	4	0	156	84.00	4	0	0	79	5.75	4	0	0
S7	79	3.37	3	1	0	106	10.84	4	0	0	87	1.89	4	0	0

Table 5.3: Performance evaluation of the tightening forces for each individual using different control modes.

Subject	No force feedback			Visual force feedback			Directly reflected force feedback		
	F_{pull}(N)	F_{avg}(N)	F_{max}(N)	F_{pull}(N)	F_{avg}(N)	F_{max}(N)	F_{pull}(N)	F_{avg}(N)	F_{max}(N)
S1	1.12±0.36	1.22	1.53	4.59±0.81	3.18	5.22	2.63±0.62	1.89	3.32
S2	3.71±0.96	2.21	5.05	4.66±0.38	2.47	5.09	0.94±0.39	1.28	2.66
S3	3.99±1.71	2.69	6.58	4.54±0.19	2.43	5.69	5.03±0.15	3.28	5.25
S4	1.30±1.16	1.58	2.89	4.72±0.39	3.27	5.26	1.77±1.16	1.57	3.60
S5	3.00±0.53	1.89	3.87	3.82±0.63	2.44	4.40	0.87±0.33	1.20	1.42
S6	0.32±0.14	1.85	2.66	4.07±0.84	2.33	5.05	1.36±0.26	1.28	1.72
S7	1.35±0.50	1.28	2.00	4.08±0.40	2.50	4.66	0.90±0.23	1.08	1.23

Table 5.4: Performance evaluation of the motion control over the tissue during tightening knots for each individual using different control modes.

	No force feedback				Visual force feedback				Directly reflected force feedback			
Subject	F_{avg}(N)	F_{max}(N)	collision (Ns)	Hits (no)	F_{avg}(N)	F_{max}(N)	collision (Ns)	Hits (no)	F_{avg}(N)	F_{max}(N)	collision (Ns)	Hits (no)
S1	0.68	1.36	6.72	1	0.56	0.67	4.83	0	0.69	0.95	5.60	0
S2	1.32	2.70	22.90	5	1.34	3.23	29.82	6	0.58	1.26	13.29	1
S3	1.49	5.80	46.22	5	1.33	5.03	39.98	8	0.82	2.12	6.65	2
S4	1.15	2.40	41.86	5	0.56	0.69	5.72	0	0.80	1.66	6.35	1
S5	0.99	2.57	18.48	2	0.84	1.94	6.57	4	0.60	0.88	10.52	0
S6	1.24	2.69	5.25	2	1.64	3.65	84.00	10	0.20	0.47	5.75	0
S7	0.62	0.94	3.37	0	0.97	2.07	10.84	6	0.65	0.80	1.89	0

5.1 Results

Tables 5.2-5.4 show the collected data from seven subjects participated in the knot-tightening task study for the three feedback modes: no force feedback (NFF), visual force feedback (VFF), and direct force feedback (DFF).

Figs. 5.5-5.9 also show the results in the bar graph. The quality of the knots tightened by the subjects is presented in Fig. 5.5. The results show that without any feedback from the force being applied by the operators on the suture, seven knots were loose and one suture was broken. Having force feedback on the subject's hand when performing the task ended up with two loose knots and with visual force feedback all suture knots were sufficiently tightened without any loose or broken sutures.

Fig. 5.6 shows the average tightening force applied on the suture and its standard

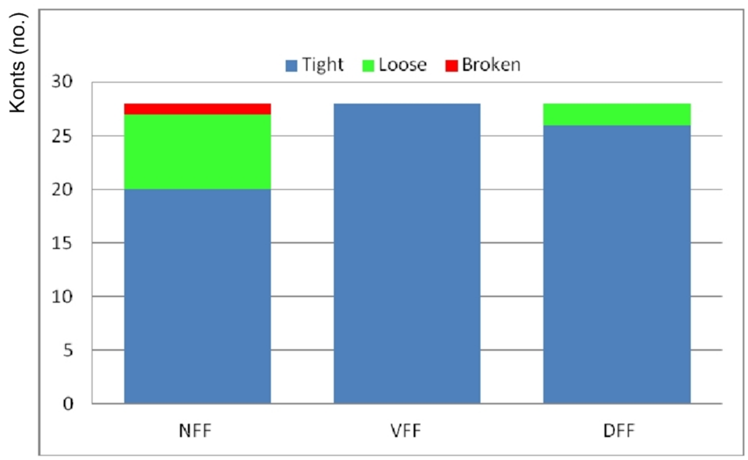

Figure 5.5: Quality of the knots.

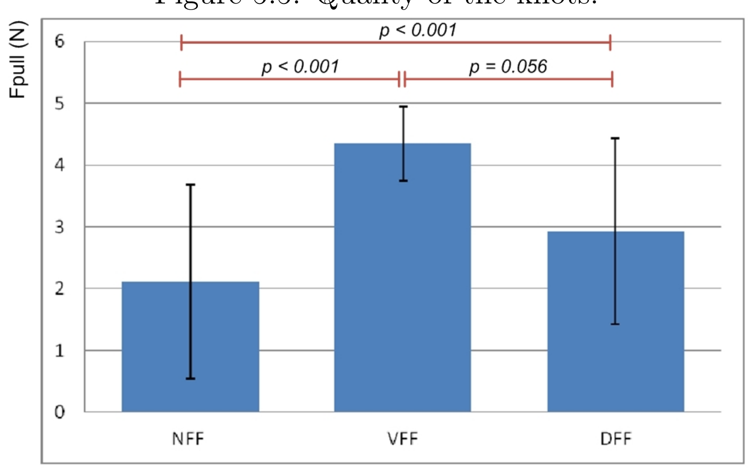

Figure 5.6: Tightening force applied on the sutures in the three scenarios.

deviation for the different scenarios. The results show that the subjects pulled on the suture with 2.11 N, 4.35 N and 2.93 N on average for NFF, VFF, and DFF, respectively. The force applied using visual force feedback was the most consistent one among those three methods. The results achieved from an ANOVA analysis (Table 5.5) show a significant difference for the VFF method compared to the NFF and DFF method ($p < 0.001$ for both VFF-NFF, and VFF-DFF).

Fig. 5.7 presents the amount of pressure suffered by the tissue because of collisions between the instrument and the tissue. The results show that the participants had the minimum collision with the tissue when they felt the interaction forces on their hands. An ANOVA test reveals that a significant difference occurred in the collision for the DFF feedback mode compared to the NFF and VFF ($p = 0.021$ for DFF-NFF and $p = 0.001$ for DFF-VFF). Fig. 5.8 also shows the DFF mode had the minimum

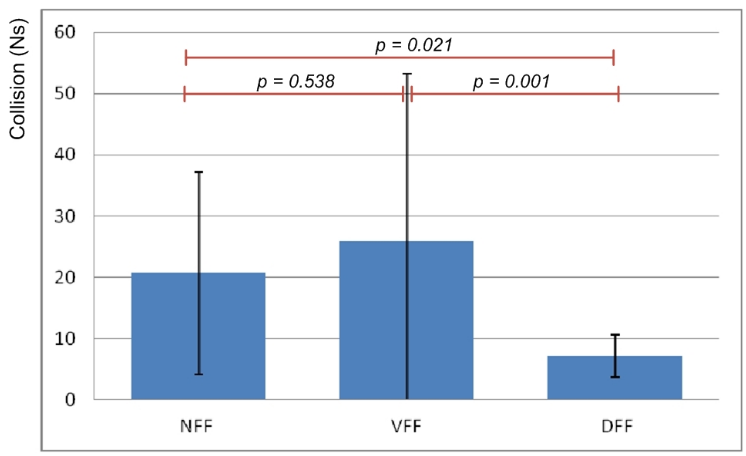

Figure 5.7: Collision factor in the three scenarios.

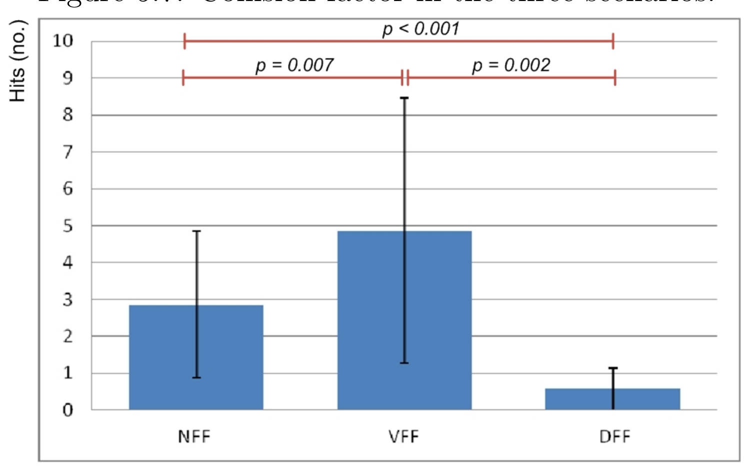

Figure 5.8: Number of hits on the tissue in the three scenarios.

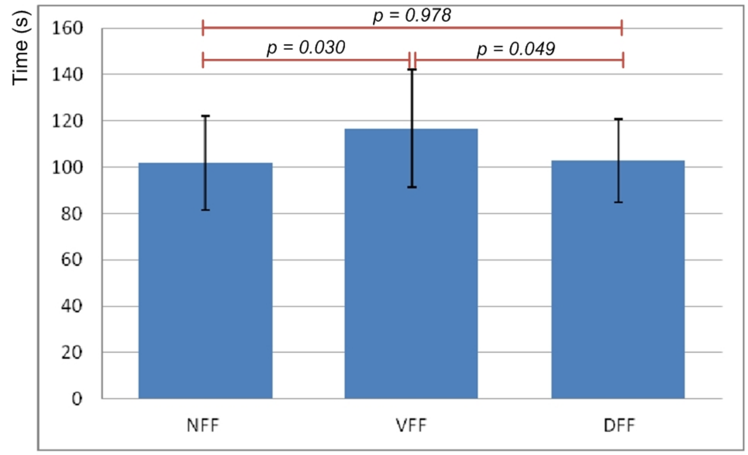

Figure 5.9: Task completion time in the three scenarios.

number of hits with the tissue when performing knot-tightening task ($p = 0.002$ for DFF-NFF and $p < 0.001$ for DFF-VFF).

Fig. 5.9 shows the time required to accomplish task for each method. An ANOVA test shows a significant difference for the VFF method compared to the NFF and DFF methods ($p = 0.030$ for VFF-NFF and $p = 0.049$ for VFF-DFF). No significant difference in task completion time was seen for the DFF method compared to the NFF method ($p = 0.978$).

5.2 Discussion

As mentioned earlier, the performance evaluation criteria included the quality of the knot, the amount of tightening force applied on the suture and its consistency among participants, the user controllability over the instrument, tissue damage, task completion time, and user friendliness.

The results confirm that if the amount of tightening force is given to the subject in a visual form, he/she can ensure that sufficient force is applied in order to secure the knot. Having haptic feedback reflected to the subject's hand can also decrease the number of loose or broken sutures compared to when the subject has no feedback from the interaction of the instrument with the suture. However, as the results showed, since the subjects did not know how much force was sufficient to tighten the knots, each applied a different amount of force which ended up with two loose knots. Fig. 5.6 and Table 5.5 also confirm that the consistency of applied forces during the robot-assisted knot-tightening task with sensory substitution was significantly greater than that achieved with no force feedback or direct force feedback. Although both DFF and NFF showed significant variation in the applied tightening force by different subjects, the main advantage of the DFF method over the NFF method is that it allows forces to be felt directly on the hand, which decreases the number of loose or broken sutures.

Despite the advantages of sensory substitution (VFF) over haptics (DFF) from the point of view of suture knot quality and tightening force consistency, Figs. 5.7 and 5.8 and Table 5.5 demonstrate poor performance in the visual force feedback scenario and superior performance in the haptics scenario with regards to the user's control of the instrument. The results show that both NFF and VFF were unable to help the participants control the instrument effectively and the instrument hit the tissue several times during the performance of the knot-tightening task. The statistical analysis shows that the factor denoting the amount of collision using DFF was significantly lower than that using NFF and VFF. This can be justified by the 7-DOF force reflection capability provided through the master-slave teleoperation system to the participant's hand which gives him/her a more intuitive feel to effectively perform a RAMIS task. Visually representing the magnitude of the interaction force between the instrument and its environment cannot give subjects an intuitive feel about where and in which DOF this force is being applied. On the other hand, providing force visualization for each DOF is also distracting to the user and difficult for him/her to decide how to modify the forces applied to the tissue. The other source of error that created poor performance in the VFF scenario was that when the operator attempted

Table 5.5: Multiple comparisons between the different scenarios.

ANOVA		Significance (p value)			
(I)	(J)	Pulling force	Collision Factor	No. of hits	Time
NFF	VFF	.000	.538	.007	.030
	DFF	.056	.021	.002	.978
VFF	NFF	.000	.538	.007	.030
	DFF	.000	.001	.000	.049
DFF	NFF	.056	.021	.002	.978
	VFF	.000	.001	.000	.049

to grasp one end of the suture using one instrument, he/she lost focus of what the other instrument was doing which caused the instrument to collide with the tissue.

With respect to task completion time, the results show that not only was there no improvement using haptics or sensory substitution, but the latter also caused the task to take longer. This is reasonable because of the additional time needed by the participants to ensure that the tightening force was in the yellow zone.

After finishing the experiments, each participant was asked to choose the method that he/she was more comfortable with. Almost all participants agreed that having both visual and haptic feedback is helpful. However, the novice participants preferred to have visual feedback from the interaction forces since they could get a better measure of how much force they were applying on the suture. Those who had some experience with haptics preferred direct force reflection on their hands and found it difficult to control the instrument without haptic feedback.

All the aforementioned results show that neither sensory substitution alone nor haptics alone can significantly improve the performance of the knot-tightening task in robotics-assisted minimally invasive surgery. Sensory substitution has superior performance in the quality of suture knots with high consistency of the tightening force because the user knows how much force he/she needs to apply to secure the knots. Haptics can significantly improve the performance of suture-manipulation because of the intuitive feel provided to the user through the haptic interface. This study shows that visual presentation of the magnitude of the interaction force needs to be incorporated with a haptics-enabled teleoperated system to let the user know how much force is required to secure the knot.

Chapter 6

Conclusion and Future Work

This chapter summarizes the key contributions of the thesis and then provides some suggestions for future work on the topic of the thesis.

6.1 Conclusions

This thesis focused on the problem of incorporating haptics in robotics-assisted minimally invasive surgery in the form of single- and dual-arm master-slave teleoperated systems. The dual arm master-slave teleoperation testbed developed in this project consisted of two Mitsubishi PA10-7C robots as the slave system that was remotely controlled (over a dedicated network) through two 7-DOF Haptic Wands. Chapter 2 described the hardware modifications which were carried out to equip the testbed in order to measure tool-tissue interaction in 7-DOFs and to fully reflect them to the master side. The original Haptic Wand was found to have limited applicability in MIS due to the lack of force reflection in the yaw direction and for grasping (the original Haptic Wand provided by Quanser is only capable of force reflection in 5-DOF). Thus, it was required to modify the device to include force reflection in those DOFs. At the slave side, two types of laparoscopic instruments were used as the end effector of the Mitsubishi PA10 robots: Two da Vinci needle drivers that were used for the suturing application, and a customized instrument the Tactile Sensing Instrument, which is a palpation probe incorporated with an array of tactile sensors and used for tumor localization in RAMIS via soft-tissue palpation. In order to measure the interaction of these instruments with their environments, we used an external ATI force sensor mounted between the instrument and the Mitsubishi PA10-7C robot and developed calibration software in MATLAB® to compensate for the effect of gravity as the instrument moves. However, to fully measure the interaction for the da Vinci instrument with tissue, several strain gauges were embedded inside the tool to measure the forces/torques applied to the tip of the instrument. The control system for the setup was implemented in two Windows-based systems, one at the master side and the other at the slave side. The communication between the computers was done using the UDP protocol. All control algorithms were implemented on the QuaRC Real-Time software, which automatically generates real-time code directly from Simulink-designed controllers implemented at a sampling frequency of 1 kHz.

Chapter 3 described the software modification that was done for the dual-arm teleoperation system. To effectively implement the control algorithms and to have a fully transparent teleoperation system, the kinematics and dynamics of the master and slave manipulators needed to be modeled. Kinematics of the da Vinci needle drivers were extracted in this chapter and verified through experiment. The kinematic and dynamic modeling problems for the 7-DOF Haptic Wand were also addressed in this chapter. A closed-form kinematic model including forward kinematics, inverse kinematics and the Jacobian were developed and verified for the 7-DOF Haptic Wand. The dynamic equations of the Haptic Wand were derived using the Lagrangian approach. An experimental friction analysis for the Haptic Wand was also presented in this chapter. Then, both kinematics and dynamics of the Haptic Wand were verified by an end-effector trajectory tracking experiment. A two-channel bilateral control architecture was chosen to transmit data from one side of the teleoperation system to the other side. In this architecture, the position command imposed by the operator was fed forward from the master as the input to the slave, and the interaction force between the remote slave robot and its environment was fed back as the input to the master. To reflect force feedback to the master side, the impedance control technique was chosen for the haptic wand. Using the dynamic model developed in this project, the inherent impedance of the mechanism was first compensated and then a desired impedance, based on the required MIS application, was given to the Haptic Wand along with the tool-tissue force interaction reflected to the operator's hand. Due to the lack of force sensing at the master side, a high-gain force observer was designed to measure the interaction force between the operator's hand and the handle of the Haptic Wand. For the slave manipulator, a hybrid impedance controller was designed to enable switching between position-controlled and force-controlled subspaces in different DOFs based on what was required for the MIS task. In order to pivot the instrument about the entry port in an MIS training box, representing the patient's body, a software-based remote center of motion was generated at the slave side.

The problem of incorporating tactile sensing with force feedback was explored for minimally invasive tumor localization for liver and lung cancer in Chapter 4. In this work, the Tactile Sensing Instrument (TSI) was used to remotely palpate tissue through the single-arm master-slave teleoperation system. In this study, first the performance of each individual method for tumor localization was investigated; then force feedback was incorporated with tactile feedback to see how effectively it could reduce the limitations of tactile sensing for tumor localization. It was shown that the results of the TSI-based palpation are highly dependent on the consistency of the exploration force. For liver cancer, two scenarios were presented to incorporate force feedback with tactile feedback: visual presentation of the force on a screen and direct reflection of the force on the operator's hand. Eight participants were asked to locate the artificial tumors embedded in the liver. The results showed that using the TSI in a force-controlled environment could realize on average 57% decrease in the maximum force and 55% decrease in the average force applied on the tissue while increasing the tumor detection accuracy by up to 50% compared to the case of using tactile feedback alone. The results also showed better performance of visual force feedback compared to direct force reflection; getting visual force feedback from the interaction between the TSI and tissue could better help the operator control forces in the specified ranges and to ensure that enough exploration force was applied on the tissue while keeping the tissue away from any damage. In order to see the effect of haptics in tumor localization in the case of lung cancer, new tactile-force integrated feedback was proposed. In this method, the operator would be able to palpate lung tissue by sliding the TSI over the tissue without any concern about controlling exploration force in the palpation direction. The hybrid impedance control method proposed for this application enabled the operator to switch between position-controlled and force-controlled subspaces and thereby automatically adjust the exploration force at a level predetermined by the operator. Using the proposed method, the operator would be able to palpate the tissue consistently, observe the pressure distribution over the tissue by a color contour map on a screen and feel the tumor on his/her fingers through a grasping mechanism of the haptic interface as a result of higher stiffness of the tumor. The tissue used for the experiments was *ex vivo* bovine lung and seven participants were asked to locate artificial tumors embedded in the lungs. The results showed an accuracy of 93% in tumor localization using the proposed method while the average force applied to the tissue was $3.42N$ and the force never exceeded $6N$.

Chapter 5 was aimed at exploring the effect of force feedback on the performance of endoscopic suturing in RAMIS. In this work, we evaluated the performance of subjects during a knot-tightening task in three modes: without force feedback, with visual force feedback and with direct force reflection on the subjects' hands. Three levels were considered for the visual feedback presented to the user. The main objective of showing force in different levels was to assure the user that the force being applied on the suture was sufficient to end up with a secure knot. The first level colored in green denoted the range of force/tension below the threshold required for a tight knot, the second level shown in yellow denoted the range that was sufficient for a tight knot and the last level (red) denoted the force/tension which could damage the tissue or break the suture. Different performance measures were implemented: the quality of the knot, the amount of tightening force applied on the suture and its consistency, user controllability over the instrument, tissue damage, task completion time, and user friendliness. The main focus of this work was to investigate how force feedback should be presented to make it more effective, and how each modality could help the user to improve his/her performance. Seven subjects participated in this study and were asked to tighten the second throw of surgical knots using the dual-arm teleoperation system. The results showed that visual force feedback allowed superior performance in the quality of the suture knots with high consistency in the tightening force, while direct force feedback could significantly improve the user's control over the instrument.

6.2 Recommendations for Future Work

There are several directions in which this research can be continued in the future. Some suggestions are as follows:

1. The master-slave teleoperation system developed in this project is a research platform aimed at exploring the effect of haptics in robotics-assisted minimally invasive telesurgical scenarios. This setup has some limitations that do not allow it to be used for in-vivo trials or clinical application. In order to implement the

proposed approaches in this thesis for in-vivo telesurgical scenarios, a number of issues would need to be resolved for the setup:

(a) The first and most significant issue is the need for a force sensor that can be inserted into the patient's body and can directly measure the interaction forces between the tip of the instrument and tissue. As part of the sensory system in our dual-arm teleoperation setup, two ATI Gamma force sensors were used and mounted between the wrist of the Mitsubishi PA10-7C robots and the laparoscopic instruments. These externally mounted force sensors measure not only the interaction between the tip of the laparoscopic instrument and tissue but also the friction between the tool and the trocar. The other source of error in the force measurements is the weight of the laparoscopic instruments attached to the externally mounted force sensor. Although the gravity effect of the laparoscopic tools has been compensated through software, the dynamics effect of the tools can create some inaccuracies in the tip force measurements when the robots are in motion.

(b) In order to pivot the instrument at entry point, a virtual RCM was maintained in this research. However, designing a mechanical structure for maintaining the RCM would be preferable in clinical applications because of the rigidity and reliably that it brings by avoiding the effect of possible controller faults.

(c) The PA10-7C robots used in our dual-arm teleoperation system are industrial manipulators developed by Mitsubishi Heavy Industries Ltd. for robotic R&D and general industrial use which of course are not suitable for use as surgical robots because of patient safety issues.

(d) At the other end of the teleoperation system, the master side, the limit on the magnetite of continuous force reflection for the Haptic Wands prevented us from using a one-to-one mapping for the reflection of the interaction force measured at the slave side to the master side (the maximum continuous force reflection providing by the motors of the Haptic Wand is 3 N in the z-direction in its world frame).

(e) The mechanical design structure of the Haptic Wands provided a limited range of motions for orientation. For some applications such as suturing, surgeons need a larger workspace for orientation. To resolve this issue, we used a 1-to-2 mapping for the orientation from the Haptic Wand to that of the PA10 end effector which caused the master-slave teleoperation system to be less intuitive.

2. Being able to perform telesurgery using a RAMIS system over long distances has been of interest for the medical community around the world, particularly in Canada. One of the challenging issues for master-slave teleoperation systems for use in MIS is communication latency in transmission of the data. It has been shown that if the communication latency between the command sent by the remote surgeon and the signal received by the surgical robots in the operating room exceeds a certain amount, it can cause some difficulties. Time delays in teleoperation can reduce efficiency by requiring the user to slow down on each movement and, in the worst case scenario, cause instability in the teleoperated system. For a haptics-enabled robotics-assisted telesurgical system, time delay can also affect the transparency of the master-slave teleoperation and change the "feel" of interaction between the laparoscopic instrument and the tissue. In general, compensation techniques against the destabilizing effect of time delays in teleoperation systems can be classified into three main groups: Predictive displays, supervisory control, and passivity-based approach. Predictive displays need an adaptable model of the remote platform which is computationally expensive and might not be available for an unstructured and unknown environment. Supervisory control can also be effective for applications with sufficiently predictable characteristics which is not generally the case for telesurgery due to the unpredictable nature of interactions with tissue. However, the passivity-based approach has been theoretically proven to be capable of stabilizing teleoperation systems with any time delay. This method links the observed instability of the delayed teleoperation system to power generation in an equivalent two-port network and employs scattering theory to stabilize the system. However, it has some restrictions in practice which needs further considerations. Proposing a successful time-delay compensation technique is another research area which can address the problem of stabilization of the overall closed-loop teleoperation system in the presence of communication latency while providing the improved transparency.

3. Although proposing an appropriate time-delay compensation method can make robotics-assisted telesurgery feasible over remote distances, it has been shown in the literature that if the time delay exceeds a certain threshold value, depending on the MIS task, telesurgery will not be feasible anymore. However,

for some non-surgical tasks such as tumor localization, the effect of latency in remote teleoperation may not pose a major obstacle. A combination of time-delay compensation, haptics and visual representation of force reflection could still be useful. A project based on the existing teleoperation testbed with the introduction of time delays between the master and the slave in a palpation task is planned in the near future.

4. In both telesurgical applications in this research project, surgeons performed the RAMIS task on soft-tissue using the dual-arm master-slave teleoperation system. However, for some telesurgery scenarios such as orthopedic applications where the surgeon performs procedures that deal with both soft tissue and bones, special consideration should be taken to stabilize the haptics-enabled teleoperation system in the presence of hard contact. Different control approaches would be required for such interactions.

5. The comprehensive study on the effect of force feedback on tactile sensing tumor localization showed that the best performance was achieved using the semi-autonomous method proposed for tumor localization in the lung. In this method, the operator palpates the tissue consistently, observes the pressure distribution over the tissue by a color contour map on a screen and feels the tumor on his/her fingers through a grasping mechanism of the haptic interface as a result of higher stiffness of the tumor. The force felt by the operator through the grasping mechanism in this project was the force measured by the middle elements of the TSI. If the palpated tumor is not in that area, the operator would not feel it by direct force feedback. A modification of this work could be to design a stimulator composing of four separately actuated pads. By attaching these pads to the pinch lever (grasping mechanism on the Haptic Wand), we would be able to feel the amount of pressure applied on different regions of the TSI and thereby achieve better detection over the region where the tumor exists.

6. The haptics-enabled master-slave teleoperation system developed in this project has the potential to be used for other telesurgery scenarios in order to explore the effect of haptics for those applications. As an example, we can mention to robotics-assisted mitral valve repair. There is an ongoing project at CSTAR that is investigating the use of force feedback in the performance of certain cardiac procedures such as minimally invasive mitral valve repair. This work is using our dual-arm teleoperation setup. In this application, sixteen 20 cm 2-0

Ethibond sutures will be passed through the porcine mitral valve annulus at predetermined marked points. The subjects of this study are cardiac surgeons and residents who will execute a series of knots using the dual-arm teleoperation system. This study is aimed at addressing the following challenges: Which method of presenting force feedback is more effective when suturing on mitral valve and is more comfortable for the surgeon? Which method provides better consistency of applied forces in this task? Is haptic feedback or visual sensory substitution better at reducing the task completion time? Which method causes the least damage to the tissue? Does haptic feedback help the operator better control the laparoscopic instrument when performing the task?

7. Haptics for surgical training and skills assessment: The dual-arm teleoperation setup developed in this project can provide novice surgeons the opportunity to practice surgical procedures where they have stereoscopic vision as well as haptic feedback. This haptics-enabled master-slave setup can help trainees to learn how to do a task in a telesurgical mode. It can help them to gain an objective kinesthetic understanding of the task by reflecting the interaction force on their hands. Using force feedback for training in MIS can help novice surgeons to avoid applying excessive force when performing surgery in a master-slave setting. One area of research is to study the effect of haptic feedback on trainees' learning curves for different telesurgical scenarios when force information is presented as direct reflection and via sensory substitution.

Bibliography

[1] A. L. Trejos and R. V. Patel, "A sensorized instrument for skills assessment and training in minimally invasive surgery," *Journal od Medical Devices*, vol. 3, no. 4, 041002 (12 pages), 2009.

[2] R. H. Taylor, "A perspective on medical robotics," *Proceedings of the IEEE*, vol. 94, no. 9, pp. 1652–1664, 2006.

[3] http://www.intuitivesurgical.com.

[4] A. M. Okamura, L. N. Verner, C. E. Reiley, and M. Mahvash, "Haptics for robot-assisted minimally invasive surgery," in *13th International Symposium on Robotics Research*, pp. 102–107, 2007.

[5] J. J. Abbott, *Virtual Fixtures for Bilateral Telemanipulation*. PhD thesis, The Johns Hopkins University, 2005.

[6] T. Akinbiyi, C. E. Reiley, S. Saha, D. Burschka, C. J. Hasser, D. D. Yuh, and A. M. Okamura, "Dynamic augmented reality for sensory substitution in robot-assisted surgical systems," in *Proceeding of the IEEE Engineering in Medicine and Biology Society*, pp. 567–570, 2006.

[7] M. Tavakoli, *Haptic Interaction in Master-Slave Minimally Invasive Robotic Surgery*. PhD thesis, The University of Western Ontario, 2007.

[8] L. N. Verner, *Sensor/Actuator Asymmetries in Telemanipulators*. PhD thesis, The Johns Hopkins University, 2009.

[9] S. Saha, "Appropriate degrees of freedom of force sensing in robot-assisted minimally invasive surgery," Master's thesis, The Johns Hopkins University, 2005.

[10] J. P. Ruurda, I. A. M. J. Broeders, B. Pulles, F. M. Kappelhof, and C. van der Werken, "Manual robot assisted endoscopic suturing: time action analysis in an experimental model," *Surgical endoscopy*, vol. 18, no. 8, pp. 1249–1252, 2004.

[11] A. K. Morimoto, R. D. Foral, J. L. Kuhlman, K. A. Zucker, M. J. Curet, T. Bocklage, T. I. MacFarlane, and L. Kory, "Force sensor for laparoscopic babcock," *Studies in Health Technology and Informatics*, vol. 39, pp. 354–361, 1997.

[12] T. Ortmaier, B. Deml, B. Kubler, G. Passig, D. Reintsema, and U. Seibold, "Robot assisted force feedback surgery," *Advances in telerobotics, Springer Tracts in Advanced Robotics*, vol. 31, pp. 361–379, 2007.

[13] B. Demi, T. Ortmaier, and U. Seibold, "The touch and feel in minimally invasive surgery," in *IEEE International Workshop on Haptic Audio Visual Environments and their Applications*, pp. 33–38, 2005.

[14] C. R. Wagner and R. D. Howe, "Force feedback benefit depends on experience in multiple degree of freedom robotic surgery task," *IEEE Transaction on Robotics*, vol. 23, no. 6, pp. 1235–1240, 2007.

[15] C. R. Wagner, N. Stylopoulos, P. G. Jackson, and R. D. Howe, "The benefit of force feedback in surgery: Examination of blunt dissection," *Presence: Teleoperators and Virtual Environments*, vol. 16, no. 3, pp. 252–262, 2007.

[16] A. Kazi, "Operator performance in surgical telemanipulation," *Presence: Teleoperators and Virtual Environments*, vol. 10, no. 5, pp. 495–510, 2001.

[17] C. E. Reiley, T. Akinbiyi, D. Burschka, D. C. Chang, A. M. Okamura, and D. D. Yuh, "Effects of visual force feedback on robot-assisted surgical task performance," *Journal of Thoracic and Cardiovascular Surgery*, vol. 135, pp. 196–202, 2008.

[18] C. G. L. Cao, M. Zhou, D. B. Jones, and S. D. Schwaitzberg, "Can surgeons think and operate with haptics at the same time?," *Journal of Gastrointest Surgery*, vol. 11, pp. 1564–1569, 2007.

[19] G. Tholey, J. P. Desai, and A. E. Castellanos, "Force feedback plays a significant role in minimally invasive surgery: results and analysis," *Annals of Surgery*, vol. 241, no. 1, pp. 102–109, 2005.

[20] C. Aschwanden, A. Sherstyuk, L. Burgess, and K. Montgomery, "A surgical and fine-motor skills trainer for everyone? touch and force-feedback in a virtual reality environment for surgical training," *Studies in Health Technology and Informatics*, vol. 119, pp. 19–21, 2005.

[21] H. Maass, B. B. Chantier, H. K. Cakmak, C. Trantakis, and U. G. Kuehnapfel, "Fundamentals of force feedback and application to a surgery simulator," *Computer Aided Surgery*, vol. 8, pp. 283–291, 2003.

[22] W. Chou and T. Wang, "Human-computer interactive simulation for the training of minimally invasive neurosurgery," in *IEEE International Conference on Systems, Man and Cybernetics*, pp. 1110–1115, 2003.

[23] H. Wu, C. Hourie, R. Eagleson, and R. V. Patel, "A haptics based simulator for laparoscopic pyeloplasty," *Studies in Health Technology and Informatics*, vol. 119, pp. 583–585, 2006.

[24] T. N. Judkins, D. Oleynikov, and N. Stergiou, "Real-time augmented feedback benefits robotic laparoscopic training," *Studies in Health Technology and Informatics*, vol. 119, pp. 243–248, 2006.

[25] E. P. Westebring, V. D. Putten, R. H. M. Goossens, J. J. Jakimowicz, and J. Dankelman, "Haptics in minimally invasive surgery - a review," *Minimally Invasive Therapy*, vol. 17, no. 1, pp. 3–16, 2008.

[26] A. M. Okamura, "Haptic feedback in robot-assisted minimally invasive surgery," *Current opinion in urology*, vol. 19, no. 1, pp. 102–107, 2009.

[27] A. L. Trejos, R. V. Patel, and M. D. Naish, "Force sensing and its applications in minimally invasive surgery and therapy: A survey," *Proceedings of the Institution of Mechanical Engineers, Part C: Journal of Mechanical Engineering Science*, vol. 224, pp. 1435–1454, 2010.

[28] B. Kuebler, U. Seibold, and G. Hirzinger, "Development of actuated and sensor integrated forceps for minimally invasive robotic surgery," *The International Journal of Medical Robotics and Computer Assisted Surgery*, vol. 1, no. 3, pp. 96–107, 2005.

[29] M. E. H. Eltaib and J. R. Hewit, "Tactile sensing technology for minimal access surgery: a review," *Mechatronics*, vol. 13, pp. 1163–1177, 2003.

[30] J. Dargahi, "An integrated force position tactile sensor for improving diagnostic and therapeutic endoscopic surgery," *Bio-Medical Materials and Engineering*, vol. 14, no. 2, pp. 151–166, 2004.

[31] A. Bicchi, G. Canepa, D. D. Rossi, P. Iacconit, and E. P. Scilingo, "A sensor-based minimally invasive surgery tool for detecting tissue elastic properties," in *IEEE International Conference on Robotics and Automation*, pp. 884–888, 1996.

[32] P. J. Berkelman, L. L. Whitcomb, R. H. Taylor, and P. Jensen, "A miniature microsurgical instrument tip force sensor for enhanced force feedback during robot-assisted manipulation," *IEEE Transactions on Robotics and Automation*, vol. 19, no. 5, pp. 917–922, 2003.

[33] J. Rosen and B. Hannaford, "Markov modeling of minimally invasive surgery based on tool/tissue interaction and force/torque signatures for evaluating surgical skills," *IEEE Transactions on Biomedical Engineering*, vol. 48, no. 5, pp. 579–591, 2001.

[34] M. V. Ottermo, M. Vstedal, T. Lang, Stavdahl, Y. Yavuz, T. Johansen, and R. Marvik, "The role of tactile feedback in laparoscopic surgery," *Surgical Laparoscopy Endoscopy and Percutaneous Techniques*, vol. 16, no. 6, pp. 390–400, 2006.

[35] D. T. V. Pawluk, J. S. Son, P. S. Wellman, W. J. Peine, and R. D. Howe, "A distributed pressure sensor for biomechanical measurements," *ASME Journal of Biomechanical Engineering*, vol. 102, no. 2, pp. 302–305, 1998.

[36] R. D. Howe, W. J. Peine, D. A. Kontarinis, and J. S. Son, "Remote palpation technology for surgical applications," *Engineering in Medicine and Biology Magazine*, vol. 14, no. 3, pp. 318–323, 1995.

[37] M. B. Cohn, L. S. Crawford, J. M. Wendlant, and S. S. Sastry, "Surgical applications of milli-robots," *Journal of robotic systems*, vol. 12, no. 6, pp. 401–416, 1995.

[38] S. Omata and Y. Terunuma, "New tactile sensor like the human hand and its applications," *Sensors and Actuators A: Physical*, vol. 35, no. 1, pp. 9–15, 1992.

[39] K. Takashimaa, K. Yoshinakab, T. Okazakia, and K. Ikeuchia, "An endoscopic tactile sensor for low invasive surgery," *Sensors and Actuators A: Physical*, vol. 119, no. 2, pp. 372–383, 2005.

[40] R. S. Fearing, "Tactile sensing mechanisms," *The International Journal of Robotics Research*, vol. 9, no. 3, pp. 3–23, 1990.

[41] M. T. Perri, D. A. Bottoni, A. L. Trejos, G. L. McCreery, M. D. Naish, R. V. Patel, and R. Malthaner, "A new tactile imaging device to aid with localizing lung tumours during thoracoscopic surgery," in *International Conference on Computer Assisted Radiology and Surgery (CARS)*, pp. 257–258, 2008.

[42] M. T. Perri, A. L. Trejos, M. D. Naish, R. V. Patel, and R. Malthaner, "Initial evaluation of a tactile/kinesthetic force feedback system for minimally invasive tumor localization," *IEEE/ASME Transaction on Mechatronics*, vol. 15, no. 6, pp. 925–931, 2010.

[43] S. D. Laycock and A. M. Day, "Recent developments and applications of haptic devices," *Computer Graphics Forum*, vol. 22, no. 2, pp. 117–132, 2003.

[44] V. Hayward, O. R. Astley, M. C. Hernandez, D. Grant, and G. Robles-De-La-Torre, "Haptic interfaces and devices," *Sensor Review*, vol. 24, no. 1, pp. 16–29, 2004.

[45] M. Bouzit, G. Popescu, and R. Boian, "The Rutgers master II-new design force-feedback glove," *IEEE/ASME Transaction on Mechatronics*, vol. 7, no. 2, pp. 256–263, 2002.

[46] J. Blake and H. B. Gurocak, "Haptic glove with MR brakes for virtual reality," *IEEE/ASME Transactions on Mechatronics*, vol. 14, no. 5, pp. 606–615, 2009.

[47] Y. S. Kim, L. C. Cho, M. Kim, and C. W. Lee, "A new exoskeleton-type masterarm with force reflection based on the torque sensor beam," in *IEEE International Conference on Robotics and Automation*, pp. 2628–2633, 2001.

[48] L. J. Stocco, S. E. Salcudean, and F. Sassani, "Optimal kinematic design of a haptic pen," *IEEE/ASME Transactions on Mechatronics*, vol. 6, no. 3, pp. 210–220, 2001.

[49] T. H. Massie and J. K. Salisbury, "The PHANToM haptic interface: a device for probing virtual objects," in *Proceeding of the ASME Winter Annual Meeting, Symposium on Haptic Interfaces for Virtual Environment and Teleoperator Systems*, pp. 295–299, 1994.

[50] D. Ryu, J. B. Song, C. Cho, S. Kang, and M. Kim, "Development of a six DOF haptic master for teleoperation of a mobile manipulator," *Mechatronics*, vol. 20, pp. 181–191, 2010.

[51] L. F. Lee, M. S. Narayanan, F. Mendel, V. N. Krovi, and P. Karam, "Kinematics analysis of in-parallel 5 DOF haptic device," in *IEEE/ASME International Conference on Advanced Intelligent Mechatronics*, pp. 237–241, 2010.

[52] G. Tholey and J. P. Desai, "A general-purpose 7 DOF haptic devive: Applications toward robot-assisted surgery," *IEEE/ASME Transactions on Mechatronics*, vol. 12, no. 6, pp. 662–669, 2007.

[53] M. Tavakoli, R. V. Patel, and M. Moallem, "A force reflective master-slave system for minimally invasive surgery," in *IEEE/RSJ Conference on Intelligent Robots and Systems*, pp. 3077–3082, 2003.

[54] T. H. Massie and J. K. Salisbury, "Force reflecting haptic interface," in *U.S. Patent : 5587937*, 1996.

[55] K. Kim, W. K. Chung, and Y. Youm, "Design and analysis of a new 7-DOF parallel type haptic device : PATHOS-II," in *IEEE/RSJ Conference on Intelligent Robots and Systems*, pp. 2241–2246, 2003.

[56] V. Hayward, P. Gregorio, O. Astley, S. Greenish, M. Doyon, L. Lessard, J. Mcdougall, I. Sinclair, S. Boelen, X. Chen, J. P. Demers, J. Poulin, I. Benguigui, N. Almey, B. Makuc, and X. Zhang, "Freedom-7: A high fidelity seven axis haptic device with application to surgical training," in *Lecture Notes in Control and Information Science 232*, pp. 445–456, 1998.

[57] http://www.forcedimension.com.

[58] M. Tavakoli, R. V. Patel, and M. Moallem, "Robotic suturing forces in the presence of haptic feedback and sensory substitution," in *IEEE Conference on Control Applications*, pp. 1–6, 2005.

[59] A. P. Miller, Z. Hammoud, J. S. Son, and W. J. Peine, "Tactile imaging system for localizing lung nodules during video assisted thoracoscopic surgery," in *IEEE International Conference on Robotics and Automation*, pp. 2996–3001, 2007.

[60] M. Hosseini, S. Najarian, S. Motaghinasab, and J. Dargahi, "Detection of tumours using a computational tactile sensing approach," *The International Journal of Medical Robotics and Computer Assisted Surgery*, vol. 2, no. 4, pp. 333–340, 2006.

[61] J. Dargahi, S. Najarian, and R. Ramezanifard, "Graphical display of tactile sensing data with application in minimally invasive surgery," *Canadian Journal of Electrical and Computer Engineering*, vol. 32, pp. 151–155, 2007.

[62] J. H. Killebrew, S. J. Bensmaia, J. F. Dammann, P. Denchev, S. S. Hsiao, J. C. Craig, and K. O. Johnson, "A dense array stimulator to generate arbitrary spatiotemporaltactile stimuli," *Journal of Neuroscience Methods*, vol. 161, no. 1, pp. 62–74, 2007.

[63] M. V. Ottermo, O. Stavdahl, and T. A. Johansen, "Electromechanical design of a miniature tactile shape display for minimally invasive surgery," in *First Joint Eurohaptics Conference and Symposium on Haptic Interfaces for Virtual Environment and Teleoperator Systems (World Haptics)*, pp. 561–562, 2005.

[64] M. Culjat, C. H. King, M. Franco, J. Bisley, W. Grundfest, and E. Dutson, "Pneumatic balloon actuators for tactile feedback in robotic surgery," *Industrial Robot*, vol. 35, no. 5, pp. 449–455, 2008.

[65] M. Kitagawa, D. Dokko, A. M. Okamura, B. T. Bethea, and D. D. Yuh, "Effect of sensory substitution on suture manipulation forces for surgical teleoperation," *Studies in health technology and informatics*, vol. 98, pp. 157–163, 2004.

[66] S. Peddamatham, W. Peine, and H. Z. Tan, "Assessment of vibrotactile feedback in a needle-insertion task using a surgical robot," in *Symposium on Haptic Interfaces for Virtual Environment and Teleoperator Systems*, pp. 93–99, 2008.

[67] G. S. Fischer, T. Akinbiyi, J. Z. S. Saha, M. Talaminiy, M. Marohny, and R. Taylor, "Ischemia and force sensing surgical instruments for augmenting available surgeon information," in *IEEE International Conference on Biomedical Robotics and Biomechatronics*, pp. 1030–1035, 2006.

[68] M. Tavakoli, R. V. Patel, and M. Moallem, "Haptic interaction in robot-assisted endoscopic surgery: a sensorized end-effector," *International Journal of Medical Robotics and Computer Assisted Surgery*, vol. 1, no. 2, pp. 53–63, 2005.

[69] M. Tavakoli, R. V. Patel, and M. Moallem, "A haptic interface for computer-integrated endoscopic surgery and training," *Virtual Reality*, vol. 9, no. 2-3, pp. 160–176, 2006.

[70] M. C. Cavusoglu, W. Williams, F. Tendick, and S. S. Sastry, "Robotics for telesurgery: second generation berkeley/ucsf laparoscopic te lesurgical workstation and looking towards the future applications," *Industrial Robot*, vol. 30, no. 1, pp. 22–29, 2003.

[71] H. Mayer, I. Nagy, A. Knoll, E. U. Schirmbeck, and R. Bauernschmitt, “The endo[PA]R system for minimally invasive robotic surgery,” in *IEEE/RSJ International Conference on Intelligent Robots and Systems*, pp. 3637–3642, 2004.

[72] N. Zemiti, G. Morel, T. Ortmaier, and N. Bonnet, “Mechatronics design of a new robot for force control in minimally invasive surgery,” *IEEE/ASME Transactions on Mechatronics*, vol. 12, no. 2, pp. 143–153, 2007.

[73] K. Tadano and K. Kawashima, “Development of a master slave system with force sensing using pneumatic servo system for laparoscopic surgery,” in *IEEE International Conference on Robotics and Automation*, pp. 947–952, 2007.

[74] M. J. H. Lum, D. C. W. Friedman, G. Sankaranarayanan, H. King, K. Fodero, R. Leuschke, B. Hannaford, J. Rosen, and M. N. Sinanan, “The raven: Design and validation of a telesurgery system,” *The International Journal of Robotics Research*, vol. 28, no. 9, pp. 1183–1197, 2009.

[75] http://www.dlr.de.

[76] A. Talasaz, R. V. Patel, and M. D. Naish, “Haptics-enabled teleoperation for robot-assisted tumor localization,” in *IEEE International Conference on Robotics and Automation*, pp. 5340 – 5345, 2010.

[77] M. Mahvash, J. Gwilliam, R. Agarwal, B. Vagvolgi, L. M. Su, D. D. Yuh, and A. M. Okamura, “Force-feedback surgical teleoperator: Controller design and palpation experiments,” in *16th Symposium on Haptic Interfaces for Virtual Environments and Teleoperator Systems*, pp. 465–471, 2008.

[78] A. L. Trejos, J. Jayender, M. T. Perri, M. D. Naish, R. V. Patel, and R. Malthaner, “Robot-assisted tactile sensing for minimally invasive tumor localization,” *The International Journal of Robotics Research*, vol. 28, no. 9, pp. 1118–1133, 2009.

[79] R. L. Feller, C. K. L. Lau, C. R. Wagner, D. P. Perrin, and R. D. Howe, “The effect of force feedback on remote palpation,” in *IEEE International Conference on Robotics and Automation*, pp. 782–788, 2004.

[80] M. T. Perri, A. L. Trejos, M. D. Naish, R. V. Patel, and R. Malthaner, “New tactile sensing system for minimally invasive surgical tumour localization,” *The International Journal of Medical Robotics and Computer Assisted Surgery*, vol. 6, pp. 211–220, 2010.

[81] C. R. Wagner, D. P. Perrin, R. L. Feller, R. D. Howe, O. Clatz, H. Delingette, and N. Ayache, “Integrating tactile and force feedback with finite element models,” in *IEEE International Conference on Robotics and Automation*, pp. 1–6, 2005.

[82] A. H. Zahraee, J. Szewczyk, and G. Morel, "Evaluating control modes for hand-held robotic surgical instrument using virtual reality simulator," in *IEEE/ASME International Conference on Advanced Intelligent Mechatronics*, pp. 1946–1951, 2009.

[83] B. T. Bethea, A. M. Okamura, M. Kitagawa, T. P. Fitton, S. M. Cattaneo, V. L. Gott, W. A. Baumgartner, and D. D. Yuh, "Application of haptic feedback to robotic surgery," *Journal of Laparoendoscopic and Advanced Surgical Techniques*, vol. 14, no. 3, pp. 191–195, 2004.

[84] http://www.quanser.com.

[85] H. Bassan, A. Talasaz, and R. V. Patel, "Design and characterization of a 7-dof haptic interface for minimally invasive surgery test-bed," in *IEEE/RSJ Conference on Intelligent Robots and Systems*, pp. 4098–4103, 2009.

[86] http://www.ccontrols.com.

[87] http://www.pressureprofile.com.

[88] http://www.ati-ia.com.

[89] C. W. Kennedy and J. P. Desai, "Modeling and control of the Mitsubishi PA-10 robot arm harmonic drive system," *IEEE/ASME Transaction on Mechatronics*, vol. 10, no. 3, pp. 263–274, 2005.

[90] N. A. Bompos, P. K. Artemiadis, A. S. Oikonomopoulos, and K. J. Kyriakopoulos, "Modeling, full identification and control of the Mitsubishi PA-10 robot arm," in *IEEE/ASME International Conference on Advanced Intelligent Mechatronics*, pp. 1–6, 2007.

[91] http://www.northerndigital.com.

[92] M. Carricato and C. M. Gosselin, "On the modeling of leg constraint in the dynamic analysis of Gouph/Stewart-type platforms," *Journal of Computational and Nonlinear Dynamics*, vol. 4, no. 1, paper 011008, 2009.

[93] http://www.maplesoft.com.

[94] http://www.clarontech.com.

[95] H. Khalil, "Adaptive output feedback control of nonlinear systems represented by input-output models," *IEEE Transactions on Automatic Control*, vol. 41, pp. 177–188, 1996.

[96] D. A. Lawrence, "Stability and transparency in bilateral teleoperation," *IEEE Transactions on Robotics and Automation*, vol. 9, no. 5, pp. 624–637, 1993.

[97] K. Hashtrudi-Zaad and S. E. Salcudean, “Analysis and evaluation of stability and performance robustnes for teleoperation control architectures,” in *IEEE International Conference on Robotics and Automation*, pp. 3107–3113, 2000.

[98] A. Stotsky and I. Kolmanovsky, “Application of input estimation techniques to charge estimation and control in automotive engines,” *Control Engineering Practice*, vol. 10, pp. 1371–1383, 2002.

[99] R. Locke and R. V. Patel, “Optimal remote center of motion location for robotics assisted minimally invasive surgery,” in *IEEE International Conference on Robotics and Automation*, pp. 1900–1905, 2007.

[100] H. Seraji, “Configuration control of redundant manipulators: Theory and implementation,” *IEEE Transactions on Robotics and Automation*, vol. 5, no. 4, pp. 472–490, 1989.

[101] B. Xian, M. S. de Queiroz, D. Dawson, and I. Walker, “Task-space tracking control of robot manipulators via quaternion feedback,” *IEEE Transactions on Robotics and Automation*, vol. 20, no. 1, pp. 160–167, 2004.

[102] J. Y. S. Luh, M. W. Walker, and R. P. Paul, “Resolved-acceleration control of mechanical manipulators,” *IEEE Transactions on Automatic Control*, vol. AC-25, no. 3, pp. 468–474, 1980.

[103] Y. Nakamura and H. Hanafusa, “Inverse kinematic solutions with singularity robustness for robot manipulator control,” *ASME Journal of Dynamic Systems, Measurement and Control*, vol. 108, no. 3, pp. 163–171, 1986.

[104] R. Patel and F. Shadpey, *Control of redundant robot manipulators: theory and experiments.* Lecture Notes in Control and Information Science, Springer, 2005.

CURRICULUM VITAE
ALI TALASAZ

EDUCATION

2007-2012 — **The University of Western Ontario**
Degree: **Ph.D. in Electrical Engineering** — **London, Canada**

2001-2003 — **Sharif University of Technology**
Degree: **M.Sc. in Electrical Engineering** — **Tehran, Iran**

1997-2001 — **Chamran University**
Degree: **B.Sc. in Electrical Engineering** — **Ahvaz, Iran**

THESES

- Ph.D. Thesis
  Haptics-Enabled Teleoperation for Robotics-Assisted Minimally Invasive Surgery
  Advisor: Dr. R. V. Patel
- M.Sc. Thesis
  Adaptive Fuzzy Sliding Mode Control of a Flexible Transmission System
  Advisor: Dr. N. Sadati
- B.Sc. Thesis
  Design and Implementation of Over-Flux Protection Relay using 89C51 Microcontroller
  Advisor: Dr. S. Namazi

TEACHING EXPERIENCE

2007-2011 — **The University of Western Ontario**
Position: **Teaching Assistant** — **London, Canada**

2006-2007 — **Azad University of Ahvaz/Dezful**
Position: **Instructor** — **Khouzestan, Iran**

2002-2003 — **Sharif University of Technology**
Position: **Teaching Assistant** — **Tehran, Iran**

WORK EXPERIENCE

2007-2012 — **Canadian Surgical Technologies and Advanced Robotics**
Position: **Research Associate** — **London, Canada**

2005-2007 — **Khouzestan Gas Distribution Company**
Position: **Project Manager** — **Ahvaz, Iran**

2001-2003 — **Iran Seabock Company**
Position: **System Design Engineer** — **Tehran, Iran**

HONORS AND AWARDS

- Western Graduate Research Scholarship (WGRS) [2007-2011].
- Ranked 12th among 10000 participants in the national iranian university entrance exam for M.Sc. [2001].
- Graduated with distinction from Chamran University Faculty of Engineering [2001].
- 1% in the national iranian university entrance exam for B.Sc. [1997].

JOURNAL PAPERS

- **A. Talasaz**, and R. V. Patel, "Integration of force reflection with tactile sensing for minimally invasive robot-assisted tumor localization" *Submitted to IEEE Transactions on Haptics*, Second revision, Manuscript ID: TH-2011-08-0062.
- **A. Talasaz**, S. Perreault, H. Bassan, A.L. Trejos and R. V. Patel, "A 7-DOF haptics-enabled master-slave teleoperated test-bed for minimally invasive surgery: Design and application", *Under Submission to the International Journal of Robotics Research.*
- N. Sadati, and **A. Talasaz**, "Variable structure control with adaptive fuzzy sliding surface," *Journal of Vibration and Control*, Volume 12, Issue 11, pp. 1251-1270, Nov. 2006.

REFEREED CONFERENCE PAPERS

- M. Currie, MD, **A. Talasaz**, Phd, A.L. Trejos, MASc, R. Rayman, MD, M.W.A. Chu, MD, R. V. Patel, Phd, T. Peters, Phd, and B. Kiaii, MD, "The role of haptics in robotics-assisted mitral valve annuloplasty," *Submitted to the Hamlyn Symposium on Medical Robotics, 2012.*
- **A. Talasaz**, A.L. Trejos, and R.V. Patel "Effect of Force Feedback on Performance of Robotics-Assisted Suturing," *Accepted for publication at the IEEE International Conference on Biomedical Robotics and Biomechatronics (BioRob 2012).*
- **A. Talasaz**, and R.V. Patel "Remote palpation to localize tumors in robot-assisted minimally invasive approach," *Accepted for publication at the IEEE International Conference on Robotics and Automation 2012.*
- S. Perreault, **A. Talasaz**, A.L. Trejos, C. D. Ward, R. V. Patel, and B. Kiaii, "A 7-DOF haptics-enabled teleoperated robotic system: kinematic modeling and experimental verification," *International Conference on Biomedical Robotics and Biomechatronics*, Tokyo, Japan, Sep. 2010
- **A. Talasaz**, R.V. Patel, and M.D. Naish, "Haptics-enabled teleoperation for robot-assisted tumor localization," *IEEE International Conference on Robotics and Automation*, Alaska, May 2010.

- H. Bassan, **A. Talasaz**, and R.V. Patel, "Design and characterization of a 7-DOF haptic interface for minimally invasive surgery test-bed," *IEEE/RSJ International Conference on Intelligent Robots and Systems*, MO, USA, Oct. 2009.
- **A. Talasaz**, and A.N. Shooshtari, "Closed-loop pressure control based on smith predictor for gas distribution network," *IEEE Conference; Information, Decision and Control, The Challenge of Distributed Systems*, Adelaide, Australia, Feb. 2007.
- **A. Talasaz**, and A.N. Shooshtari, "Adaptive predictive control application in gas distribution network: a case study," *IEEE Conference; Information, Decision and Control, The Challenge of Distributed Systems*, Adelaide, Australia, Feb. 2007.
- N. Sadati, and **A. Talasaz**, "A robust fuzzy sliding mode control for uncertain dynamic systems," *IEEE Conference on Systems, Man and Cybernetics*, Netherlands, Oct. 2004.
- N. Sadati, and **A. Talasaz**, "Sliding mode control for a flexible transmission system," *IEEE Conference on Systems, Man and Cybernetics*, Netherlands, Oct. 2004.
- N. Sadati, and **A. Talasaz**, "Chattering-free adaptive fuzzy sliding mode control," *IEEE Conference on Cybernetics and Intelligent Systems*, Singapore, Dec. 2004.
- N. Sadati, and **A. Talasaz**, "Robust fuzzy multimodel control using variable structure system," *IEEE Conference on Cybernetics and Intelligent Systems*, Singapore, Dec. 2004.